MAGNETIC DYNAMICS IN MAGNETIC MULTILAYERS AND SPINTRONIC DEVICES

by

Hang Chen

A dissertation submitted to the Faculty of the University of Delaware in partial fulfillment of the requirements for the degree of Doctor of Philosophy in Physics

Spring 2021

© 2021 Hang Chen
All Rights Reserved

MAGNETIC DYNAMICS IN MAGNETIC MULTILAYERS AND SPINTRONIC DEVICES

by

Hang Chen

Approved: _____
Edmund R. Nowak, Ph.D.
Chair of the Department of Physics and Astronomy

Approved: _____
John A. Pelesko, Ph.D.
Dean of the College of Arts and Sciences

Approved: _____
Louis F. Rossi, Ph.D.
Dean of the Graduate College and Vice Provost for Graduate and Professional Education

I certify that I have read this dissertation and that in my opinion it meets the academic and professional standard required by the University as a dissertation for the degree of Doctor of Philosophy.

Signed: _____

John Q. Xiao, Ph.D.
Professor in charge of dissertation

I certify that I have read this dissertation and that in my opinion it meets the academic and professional standard required by the University as a dissertation for the degree of Doctor of Philosophy.

Signed: _____

Yi Ji, Ph.D.
Member of dissertation committee

I certify that I have read this dissertation and that in my opinion it meets the academic and professional standard required by the University as a dissertation for the degree of Doctor of Philosophy.

Signed: _____

Bennett A. Maruca, Ph.D.
Member of dissertation committee

I certify that I have read this dissertation and that in my opinion it meets the academic and professional standard required by the University as a dissertation for the degree of Doctor of Philosophy.

Signed: _____

Anderson Janotti, Ph.D.
Member of dissertation committee

ACKNOWLEDGMENTS

Undertaking this PhD has been a challenging and rewarding experience for me and it would not be possible to do without the support that I received from many people.

First and foremost, I wish to express my deepest gratitude to my advisor Prof. John Q. Xiao for his invaluable supervision, dedicated support, and guidance in my academic research. His wide range of knowledge and outstanding insight on research inspired me to explore the unknown in my research field.

I would like to offer my special thanks to Dr. Yu-Sheng Ou, Dr. Tao Wang and Dr. Yunpeng Chen for their patient help and selfless effort in guiding me through the experiments at the beginning of my research. I am grateful to our collaborator Prof. Christian Binek at University of Nebraska–Lincoln for his assistance. I would like to acknowledge Prof. Matthew Doty, Prof. Yuping Zeng and Prof. Yi Ji for their help on sample fabrication and experimental measurement.

Additionally, I would like to thank my lab mates: Dr. Jun Wu, Dr. Xinran Zhou, Dr. Yunsong Xie, Dr. Chuan Qin, Dr. Muhammad Asif Warsi, Dr. Harsha Kannan, Dr. Yunjiao Cai, Xingyu Shen, Yang Wang and Xinhao Wang for their kind help in those years.

Finally, I wish to deeply thank my parents, my sister, my wife and my son for their unwavering support and belief in me.

TABLE OF CONTENTS

LIST OF TABLES

LIST OF FIGURES

ABSTRACT

A critical issue in spintronic devices is how to efficiently switch the magnetization of a nanomagnet. The switching is typically occurred at ferromagnetic resonant frequency. One of the very desired features is to enhance the resonant frequency so as to increase the switching speed. In this thesis. We use optical mode in coupled FM bilayers to significantly enhance the resonance frequency because the ferromagnetic exchange coupling is much stronger compared with other effective field introduced by, for example, strain or anisotropy. We theoretically and experimentally study the resonant frequency in $Co_{90}Fe_{10}/Ta/(Ni_{80}Fe_{20})_{1-x}Cu_x$ trilayer. we also validate the theoretical model with experimental results and use the theoretical model to further design heterostructures with desired properties such as enhanced intensity in OM. All of our experimental results are fully explained by our model which also allows us to identify the coupling mechanism as Néel "orange-peel" coupling and extract the interlayer coupling strength. In current magnetic random access memories (MRAMs), the magnetization is switched via spin transfer torques (STT) or spin orbit torques (SOTs). In this thesis, we use a time-resolved (TR) Magneto-optic Kerr effect (TRMOKE) to investigate the SOT-induced magnetization dynamics in Py/Pt and Ta/CoFeB heterostructures. We have answered three questions as we set to explore: (1) the field-like torque determines initial oscillation magnitude and the damping-like torque determines the final steady position; (2) both the effect field of damping-like toque h_{DL} and field-like torque h_{FL} can be extracted from the TRMOKE spectrum, and

(3) the ratio h_{DL}/ h_{FL} measured from dynamics are the same as those measured at low frequency. Finally, we also explore the way of using voltage to switch the magnetization in order to significantly reduce the energy consumption. We employed an antiferromagnetic Cr_2O_3 film with net a net magnetization at the film surface. The surface magnetization can be isothermally switched via applied electric field (voltage), enabling "writing" function in the memory cell. We solved various challenges in developing the final device including (1) exchange coupling between the surface magnetization and the magnetization in a ferromagnetic heterostructure of Co/Pd multilayer, (2) the exchange coupling between Co/Pd and CoFeB which has perpendicular magnetization and serves as a bottom electrode of magnetic tunnel junction for readout. (3) the leakage issue of Cr_2O_3, (4) the contact to middle layer that is less than 5 nm thick, and (5) device layout and detailed fabrication steps. Although we did not have time to fully demonstrate the devices, all key steps have been well resolved.

Chapter 1

INTRODUCTION

1.1 Spintronics and Related Topics

Spintronics is an important branches of condensed matter physics that studies the physical properties of the electron spin and explores the way to manipulate the electron spin, in additional to its charge, for the next-generation nano electronic device with low energy consumption and high efficiency [1,2]. There is a wide range of subjects under this novel field from the investigation of controlling single localized spin as spin qubits for quantum computation to the study of collective spin transport and spin dynamics. Since the discovery of the giant magnetoresistance (GMR) [3,4]and tunneling magnetoresistance (TMR) [5], the field has evolved rapidly, attracted much attention, and made significant impact on information technology.

One of key ingredients in spintronics is to control the magnetization switching, which requires the understanding of the magnetization dynamics. Fundamentally, a single dynamic magnetization is a precession movement that can be mathematically descripted by a simple partial differential equation. The precession of the magnetization is driven by a torque generated from the applied radio frequency (rf) magnetic field. At the ferromagnetic resonance (FMR) at which the natural precession frequency of the dynamic magnetization in a ferromagnet equals to the frequency of the applied rf field, the dynamic magnetization has the largest precession angle and absorbs maximum energy from driven rf field. The magnetization is switched via precession around FMR. FMR spectroscopy has also been developed as a powerful

experimental technique to characterize the gyromagnetic ratio, anisotropy field, and damping constant of magnetic materials. In this thesis, the FMR measurement is employed to study the exchange coupling in the synthetic ferromagnetic coupled trilayers.

An enabling technology for broad applications of spintronic devices is to develop electrical mean, not to generate magnetic field, to switch magnetization. One of heavily investigated technology is based on the current induced spin transfer torque (STT) and spin orbit torques (SOTs), which has been proved as an efficient for magnetization switching[2,6]. The research on SOTs is the main topic in this thesis. Detecting and characterizing the torques in a variety of magnetic structures becomes significant to understanding the origins of the current induced torques which can guide the search for materials and heterostructures with high efficiency. Either electrical or optical measurements have been reported to measure the SOTs in magnetic heterostructures [7-10]. One of the optical techniques, Magnetic-optical Kerr effect (MOKE) [10], was developed in our group and is mainly employed in our experiments to measure the SOTs since it is free of artifacts, such as thermal effect or other nonlinear processes, that may exist in electronic measurements based on second harmonic Hall measurements.

In this Chapter, we first introduce the concept of FMR and its application in magnetic films. Followed by the discussions of the charge-to-spin conversion concept, and various contributions to SOTs. Finally, the principles of two important optical effects, Faraday effect and MOKE are also introduced in terms of its discoveries, mechanisms, and phenomenology definitions.

1.2 Ferromagnetic Resonance in Magnetic Films

The resonance occurs when the Zeeman energy levels of a quantized system is split by a uniform magnetic field and the system absorbs energy from the radio frequency (*rf*) magnetic field at specific frequencies that match the energy transitions between the energy levels. Many types of resonance phenomena have been discovered and developed to investigate the magnetic properties of the materials such as nuclear magnetic resonance (NMR) [11], electron paramagnetic/spin resonance (EPR, ESR) [12], spin wave resonance (SWR) [13], ferromagnetic resonance (FMR) [14], antiferromagnetic resonance (AFMR) and so on. Particularly, the FMR, experimentally discovered in 1911 by V. K. Arkad'yev, has been widely applied to probe the magnetization **M** and magnetic anisotropy K_a of ferromagnetic materials. It is also a useful tool to investigate the spin waves [15] and spin dynamics in ferromagnetic, ferrimagnetic or antiferromagnetic films.

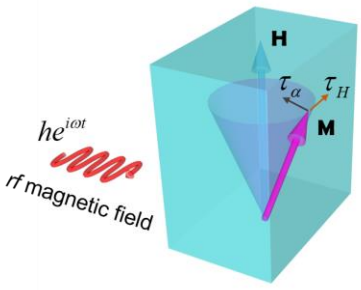

Figure 1.1 The schematic of a single precessing magnetization (pink arrow) driven by *rf* magnetic field in a uniform magnetic bulk material. The symbol H is the external field, which induces the torque τ_H on the magnetization M of the material. τ_α is the effective torque induced by the damping constant of the magnetic material.

Magnetization dynamics is illustrated in Figure 1.1 where the magnetization is rotating around the external magnetic field **H** which exerts a torque (**M**×**H**) on the magnetization and this torque forces the **M** to precess around the axis of the **H**. The movement of **M** can be described by a time-dependent dynamic equation

$$\frac{d\mathbf{M}}{dt} = -\gamma \mathbf{M} \times \mathbf{H}, \tag{1.1}$$

where γ is the gyromagnetic ratio and t is the time. In an ideal infinitely large magnetic material with uniform magnetic isotropy, the precession frequency is called Larmor frequency and given by $f_0=(\gamma/2\pi)H$. It is noted that besides the external field, f_0 might relate to the magnetization and geometry of the magnet at nonideal case. The typical value of gyromagnetic ratio $\gamma_e/2\pi$ for electron is about 28GHz/T, which suggests f_0 stays in GHz range (microwave) for sample in the field of several tenths of Tesla.

The existence of damping in a ferromagnet would drag the precessing magnetization towards the external field direction. Thus a damping torque term is phenomenologically introduced to the right hand side of the Eq (1.1) in the form of either Landau-Lifshitz [16] or Gilbert damping term. It is noted that the two forms are equivalent when the damping is small. In this thesis, we employ the Landau-Lifshitz-Gilbert (LLG) [17] equation which is given by

$$\frac{d\mathbf{M}}{dt} = -\gamma \mathbf{M} \times \mathbf{H}_{eff} + \frac{\alpha}{M_s}\left(\mathbf{M} \times \frac{d\mathbf{M}}{dt}\right), \tag{1.2}$$

where α is the effective damping factor, and M_s is the saturation magnetization, $\mathbf{H}_{eff}$ is the total effective field including the external magnetic field, *rf* magnetic field and any other effective fields arising from anisotropy, shape, and strain. Typically, the dynamic equation can be solved by writing down the magnetization and effective field vectors in a cartesian coordinates [18,19]. Suppose the external field H is applied in z direction and *rf* magnetic fields can be written as $\mathbf{h}(t) = h_0 e^{i\omega t} = [h_x, h_y, h_z]\, e^{i\omega t}$, which

will lead to a dynamic magnetization precession at frequency ω, i.e., $\mathbf{m}(t)=m_0 e^{i\omega t}$, here $\mathbf{m}(t)$ represents the unit vector of the magnetization. The total magnetization and effective field can be written as

$$\mathbf{M}(t) = [m_x, m_y, M_0+m_z], \tag{1.3}$$

$$\mathbf{H}_{eff}(t)= [h_x, h_y, H+h_z], \tag{1.4}$$

where h_j and m_j ($j = x, y, z$) are the magnitude of the dynamic magnetization and *rf* field in j direction, $M_0 \approx M_s$ is the static component of magnetization in z axis. By substituting Eqs (1.3) and (1.4) into Eq (1.2) and neglecting the high order terms (since $h << H$, $m << M_s$), one can obtain

$$\begin{cases} i\omega m_x+(\omega_0+i\alpha\omega)m_y=\omega_m h_y \\ -(\omega_0+i\alpha\omega)m_x+i\omega m_y=-\omega_m h_x, \\ m_z=0 \end{cases} \tag{1.5}$$

where $\omega_0 = \gamma H$, $\omega_m = \gamma M_s$. From Eq (1.5), the components of m_x and m_y can be solved in terms of h_x and h_y. According to the relation $\mathbf{m} = \boldsymbol{\chi}\mathbf{h}$ [20], the susceptibility tensor $\boldsymbol{\chi}$ is given in the form of

$$\boldsymbol{\chi} = \begin{bmatrix} \chi_{xx} & -i\chi_{xy} & 0 \\ i\chi_{yx} & \chi_{yy} & 0 \\ 0 & 0 & 0 \end{bmatrix}, \tag{1.6}$$

where $\chi_{xx} = \chi_{yy}$ and $\chi_{xy} = \chi_{yx}$. It is noted that χ_{ij} represents the induced magnetization in i axis by the *rf* magnetic field in j axis. From Eq (1.5), we find the expression of χ_{xx} and χ_{xy}

$$\begin{cases} \chi_{xx} = \dfrac{\omega_m(\omega_0 + i\alpha\omega)}{(\omega_0 + i\alpha\omega)^2 - \omega^2} \\ \chi_{xy} = \dfrac{-\omega_m\omega}{(\omega_0 + i\alpha\omega)^2 - \omega^2} \end{cases}. \tag{1.7}$$

It is obvious that both χ_{xx} and χ_{xy} are complex number. With the assumption that $\alpha<<1$, Eq (1.7) can be decomposed into real and imaginary parts

$$\begin{cases} \chi'_{xx} = 1 + \dfrac{\omega_m \omega_0 (\omega_0^2 - \omega^2)}{(\omega_0^2 - \omega^2)^2 + 4\omega_0^2 \alpha^2 \omega^2} \\ \chi''_{xx} = \dfrac{\omega_m \alpha \omega (\omega_0^2 + \omega^2)}{(\omega_0^2 - \omega^2)^2 + 4\omega_0^2 \alpha^2 \omega^2} \\ \chi'_{xy} = \dfrac{\omega_m \omega (\omega_0^2 - \omega^2)}{(\omega_0^2 - \omega^2)^2 + 4\omega_0^2 \alpha^2 \omega^2} \\ \chi''_{xy} = \dfrac{-2\omega_m \omega_0 \alpha \omega^2}{(\omega_0^2 - \omega^2)^2 + 4\omega_0^2 \alpha^2 \omega^2} \end{cases} . \quad (1.8)$$

It is known that the real part of the susceptibility reflects the magnetization as the function of the external field H in different direction, while the imaginary part describes the phase shift and the energy loss in the material. It can be seen from Eq (1.8) that the real parts of χ_{xx} (or χ_{xy}) are zero while the imaginary part reaches the maximum when the external field is tuned to H_0 which makes $\omega_0 = \omega$. That means the system has the largest energy absorption from the driven source, i.e., the system is at FMR and the H_0 is call resonant field at frequency ω.

All formula derivation shown above are conducted with the assumption that the system is magnetically isotropic and uniform. In reality, some magnetic anisotropies need to be taken into account like the magneto-crystalline anisotropy, shape anisotropy and surface anisotropy [19]. As a result, the expression of the resonant frequency ω_0 varies with the different configuration of effective anisotropic fields. For example, in a film with perpendicular magnetic anisotropy, the resonant frequency is given by the Kittel formula[21]

$$\omega_0 = \mu_0 \gamma (H - M_s), \quad (1.9)$$

where the $-M_s$ term is originated from the demagnetizing field $H_d = -NM$ in perpendicular direction with the demagnetization factor N=1 in z direction [22]. On the other hand, in an in-plane magnetized film, both in plane effective anisotropic field H_a and demagnetizing field proportional to the out-of-plane component of dynamic m(t), should be added to the total effective field. Therefore, the ferromagnetic resonance can be expressed by

$$\omega_0 = \mu_0\gamma\sqrt{(H + H_a)(H + H_a + M_s)}\,. \tag{1.10}$$

The Eq (1.10) actually gives the dispersion relationship for an in-plane magnetized ferromagnetic film. At a fixed frequency one can always find a corresponding resonant field H=H_0 and vice versa. This relation is widely applied in the FMR measurement technique to extract the saturation magnetization and anisotropy parameters of the magnetic material under test. More details will be discussed in Chapter 3.

1.3 Charge-to-Spin Conversion

In magnetic conductors, the spin polarized currents can be generated from the exchange interaction between conduction electrons and local spins. Alternatively, as it has progressively been understood in the last decade, spin-polarized currents can also be generated (or detected) in nonmagnetic materials by the spin-orbit interactions, mainly through the bulk spin Hall effect (SHE) or interfacial Rashba effects. For example, the SHE can be used to convert the charge current in a nonmagnetic conductor (NM) into spin current transverse to the charge current. Such a spin current can enter and exert a torque on the magnetization of a neighboring ferromagnetic layer (FM). Therefore, understanding the charge-to-spin conversion at a NM/FM interface is essential in the study of current induced SOTs.

1.3.1 Spin Current and Spin Injection Cross a NM/FM Interface

An electron carries not only a negative electric charge but also an internal angular momentum named spin. The *z* component (projection on spin axis) of spin angular momentum has only two values: $\pm \hbar/2$, where $\hbar$ is the Planck constant, positive and negative sign corresponds to spin up and down, respectively. Spin is the primary origin of the ferromagnetism. The material shows magnetization when the spins of the electrons are parallelly aligned. A flow of electron charges is a charge current which has been well understood in physics and applied in the conventional electron devices. Since the electron also carries the spin, the existence of charge current implies the coexistent flow of spin. This flow is called spin current [23]. In the aspect of its application, the spin-based devices own much higher efficiency than that of conventional charge-based devices due to the exchange coupling among spins which often induces coherent motions.

There are two important features that distinguish a spin current from charge current [23]: 1) spin current is invariant under the time reversal; 2) spin current is the flow of angular momentum. Those properties enable the spin current as a carrier to transfer or manipulate the quantum information. Spin current may exist even the charge current is zero. For example, two electrons with opposite spins moving in opposite directions will lead to zero net charge current but giving rise a spin current carrying angular moment of $\hbar$. The spin current in absent of charge current is called pure spin current.

An interesting consequence of the spin current is the spin accumulation near the boundary of the material. For example, a charge current in FM/NM bilayer is spin-polarized and it will lead to spin accumulation at the interface and spin injection into

NM layer due to the spin diffusion [24]. The spin current consists of regular drift current and diffusion current so that the spin current density j [25] is written as

$$j = \sigma E + eD\nabla n, \tag{1.11}$$

where E is the electric field driving the charge current, σ is the electrical conductivity, D is the diffusion constant and n is the electron density. From the Fermi-Dirac distribution, it derives that chemical potential equals Fermi energy at zero temperature, i.e. $\mu^c(T=0) = E_F$ and $\delta\mu^c = \delta n/N(E_F)$. Therefore, the gradient of electrochemical potential is

$$\nabla\mu = \nabla(-e\phi + \mu^c) = eE + \frac{\nabla n}{N(E_F)}, \tag{1.12}$$

where ϕ is electric potential and N is the density of states [26]. According to the Einstein relation $\sigma = e^2N(E_F)D$ [27], Eqs (1.11) and (1.12), one obtains

$$j = \frac{\sigma}{e}\nabla\mu. \tag{1.13}$$

It is noted that the electrochemical potential is spin-dependent and their difference in two spin channels gives rise to the spin current. The charge current and spin current are given by

$$j_c = \frac{1}{e}\nabla(\sigma_\uparrow\mu_\uparrow + \sigma_\downarrow\mu_\downarrow). \tag{1.14}$$

$$j_s = \frac{1}{e}\nabla(\sigma_\uparrow\mu_\uparrow - \sigma_\downarrow\mu_\downarrow), \tag{1.15}$$

where the symbols ↑ and ↓ stands for spin-up and spin-down channels, respectively. In a nonmagnetic metal or semiconductor, the electrical conductivity is spin-independent, $\sigma_\uparrow = \sigma_\downarrow$. By substituting Eqs (1.14) and (1.15) into the corresponding continuity equations, one obtains

$$\nabla^2(\sigma_\uparrow\mu_\uparrow + \sigma_\downarrow\mu_\downarrow) = 0, \tag{1.16}$$

$$\nabla^2(\mu_\uparrow - \mu_\downarrow) = \frac{1}{\lambda^2}(\mu_\uparrow - \mu_\downarrow), \tag{1.17}$$

where λ is the spin-diffusion length, $\lambda = \sqrt{D_{ave}\tau_{sf}}$, D_{ave} is spin-averaged diffusion constant and τ_{sf} is the spin relaxation time. The general solution of Eqs (1.16) and (1.17) are $\mu_{\uparrow}^{F}$, $\mu_{\downarrow}^{F}$, $\mu_{\uparrow}^{N}$, $\mu_{\downarrow}^{N}$ which represent the electrochemical potential of ↑ and ↓ in FM and NM layer, respectively. Their expressions can be determined by applying the boundary conditions at the interface. The distribution of the electrochemical potentials along the thickness direction is shown in Figure 1.2 where at the interface $x = 0$ both the electrochemical potentials and spin currents are continuous in each spin channel.

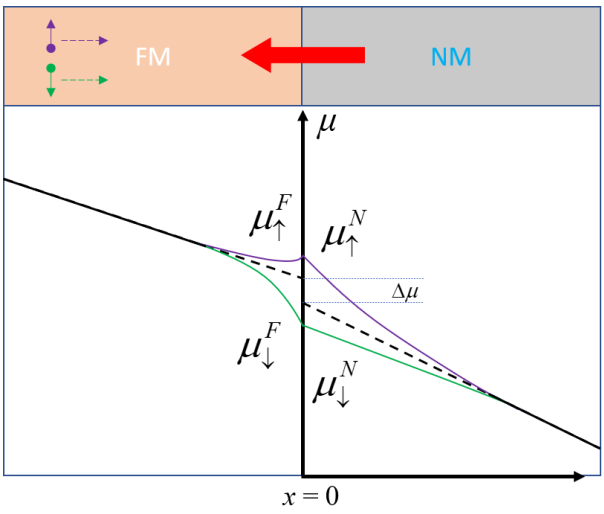

Figure 1.2 A ferromagnetic/nonmagnetic (FM/NM) structure with charge current represented by large red arrow passing through the interface. The bottom box shows the spin-dependent electrochemical potential distribution along the current direction.

In FM layer, $\sigma_{\uparrow}^{F} \neq \sigma_{\downarrow}^{F}$, $\sigma_{\uparrow}^{F} + \sigma_{\downarrow}^{F} = \sigma_{F}$, while in NM layer, $\sigma_{\uparrow}^{N} \neq \sigma_{\downarrow}^{N}$, $\sigma_{\uparrow}^{N} + \sigma_{\downarrow}^{N} = \sigma_{N}$. Applying the boundary condition at the interface, it gives

$$\mu_{\uparrow\downarrow}^{F} = \frac{ej_c}{\sigma^{F}} x \mp G \frac{(1-P^2)\sigma^{F}}{2\sigma_{\uparrow\downarrow}^{F}} e^{x/\lambda_F}, \qquad (1.18)$$

$$\mu_{\uparrow\downarrow}^{N} = \frac{ej_c}{\sigma^N} x + G(P \mp 1)e^{-x/\lambda_F} , \tag{1.19}$$

where P is polarization in FM layer, and G is expressed as

$$P = \frac{\sigma_{\uparrow}^{F} - \sigma_{\downarrow}^{F}}{\sigma_{\uparrow}^{F} + \sigma_{\downarrow}^{F}} , \tag{1.20}$$

$$G = \frac{ej_c P\lambda_N}{\sigma^N[1+(1-P^2)\frac{\sigma_F\lambda_N}{\sigma_N\lambda_F}]} . \tag{1.21}$$

In Figure 1.2 it shows the spatial variation of $\mu_{\uparrow}$, $\mu_{\downarrow}$ when a charge current passing through the FM/NM bilayer. At the interface, the spin-polarized current is formed and injected into the NM layer. The polarization P' in NM layer is given by

$$P' = \frac{P}{1+(1-P^2)\frac{\sigma_F\lambda_N}{\sigma_N\lambda_F}} . \tag{1.22}$$

The spin-polarized current diffusing across the interface towards the NM layer is driven by gradient $\nabla(\mu_{\uparrow}^{N} - \mu_{\downarrow}^{N})$ and exponentially decaying along the gradient direction. The decay length is characterized by the spin diffusion length λ_N. The spin-polarized current in the FM layer is suppressed near the interface because of the back flow of the spin current induced by spin accumulation at the interface [28]. The Eq (1.22) indicates that the term $\sigma_F\lambda_N/\sigma_N\lambda_F$ should be as smaller as possible to get a larger interfacial polarization P' if one use FM as a spin current source. Typically, $\lambda_N >> \lambda_F$, which makes it difficult to obtain a large spin polarization if NM is a semiconductor since the conductivity mismatch problem, $\sigma_F >> \sigma_N$. To circumvent this obstacle and get high spin injection efficiency, one of the solutions is to replace the FM with a ferromagnetic semiconductor to get a better conductivity match. An alternative solution is to manipulate the FM/NM interface through a insertion in between [26].

1.3.2 Spin Hall Effect and Inverse Spin Hall Effect

So far, we have discussed the spin current generated in a FM/NM bilayer by passing a charge current perpendicularly through the layers. Here, the FM layer works as a spin source where the spin polarization direction is determined by the magnetization direction in FM layer. Conversely, spin current can also be generated by a flow of an in-plane charge current in a NM layer with spin-orbit coupling, which is named spin Hall effect (SHE) [29]. In addition, spin current can also be produced via a dynamic method of spin pumping [30,31], in which the precessing magnetization in a FM material continuously inject spin current into a neighboring NM layer. The injected spin current in NM layer can be detected via inverse spin Hall effect (ISHE) or non-local spin valve measurement [32].

The spin Hall effect phenomena was first predicted by Mikhail I. Dyakonov and Vladimir I. Perel [33] in 1971. This effect was rediscovered and named as "spin Hall effect" by J. E. Hirsch[29] in 1999. The spin Hall effect is an effect analogous to the normal Hall effect where the flowing charges with opposite sign accumulate at the opposite boundaries of the object due to the Lorenz force exerted on the charges by external magnetic field. Instead of charges accumulation, spin Hall effect generates the accumulation of the spins with up and down direction at the opposite boundaries without the presence of the external magnetic field.

The spin orbit interaction (SOI) is a relativistic interaction between spin and orbit motion of the electron, which induces a spin-asymmetric scattering of conductive electrons at a local potential caused by impurities or defects [34]. When a charge current passes through a metal in longitudinal direction, the flow of spin-up electrons is deflected to a transverse direction due to SOI while the flow of spin-down electrons is scattered to the opposite direction. As a result, a pure spin current is formed along

the transverse direction without accompanying of charge current since the numbers of spin-up and spin-down electron carriers are equal in a nonmagnetic material. This effect is called SHE. Conversely, injection of this pure spin current into a metal with SOI can also generate a transverse charge current since the spin-up and spin-down electrons flow in opposite directions are scattered into the same direction. This inverse of SHE (ISHE) results in charge accumulation in the same boundary and a transverse voltage [35]. In a ferromagnetic material, the spin-up and spin-down electrons are imbalanced in a charge current it. Therefore, the spin-dependent scattering results in not only the spin current but also the charge current in transverse direction perpendicular to both the charge current direction and magnetization direction. This effect is commonly known as anomalous Hall effect (AHE) [36,37].

The total spin and charge currents can be derived from quantum formula calculation as (here we omit the tedious derivation and directly give the equations):

$$\mathbf{J_s} = \mathbf{j_s} + \theta_{SH}(\boldsymbol{\sigma} \times \mathbf{j_c}), \tag{1.23}$$

$$\mathbf{J_c} = \mathbf{j_c} + \theta_{SH}(\boldsymbol{\sigma} \times \mathbf{j_s}), \tag{1.24}$$

where θ_{SH} is the spin Hall angel used to describe the efficiency of the charge-to-spin current conversion, $\mathbf{j_s}$ is the diffusive spin current density and $\mathbf{j_c}$ is the Ohmic charge current density. The second term in Eqs (1.23) and (1.24) are the SHE induced spin current and ISHE induced charge current, respectively. The impurity in a nonmagnetic metal produces an impurity potential which gives rise to an additional electric field *E*. When electrons pass through this electric field, they feel this electric field as an effective magnetic field, which leads to the spin orbit coupling (SOC) $\eta_{so} = (\hbar/2mc)^2$, where *m* is the mass of the electron and *c* is the velocity of the light. Two mechanisms

have been developed to explain the spin orbit scattering: side jump [38] and skew scattering[39]. Their contributions to the spin Hall angle are separately expressed as

$$\theta_{SH}^{sj} = \frac{n_{so}}{E_F}\pi n N(0) u_{imp}^2, \tag{1.25}$$

$$\theta_{SH}^{ss} = -\frac{2n_{so}}{3}\pi N(0) u_{imp}, \tag{1.26}$$

where n_{so} is the impurity density, E_F is the fermi energy and u_{imp} is the impurity potential. The total spin Hall angel is $\theta_{SH} = \theta_{SH}^{sj} + \theta_{SH}^{ss}$. In Eqs (1.23) and (1.24), $\mathbf{j_c}$ and $\mathbf{j_s}$ can be written by

$$\mathbf{j_c} = \sigma_N \mathbf{E}, \quad \mathbf{j_s} = -(\sigma_N / 2e)\nabla \delta\boldsymbol{\mu}_N, \tag{1.27}$$

where σ_N is the electrical conductivity and $\delta\boldsymbol{\mu}_N$ is the spin accumulation [25] given by

$$\delta\boldsymbol{\mu}_N(z) = 2e\theta_{SH}\rho_N\lambda_N j_c \frac{\sinh(z/\lambda_N)}{\cosh(d_N/2\lambda_N)} e_z, \tag{1.28}$$

here we assume the charge current flows in x direction and the spin current travels in z direction. The parameters ρ_N, d_N and λ_N are the resistivity, thickness, and the spin diffusion length of NM layer, respectively. The Eq (1.28) is calculated under the boundary condition that $\mathbf{J_s}$ ($z = \pm d_N/2$) = 0. However, if NM layer is neighbored by another layer the boundary condition will be different.

In this section, we have introduced the SHE and its reversal effect ISHE. The former describes the conversion of charge-to-spin currents and the latter provides a detection method of a pure spin current. Since SHE occurs inside a NM layer, it is often referred as a bulk contribution. The charge-to-spin conversion can also occur at NM/FM interface due to Rashba effect which we discuss next.

1.3.3 Rashba Effect

The Rashba effect [40,41] was first introduced in the crystals lacking an inversion center. As shown in Figure 1.3 (a), the electronic energy bands are split due

to the spin-orbit interaction and the asymmetry of the crystal potential. When the Rashba theory is applied to a system with inversion symmetry breaking such as a two-dimensional electron gas (2DEG) with structural inversion asymmetry, the SOC becomes odd in momentum *p* (reduce to linear dependence in the simplest case: 2D free electron approximation as shown in Figure 1.3 (b)). This coupling is called Rashba-type SOC [42] and its odd-in-p relation has been widely confirmed in many materials without spatial inversion symmetry.

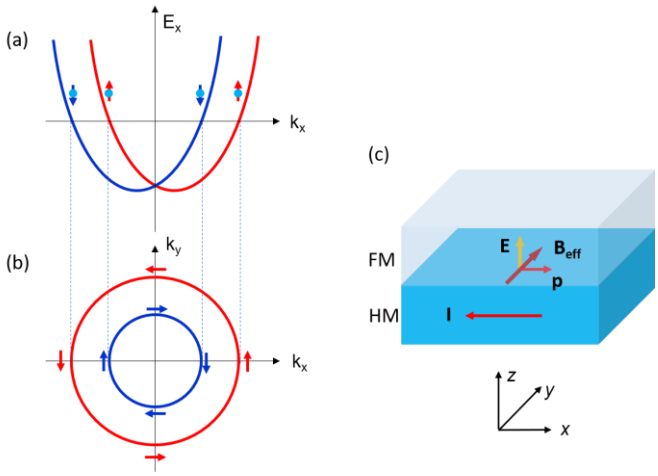

Figure 1.3 Schematics of Rashba spin splitting at interface. (a) Rashba SOC induced energy dispersion with spin-momentum locking in a one-dimensional free electron gas. The red and blue curves represent two bands carrying opposite spins. (b) Fermi surface of a two-dimensional free electron gas with locked spin angular momentum induced by Rashba spin-orbit coupling. (c) The existence of Rashba SOC at the interface of a HM/FM heterostructure.

When an electron moves across a magnetic field **B**, it owns the Zeeman energy $\mu_B \boldsymbol{\zeta} \cdot \mathbf{B}$, where μ_B is the Bohr magnetron, $\boldsymbol{\zeta}$ is the vector of Pauli matrices. If the electron moves across an electric field **E**, by analogy it also feels an effective magnetic

field proportional to $\mathbf{B_R} \sim \mathbf{E} \times \mathbf{p}$ in its rest frame due to relativistic corrections, where $\mathbf{p}$ is the momentum. This field is called spin-orbit field. In a system with structural inversion symmetry broken along the growth direction in *z* axis, it induces an electric field in *z* direction since the gradient of the crystal potential. With this, the Rashba Hamiltonian is given by

$$H_R = \frac{\alpha_R}{\hbar}(\mathbf{z} \times \mathbf{p}) \cdot \zeta , \tag{1.29}$$

$$\alpha_R \approx \hbar^2 \frac{\partial V / \partial z}{4m^2c^2} , \tag{1.30}$$

where α_R is the Rashba parameter, V is the potential, m is the mass of the electron and c is the speed of the light. In a most often used bilayer of heavy metal (HM/FM) as shown in Figure 1.3 (c), if electrons flow in *x* direction, the Rashba field $\mathbf{B_R}$, $B_R = 2\alpha_R k_F / g\mu_B$, is induced in *y* direction, where k_F is the Fermi wavevector g is the g-factor of the carriers. The emergence of the Rashba field induces the procession of the spins which initially are nonparallel to Rashba field but eventually aligned in Rashba field direction. Therefore, when a charge current flows in a HM/FM structure in which the inversion symmetry is broken in normal direction, the induced Rashba field polarizes the spins of the moving electrons in its field direction and forms the spin accumulation at the interface, this effect is called inverse spin galvanic effect(ISGE) [43,44]. As compared to the SHE induced spin accumulation and injection, spin accumulation induced by ISGE happens at the interface where the inversion symmetry is broken. Therefore, the former is classified as a bulk effect while the latter is an interfacial effect.

So far, we have discussed two mechanisms that contribute to the spin accumulation and injection at the HM/FM interface: bulk SHE and interface ISGE.

Both contributions can be treated on the same footing and there are no clear experimental methods to separate them.

1.4 Current Induced Torques

In Section 1.3 we discussed how the spin current can be generated in either FM or NM layer. The spin accumulation at the interface will result in the spin diffusion to the adjacent layer. The injected spin current in NM layer can be detected by ISHE or non-local spin valve measurement. In this section we will discuss the interaction between injected spin current and the magnetic moments in FM layer. In general, the flow of spin current in FM layer would exert torques on the magnetic moments, leading to magnetization precession or switching. According to the different methods in generating the spin current, the torques can be classified as spin transfer torque (STT) and spin orbit torque (SOT). The details about their origins and applications will be discussed in following sections.

1.4.1 Spin Transfer Torque

The concept of the STT is introduced by L. Berge [45] in 1984. The “transfer” here means the transfer of spin angular momentum between the localized magnetic moment in ferromagnet and the conduction electrons (carriers of the spins) due to the conservation of the angular momentum. This is called spin transfer effect and the torque acted on magnetization is named STT [46,47]. At the beginning it was difficult to confirm the prediction of STT because of its very small magnitude compared with other dominated factors like Oersted field induced torque. However, with the development of micro-fabrication techniques, the magnitude of STT has been extraordinarily enhanced by shrinking the device size. Especially after the discovery

of giant magneto resistance (GMR) effect in magnetic multilayers, STT attracted enormous attention as it can lead to magnetization switching which is critical in applications of spintronic devices such as magnetic random-access memory (MRAM).

We consider a sandwich structure of FM1(fixed layer)/NM/ FM2(free layer) [48,49] in Figure 1.4 (a) and assume that the magnetization $\mathbf{M_2}$ is initially tilted out of plane at a position marked by dotted arrow. As a charge current **I** is passing from FM2 to FM1, the electrons flow in opposite direction. The injected electrons carry the spins polarized in the same direction as $\mathbf{M_1}$. Since the spin polarization $\boldsymbol{\sigma}$ (*same symbol but distinct from previous conductivity*) is not parallel to $\mathbf{M_2}$, the exchange interaction between them forces the spin to align with $\mathbf{M_2}$, vice versa, the spin exerts a torque on $\mathbf{M_2}$ and force it to rotate towards the spin direction. Eventually $\mathbf{M_2}$ can be parallelly aligned to the direction of $\mathbf{M_1}$ if the injected spin current is large enough. Figure 1.4 (b) demonstrates the situation when the current is reversed. According to the ballistic model, the electrons carrying spins antiparallel to $\mathbf{M_1}$ will be reflected at the NM/FM1 interface. The reflected electrons return to FM2 and similarly the torque would rotate $\mathbf{M_2}$ clockwise. If the torque is large enough, the $\mathbf{M_2}$ can be reversed to be antiparallel to $\mathbf{M_1}$.

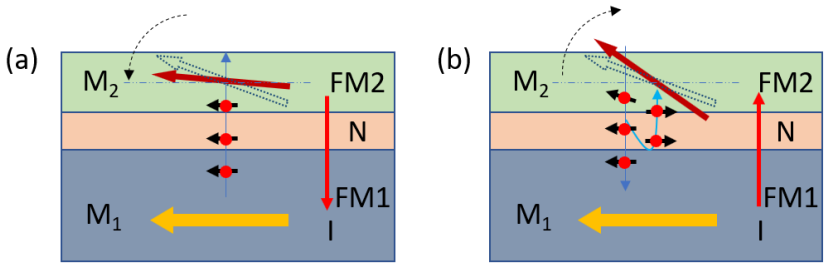

Figure 1.4 FM1/NM/FM2 trilayer with in plane magnetization M_1 (broad yellow arrow), M_2 (thin red arrow) that the dotted arrow marks the initial position of M_2. The perpendicular arrows in orange color represent the flow of charge currents. Red solid circles are electrons with black arrows indicating the spin directions. The flow of spin current is represented by blue arrow.

In Slonczewski's model [50,51], with the assumption of ideal single domain in FM1 and FM2 layers, the STT is determined by

$$\boldsymbol{\tau}_{\mathbf{STT}} = \frac{\hbar}{2e} I_s \mathbf{m_2} \times (\mathbf{m_2} \times \mathbf{m_1}), \tag{1.31}$$

where I_s is the spin current injected into FM2, $\mathbf{m_1}$ and $\mathbf{m_2}$ are the unit vectors in F1 and F2, respectively. I_s is given by [46,50]

$$I_s = \frac{I_e}{-4 + (1+P^2)(3+\mathbf{m_1}\cdot\mathbf{m_2})/4P^{3/2}}, \tag{1.32}$$

where I_e is the charge current, and P is the spin polarization. The STT enters LLG equation to describe the magnetization dynamics in free layer F2:

$$\frac{d\mathbf{M}_2}{dt} = -\gamma \mathbf{M}_2 \times \mathbf{H}_{eff} + \frac{\alpha}{M_1}(\mathbf{M}_2 \times \frac{d\mathbf{M}_2}{dt}) + \frac{\hbar}{2e} I_s \mathbf{m_2} \times (\mathbf{m_2} \times \mathbf{m_1}). \tag{1.33}$$

Here, if we consider the case that the H_{eff} is in-plane and antiparallel to $\mathbf{m_1}$, the Eq (1.33) can be simplified as

$$\frac{d\mathbf{m}_2}{dt} = -\gamma \mathbf{m}_2 \times \mathbf{H}_{eff} + \gamma(\alpha - \frac{\hbar}{2e} I_s \frac{1}{\gamma M_1 H_{eff}})(\mathbf{m}_2 \times \mathbf{m}_2 \times \mathbf{H}_{eff}). \tag{1.34}$$

where $\mathbf{M_2}$ is reduced to $\mathbf{m_2}$ by $\mathbf{m_2} = \mathbf{M_2}/ M_{2s}$. Thus, the third term in Eq (1.33) is absorbed into the second term and thus the effective damping is given by

$$\alpha_{eff} = \alpha - \frac{\hbar}{2e} I_s \frac{1}{\gamma M_1 H_{eff}}. \tag{1.35}$$

This result indicates that the STT introduces an additional damping which has opposite sign to the regular damping α. It is known that the regular damping leads to the dissipation and suppresses the magnetization precession. On the contrary, the STT introduced damping amplifies the magnetization precession for a positive I_s while suppresses the magnetization precession for negative I_s. Consequently, STT can be used to switch the free layer in the sandwich structure even without the assistance of an external magnetic field. This torque is called anti-damping-like torque. When the anti-damping-like torque overcomes the damping torque, one has $\alpha_{\text{eff}} = 0$, with this relation the critical switching current I_c can be calculated as [52]

$$I_c = \frac{2e\alpha\gamma M_1 H_{eff}}{\hbar}[-4 + (1+P^2)(3+\mathbf{m_1}\cdot\mathbf{m_2})/4P^{3/2}]. \tag{1.36}$$

1.4.2 Spin Orbit Torques

Despite of the different mechanisms between SHE and ISGE, the spin density **S** is produced at the edge of the FM layer due to the SOC. As a result, the polarized spins travel across the NM/FM interface and exert a torque on the magnetization in FM layer. This SOC induced torque can also be used to switch the magnetization in spintronic devices. We illustrate the STT-switching and SOT-switching in a magnetic tunnel junction (MTJ) [53-55] device. In Figure 1.5 (a), the polarized current flows from a reference (fixed) layer into the recording (free) layer. In this structure, the magnetization M_2 in the free layer is antiparallel to the M_1 in the fixed layer. Consequently, M_2 is switched by STT due to the exchange interaction between the

magnetic moment in free layer and the injected spin current. Here, each injected electron transfers one quantum unit of spin angular momentum to free layer. On the other hand, in SOT-switching as shown in Figure 1.5 (b), charge current is simply flowing in a nonmagnetic heavy metal (HM) layer which is adjacent to the free layer. Due to the SHE in HM layer, the generated transverse spin current travels through the interface and exert torque on the magnetization in the free layer. In addition, this mechanism enables an electron transfers more than one quantum unit because the spin angular momentum generated in between collisions gives little kick in collision or acceleration that the electron feels [34], which makes the switching in a large sample achievable.

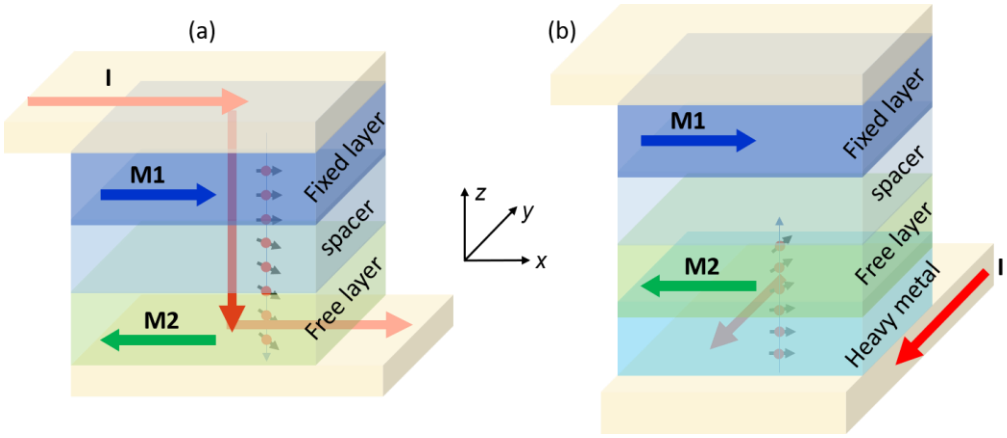

Figure 1.5 (a) Illustration of STT-switching of free layer in MTJ where charge current flows from top reference layer into bottom free layer in *z* axis. The spin direction is represented by small black arrows. (b) SOTs induced switching in MTJ device. The charge current only pass through the bottom metals.

In STT writing, the injected spins from reference layer exert no torque on magnetization in the recording layer if it is precisely parallel or antiparallel to the

magnetization in the reference layer. The misalignment is required for switching, which implies that STT relies on the thermal fluctuations of the magnetization. However, in SOT approach, the spin orientation is independent of the magnetization in reference layer and the required misalignment can be easily engineered from the fabrication. This advantage makes SOT switching more efficient than STT switching.

From the point of view of spin density, the density function theory gives the torque exerted on magnetization as

$$\mathbf{T} = -\mathbf{S} \times \mathbf{\Omega}, \tag{1.37}$$

where **S** is the spin density and **Ω** is the exchange correlation energy [56]. This relation is valid for both STT and SOT. If the SOC term is neglected in the total Hamiltonian, this relation can be equivalently expressed as the divergence of the spin current [47]:

$$\mathbf{T} = -\nabla \cdot \mathbf{j}_s, \tag{1.38}$$

This result shows that the torque is directly determined by the absorption of the spin current. On the base of two arguments above, both Rashba effect induced spin density and the SHE induced spin absorption at the NM/FM interface contribute to the SOTs.

1.4.3 Spin Hall Effect and Rashba Effect Induced SOT

SHE-SOT originates from asymmetric spin deflection induced by SOC in a nonmagnetic bulk metal. The deflected pure spin current, transverse to the electrical charge current, is subsequently absorbed in a neighboring ferromagnetic material. At first glance, this scenario is similar to STT and thus the SHE-SOT should have the analogical format in accord with Eq (1.31),

$$\mathbf{T}_{\text{SHE-SOT}} \propto [\mathbf{m} \times (\mathbf{m} \times \boldsymbol{\sigma})], \tag{1.39}$$

In the case of SHE-SOT, since magnetization feels the effective Rashba field in transverse direction, the induced torque on magnetization has the form of

$$\mathbf{T}_{\text{Rashba-SOT}} \propto \mathbf{m}\times\boldsymbol{\sigma}, \tag{1.40}$$

Therefore, SOTs includes two items named damping-like (DL) and field-like (FL) torques [57]

$$\begin{aligned}\mathbf{T} &= \mathbf{T}_{\text{DL}} + \mathbf{T}_{\text{FL}} \\ &= \tau_{\text{DL}}\mathbf{m}\times(\mathbf{m}\times\boldsymbol{\sigma}) + \tau_{\text{FL}}\mathbf{m}\times\boldsymbol{\sigma}\end{aligned}, \tag{1.41}$$

where the torque coefficients τ_{DL}, τ_{FL} may also depend on the direction of **m**.

However, it is inexact to conclude that the DL torques originates from SHE contribution while the FL torque is from the Rashba effect. Actually, the SHE-SOT induces not only the $\mathbf{T}_{\text{DL}}$ but also the $\mathbf{T}_{\text{FL}}$. The flow of spin current also yields nonequilibrium spin density at the NM/FM interface where the inversion symmetry is broken. The nonequilibrium spin density induces the effective field as in Rashba-type interface [58,59]. On the other hand, in the case of Rashba-SOT, the precessional spins around the Rashba effective field can pump the spin angular monument and induce the spins diffuse starting from the interface to FM layer, which exert a $\mathbf{T}_{\text{DL}}$ on the magnetization in FM layer [60,61]. Therefore, either SHE and Rashba effects can contribute to both $\mathbf{T}_{\text{DL}}$ and $\mathbf{T}_{\text{FL}}$ as summarized in Figure 1.6. The distinction between SOTs generated by bulk-SHE and interface-Rashba effects are experimentally challenging even though people have successfully explained some experiments by assuming that the $\mathbf{T}_{\text{DL}}$ is only contributed by SHE while $\mathbf{T}_{\text{FL}}$ exclusively originates from Rashba effect.

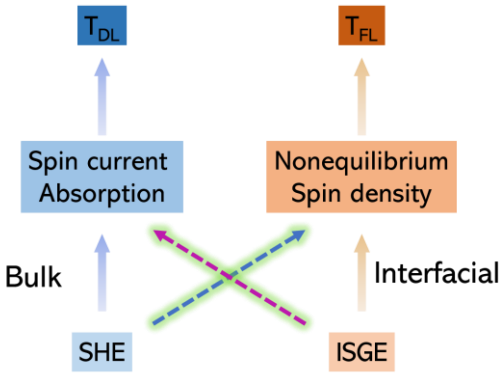

Figure 1.6 The interlaced relation of the contribution to SOTs between SHE and ISGE.

1.4.4 Faraday Rotation

Faraday effect, also called Faraday rotation discovered in 1845 by Michael Faraday [62] is a fundamental magneto-optical effect in physics. It describes a phenomenon that the polarization plane of a light has been rotated at an angle θ after the light propagates through a transparent object (solids, liquids or gases) placed in a magnetic field. The light path is in the direction parallel to the magnetic field. The rotating direction of the polarization can be found simply by analogizing to Ampere's law [63] in which light propagation path corresponds to current flow in the wire and the rotating direction corresponds to the direction of current-induced magnetic field. It is noted that this rotation is reversed if either the field or the light direction get reversed.

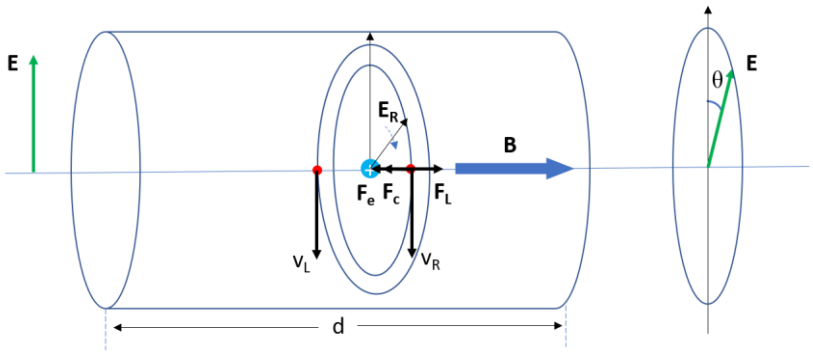

Figure 1.7 Schematics of Faraday rotation. A linearly polarized light travels through a medium with length of d. Force F_e, F_c and F_L is the forces exerted on electron due to electric field of RCL light, attractive between electron and positive center and Lorentz force, respectively. The angle θ is with respect to the E component of the incident light.

The rotating angle θ is linearly dependent on magnet field $\boldsymbol{B}$ and the thickness of the medium d in light propagation direction,

$$\theta = VBd, \tag{1.42}$$

where the coefficient V is *Verdet* constant of the medium [64]. This equation can be derived from the basic concept that a linearly polarization light is the superposition of left circularly polarized (LCP) and right circularly polarized (RCP) lights. The two light components have the same electric field amplitudes, $E_L = E_R = E$. As shown in Figure 1.7, the electrons in the medium feel the electric force $eE_{L,R} = eE$ in the radial direction and moves the electrons left/right circularly around a fixed positive charged center, where e is the elementary charge of an electron [65]. In addition, the positive center and electron form an electric dipole which also exerts a force $F_c = kr$ on the electron, where k is the coefficient and r is the radius. When magnetic field is absent in this system the equilibrium of the forces on the electron is expressed as

$eE + kr = m\omega^2 r$, where ω is the angular frequency of the circular motion and m the mass of the electron. With the presence of magnetic field $\boldsymbol{B}$ along the light propagation direction, electron feels the third force, *Lorentz* force and thus

$$eE + kr \pm e\omega rB = m\omega^2 r, \tag{1.43}$$

where the plus/minus sign of *Lorentz* force determined by the left/right rotating motion of the electron induced by LCP/ RCP light. By defining $\omega_0^2 = k/m$ and substituting it into Eq (1.43), radius of the rotating motion is obtained as

$$r_{L,R} = \frac{eE/2m}{\omega^2 - \omega_0^2 \mp e\omega B/m}. \tag{1.44}$$

This result indicates that the rotation radiuses are different for LCP and RCP lights when a magnetic field presents.

The electric dipole p moment is proportional to the radius of the circular orbit, $p = er$. In a unit volume with N dipoles, the total electric polarization is $P = Ner$. Thus the electric displacement field D can be written as $D = \varepsilon E = \varepsilon_0 E + P = \varepsilon_0 E + Ner = \varepsilon_0(1 + Ner/E\varepsilon_0)E$, where $\varepsilon_r = 1 + Ner/E\varepsilon_0$ is the relative susceptibility. In a nonmagnetic material the relative permeability μ_r is very close to 1 thus the square of refractive index can be written as $n^2 = \varepsilon_r\mu_r = \varepsilon_r = 1 + Ner/E\varepsilon_0$. From Eq (1.44), the refractive indices n_L and n_R seen by the LCP and RCP lights, respectively, are given by

$$n_{L,R}^2 = 1 + \frac{Ne^2/2m\varepsilon_0}{\omega^2 - \omega_0^2 \mp e\omega B/m}. \tag{1.45}$$

Here, the term $\mp e\omega B/m$ can be treated as a small perturbation. The Taylor's series expansion to Eq (1.45) gives

$$n_{L,R}^2 \cong n^2\left(1 \pm \frac{e\omega B/m}{\omega^2 - \omega_0^2}\right), \tag{1.46}$$

where $n^2 = 1 + \frac{Ne^2/2m\varepsilon_0}{\omega^2 - \omega_0^2}$, which is the refractive index without the presence of magnetic field. A further approximation of Eq(1.46) is given by

$$n_{L,R} \cong n(1 \pm \frac{1}{2}\frac{e\omega B/m}{\omega^2 - \omega_0^2}). \quad (1.47)$$

The difference in refractive index between LCP and RCP lights means the two lights travel through the medium at different velocities since n=c/v, which leads to a phase difference between two lights after travelling a propagation length d in the medium:

$$\Delta\varphi = \omega\Delta t = \frac{\omega d}{c}(n_L - n_R). \quad (1.48)$$

Finally, by summing up the two emergent circularly polarized lights, a linear light is formed again but its polarization direction has been rotated at an angle $\theta = \Delta\varphi/2$ with respect to its original direction. From Eqs (1.47) and (1.48), rotation angle is given by

$$\theta = \frac{ne}{2mc}(\frac{\omega^2}{\omega^2 - \omega_0^2})dB. \quad (1.49)$$

This is the detailed version of Eq (1.42). The Faraday rotation angle is proportional to the strength of the applied magnetic field and the travelling length in the medium. It should also be pointed out that the *Verdet* constant depends not only the refractive index but also the frequency of the traveling light.

1.4.5 Magneto-optical Kerr Effect

Magneto-optical Kerr Effect (MOKE), discovered in 1877 by John Kerr [66], describes the change in polarization of the incident light after the interaction with the magnetic material. Differ from Faraday effect, it discusses the polarization change after the light gets reflected from a magnetic surface instead of traveling through the material. According to the direction of the magnetization with respect to the incidence plane, there are three geometric MOKE configurations: polar, longitudinal and transverse [67] as shown in Figure 1.8.

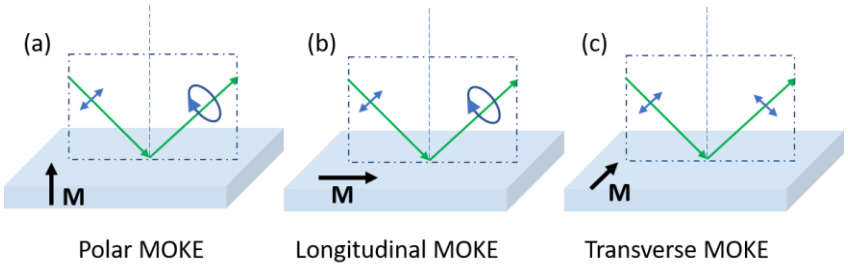

Figure 1.8 Three types of MOKE. Green arrows represent the light beam directions while blue double arrows and ellipses stand for the polarization of the incident or reflected lights.

In Figure 1.8 (a) and (b), a linear incident light becomes an elliptically polarized light after the reflection from sample surface due to MOKE. The changes in polarization and ellipticity are proportional to the surficial magnetization of the sample. Under a transverse geometry as shown in Figure 1.8 (c), the polarization status of the reflected light does not change but the magnitude of the light changes.

Similar to Faraday effect, MOKE also induce a change of light polarization after the reflection, which is called Kerr rotation. In the following, we will mathematically derive the expression of the Kerr rotation. Considering a linearly polarized light,

$$\mathbf{E} = \mathbf{E}_0 e^{i(kz-\omega t)} = [E_x, E_y, E_z] e^{i(kz-\omega t)}, \tag{1.50}$$

shines perpendicularly on a ferromagnetic material. In magnetic materials, the electric displacement **D** and the magnetic induction **B** are introduced to link the electric field **E** and magnetic field **H**, respectively.

$$\mathbf{D} = \varepsilon_0 \boldsymbol{\varepsilon}_\mathbf{r} \mathbf{E} \tag{1.51}$$

$$\mathbf{B} = \mu_0 (\mathbf{H} + \mathbf{M}) = \mu_0 \boldsymbol{\mu}_\mathbf{r} \mathbf{H}. \tag{1.52}$$

Here $\boldsymbol{\varepsilon}_\mathbf{r}$ is the permittivity tensor and $\boldsymbol{\mu}_\mathbf{r}$ is the permeability tensor. In optical frequency range, $\boldsymbol{\mu}_\mathbf{r} \sim \mathbf{1}$, where **1** is unitary tensor. Tensor $\boldsymbol{\varepsilon}_\mathbf{r}$ is a second rank tensor that fulfills the Onsanger relations $\varepsilon_{ij}(\mathbf{M}) = \varepsilon_{ij}(-\mathbf{M})$, where the subscripts $i, j = x, y, z$. In Drude-Lorentz model [68], it assumes that the electron in an atom behaves as a classical particle feeling the internal Coulomb force and the external Lorentz force induced by a uniform magnetic field $\mathbf{B}/\boldsymbol{\mu}$. By solving the equation of motion of the electron, the permittivity tensor is obtained and written as[69-71]

$$\boldsymbol{\varepsilon}_\mathbf{r} = \varepsilon \begin{bmatrix} 1 & iQ_z & -iQ_y \\ -iQ_z & 1 & iQ_x \\ iQ_y & -iQ_x & 1 \end{bmatrix}, \tag{1.53}$$

where ε is the scalar relative permittivity and Q_i, defined as $Q_i = -\varepsilon_{ij} / \varepsilon_{ii}$, is the Magneto-optical Voigt constant. Since Q_i is linearly proportional to magnetic field that the electron feels in a magnetic material, it is reasonable to substitute **B** with magnetization **M**, i.e.,

$$Q_i = Q_0 m_i, \tag{1.54}$$

where m_i is the normalized magnetization. Therefore, we can rewrite the permittivity tensor in a Cartesian basis as

$$\boldsymbol{\varepsilon}_\mathbf{r} = \varepsilon \begin{bmatrix} 1 & iQ_0\cos\theta & -iQ_0\sin\theta\sin\phi \\ -iQ_0\cos\theta & 1 & iQ_0\sin\theta\cos\phi \\ iQ_0\sin\theta\sin\phi & -iQ_0\sin\theta\cos\phi & 1 \end{bmatrix}, \tag{1.55}$$

where θ and ϕ are the polar angle and azimuth angles, respectively.

With the definition above, the Voigt constants form a vector [72] $\mathbf{Q} = [Q_x, Q_y, Q_z]$ in the Cartesian coordinate, and Eq (1.51) can be equivalently written as

$$\mathbf{D} = \varepsilon_0 \varepsilon (\mathbf{E} + i\mathbf{E} \times \mathbf{Q}). \tag{1.56}$$

It is noted that there are two orthogonal linear polarization states referred as *p* and *s* polarization. The *p*-polarized light has an electric field polarized parallel to the plane of incidence while the *s*-polarized light is perpendicular to the incidence plane. The Eq (1.56) indicates that for a *s*-polarized light the transverse magnetization component (characterized by **Q**) does not change the light polarization since $\mathbf{E_s}$ is parallel to **M** as shown in Figure 1.8 (c).

By substituting the Eq (1.56) into the following Maxwell's equations [73]

$$\nabla \cdot \mathbf{D} = \rho_f , \tag{1.57}$$

$$\nabla \cdot \mathbf{B} = 0 , \tag{1.58}$$

$$\nabla \times \mathbf{E} = -\frac{\partial \mathbf{B}}{\partial t} , \tag{1.59}$$

$$\nabla \times \mathbf{H} = j_f + \frac{\partial \mathbf{D}}{\partial t} \tag{1.60}$$

one has [we omit the free current j_f to simplify the equations]

$$\mathbf{k} \times (\mathbf{k} \times \mathbf{E}_0) = \mathbf{k}(\mathbf{k} \cdot \mathbf{E}_0) - \mathbf{E}_0(\mathbf{k} \cdot \mathbf{k}) = -\omega^2 \varepsilon_0 \mu_0 \varepsilon (\mathbf{E}_0 + i\mathbf{E}_0 \times \mathbf{Q})$$

$$\Leftrightarrow (k^2 - \frac{\omega^2 \varepsilon}{c^2})\mathbf{E}_0 = \mathbf{k}(\mathbf{k} \cdot \mathbf{E}_0) + \frac{i\omega^2 \varepsilon}{c^2}\mathbf{E}_0 \times \mathbf{Q} , \tag{1.61}$$

where $c^2 = 1/\varepsilon_0 \mu_0$. In this equation the propagation vector **k** can be solved by decomposing **k** and $\mathbf{E_0}$ in an orthogonal basis $\hat{\mathbf{e}}_s$, $\hat{\mathbf{e}}_p$ and $\hat{\mathbf{e}}_k$ (those are the unit vector along *s*, *p* and *k* axes, respectively),

$$\mathbf{k} = \begin{bmatrix} 0 \\ 0 \\ k \end{bmatrix}, \tag{1.62}$$

$$\mathbf{E}_0 = \begin{bmatrix} E_s \\ E_p \\ E_k \end{bmatrix}. \tag{1.63}$$

Now Eq (1.61) can be separated into three equations:

$$(\frac{\omega^2\varepsilon}{c^2}-k^2)E_s=\frac{i\omega^2\varepsilon}{c^2}(\mathbf{Q}\cdot\mathbf{e_p}E_k-\mathbf{Q}\cdot\mathbf{e_k}E_p), \tag{1.64}$$

$$(\frac{\omega^2\varepsilon}{c^2}-k^2)E_p=\frac{i\omega^2\varepsilon}{c^2}(\mathbf{Q}\cdot\mathbf{e_k}E_s-\mathbf{Q}\cdot\mathbf{e_s}E_k), \tag{1.65}$$

$$E_k=i(\mathbf{Q}\cdot\mathbf{e_s}E_p-\mathbf{Q}\cdot\mathbf{e_p}E_s). \tag{1.66}$$

By substituting Eq (1.66) into Eqs (1.64) and (1.65) and ignoring the terms in high order of **Q**, one obtains

$$(\frac{\omega^2\varepsilon}{c^2}-k^2)E_s+\frac{i\omega^2\varepsilon}{c^2}(\mathbf{Q}\cdot\mathbf{e_k})E_p=0, \tag{1.67}$$

$$-\frac{i\omega^2\varepsilon}{c^2}(\mathbf{Q}\cdot\mathbf{e_k})E_s+(\frac{\omega^2\varepsilon}{c^2}-k^2)E_p=0. \tag{1.68}$$

Solving Eqs (1.67) and (1.68) becomes an eigenvalue problem so we can find the nontrivial solutions of eigenvalues k_i and E_i by letting the determinant of the coefficient matrix equal to zero, which leads

$$1-\frac{c^2k^2}{\omega^2\varepsilon}=\pm\mathbf{Q}\cdot\mathbf{e_k}. \tag{1.69}$$

This equation yields four solutions for k

$$k^{\pm}=\pm k_0\sqrt{1\mp\mathbf{Q}\cdot\mathbf{e_k}}, \tag{1.70}$$

where $k_0=\frac{\omega}{c}\sqrt{\varepsilon}$. The k^+ (k^-) represents the forward (backward) mode that the light travels in +(–) $\hat{\mathbf{e}}_k$ direction. With the assumption that **Q** is small, one has

$$k^{\pm}=k_0\sqrt{1\mp\mathbf{Q}\cdot\mathbf{e_k}}\approx k_0(1\mp\frac{1}{2}\mathbf{Q}\cdot\mathbf{e_k}). \tag{1.71}$$

We rewrite the Eq (1.71) in the format of the index of refraction:

$$n=n^{\mp}=n_0(1\mp\frac{1}{2}\mathbf{Q}\cdot\mathbf{e_k}), \tag{1.72}$$

where $n_0=ck_0/\omega$. The Eq (1.72) implies that the index of refraction is affected by the introduce of magnetization (represented by **Q**) and the change is determined by the projection of **Q** along the propagation direction of the light. In addition, by

substituting Eq (1.71) back into Eqs (1.67) and (1.68) the eigenvectors can be achieved as

$$\mathbf{E}_{+1} = \begin{bmatrix} E_s^- \\ -iE_p^- \\ 0 \end{bmatrix}, \tag{1.73}$$

$$\mathbf{E}_{+2} = \begin{bmatrix} E_s^+ \\ iE_p^+ \\ 0 \end{bmatrix}, \tag{1.74}$$

where $\mathbf{E}_{+1}$ and $\mathbf{E}_{+2}$ are two eigenvectors corresponding to k^+.

To brief summarize, the wave number $k_1 = k_0(1-\mathbf{Q}\cdot\mathbf{e_k}/2)$ results in the polarization of $\mathbf{E}_{+1}$ in left-handed while $k_2 = k_0(1+\mathbf{Q}\cdot\mathbf{e_k}/2)$ results in the polarization of $\mathbf{E}_{+2}$ in right-handed. It also shows that the magnetic matter reacts different indices of refraction if the coming lights polarized in different chirality. It is known from Eq (1.72) that the LCP light decreases the index of refraction *n* by $\frac{1}{2}\mathbf{Q}\cdot\mathbf{e_k}$ while the RCP light increases *n* by $\frac{1}{2}\mathbf{Q}\cdot\mathbf{e_k}$. In addition, $\frac{1}{2}\mathbf{Q}\cdot\mathbf{e_k}$ will vanish when the incident light is normal to the material surface under the configurations of transversal and longitudinal MOKE since now the **Q** is perpendicular to the incident direction $\mathbf{e_k}$, but it still exists at polar MOKE configuration.

So far, we know in polar MOKE the magnetization in the magnetic material would result in the different index of refraction *n* seen by LCP and RCP lights, which further induces the phase difference between two light components. Therefore, a linearly polarized incident light transforms into elliptically polarized state. To characterize the polarization change, it is convenient to employ the Jones matrix in our calculation. For an elliptically polarized light traveling in *z* direction, one can write it in Jones vector [74] as

$$\mathbf{E}=\begin{bmatrix}E_x\\E_y\end{bmatrix}=\begin{bmatrix}E_{x,\max}e^{i\delta_x}\\E_{y,\max}e^{i\delta_y}\end{bmatrix}=E_{x,\max}\begin{bmatrix}1\\\dfrac{E_{y,\max}}{E_{x,\max}}e^{i(\delta_y-\delta_x)}\end{bmatrix}\Rightarrow\begin{bmatrix}1\\\tan\Theta e^{i\delta}\end{bmatrix}, \tag{1.75}$$

where $\delta=\delta_y-\delta_x$ represents the phase difference between x and y components. Angle Θ is defined in Figure 1.9 and $\tan\Theta$ is the ratio of the maximum projection of E on y and x axes. Thus, the s and p polarized lights are written as

$$\mathbf{e}_s=\begin{bmatrix}1\\0\end{bmatrix},\ \mathbf{e}_p=\begin{bmatrix}0\\1\end{bmatrix}, \tag{1.76}$$

and the LCP and RCP lights are given by

$$\mathbf{e}_L=\frac{1}{\sqrt{2}}\begin{bmatrix}1\\i\end{bmatrix},\ \ \mathbf{e}_R=\frac{1}{\sqrt{2}}\begin{bmatrix}1\\-i\end{bmatrix}. \tag{1.77}$$

The MOKE study the change of light after the reflection from the magnetic sample. The effect of the sample to the light can be mathematically expressed in a 2×2 matrix. Here, we employ the matrix of the complex Fresnel reflection [75] given by

$$F^R=\begin{bmatrix}r_{ss}&r_{sp}\\r_{ps}&r_{pp}\end{bmatrix}, \tag{1.78}$$

where the subscript sp(ps) means the s(p)-polarized component induced by incident p(s) polarized light. Assuming a s-polarized light gets reflected from a magnetic material, the reflected light $\mathbf{E}_r$ could be obtained from the product of Eqs (1.76) and (1.78):

$$\mathbf{E}_r=\begin{bmatrix}r_{ss}&r_{sp}\\r_{ps}&r_{pp}\end{bmatrix}\begin{bmatrix}1\\0\end{bmatrix}=\begin{bmatrix}r_{ss}\\r_{ps}\end{bmatrix}=r_{ss}\begin{bmatrix}1\\\dfrac{r_{ps}}{r_{ss}}\end{bmatrix}\Rightarrow\begin{bmatrix}1\\\dfrac{r_{ps}}{r_{ss}}\end{bmatrix}. \tag{1.79}$$

Then we compare Eq (1.79) with Eq (1.75) and it yields the Kerr angle

$$\tan\Theta e^{i\delta}=\frac{r_{ps}}{r_{ss}}. \tag{1.80}$$

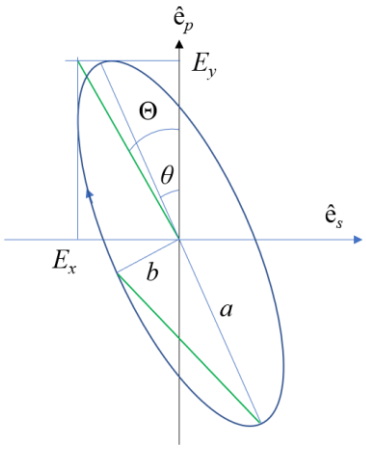

Figure 1.9. Schematic of elliptical polarization light. The orientation of the ellipse is given by the angle θ which is the angle of semi-major axis with respect to the *s*-axis. The length of semi-major and minor axes of the ellipse are *a* and *b*, respectively.

From the geometry relation in Figure 1.9, the Kerr angle is calculated as

$$\phi_K = \tan\Theta e^{i\delta} = \frac{E_{y,\max}}{E_{x,\max}} e^{i\delta} = \frac{\tan\theta - i\tan\eta}{1 + i\tan\theta\tan\eta} \approx \tan\theta - i\tan\eta \cong \theta - i\eta\,, \qquad (1.81)$$

where θ is called Kerr rotation and $\eta = b/a$ is the Kerr ellipticity [76]. In Eq (1.81) the term $i\tan\theta\tan\eta$ has been neglected because both θ and η are small quantities. The comparison between Eq (1.80) and Eq (1.81) shows that Kerr rotation and ellipticity correspond to the real and imaginary part of the r_{ps}/r_{ss} for a *s*-polarized light:

$$\theta = \mathrm{Re}\left[\frac{r_{ps}}{r_{ss}}\right],\ \eta = \mathrm{Im}\left[\frac{r_{ps}}{r_{ss}}\right]. \qquad (1.82)$$

It is known that any linearly polarized light can be decomposed as a superposition of two circularly polarized lights, i.e., LCP + RCP with $E_L = E_R$. And any elliptically polarized light can be decomposed as a combination of two linearly polarized lights with different amplitudes and phase, which means elliptically polarized light can be further written as the combination of LCP and RCP lights with

different amplitudes and phases. Therefore, the Kerr rotation is achieved by examining the following two basic vectors written by

$$\mathbf{e}'_L = \begin{bmatrix} 1 \\ i \end{bmatrix} e^{i\delta^-}, \ \mathbf{e}'_R = \begin{bmatrix} 1 \\ -i \end{bmatrix} e^{i\delta^+}, \tag{1.83}$$

where δ^- is the induced phase to LCP after the interaction with magnetization while δ^+ is for RCP, namely $\delta^+=(n^+\omega/c)z$; $\delta^-=(n^-\omega/c)z$ and z is the travelling distance. The combination is calculated by summing the two matrices in Eq (1.83),

$$\mathbf{e}'_L + \mathbf{e}'_R = \begin{bmatrix} e^{i\delta^-} \\ ie^{i\delta^-} \end{bmatrix} + \begin{bmatrix} e^{i\delta^+} \\ -ie^{i\delta^+} \end{bmatrix} = \begin{bmatrix} e^{i\delta^-} + e^{i\delta^+} \\ ie^{i\delta^-} - ie^{i\delta^+} \end{bmatrix}. \tag{1.84}$$

Finally, the Kerr rotation is calculated from Eq (1.84) as

$$\begin{aligned} \tan\theta &= \frac{ie^{i\delta^-} - ie^{i\delta^+}}{e^{i\delta^-} + e^{i\delta^+}} \\ &= \frac{i[\cos\delta^- - \cos\delta^+ + i(\sin\delta^- - \sin\delta^+)]}{\cos\delta^- + \cos\delta^+ + i(\sin\delta^- + \sin\delta^+)} \\ &= -\frac{(\cos\frac{\delta^- + \delta^+}{2} + i\sin\frac{\delta^- + \delta^+}{2})\sin\frac{\delta^- - \delta^+}{2}}{(\cos\frac{\delta^- + \delta^+}{2} + i\sin\frac{\delta^- + \delta^+}{2})\cos\frac{\delta^- - \delta^+}{2}} \\ &= -\tan\frac{\delta^- - \delta^+}{2} \end{aligned} . \tag{1.85}$$

The Kerr rotation can be approximately written as

$$\theta = -\frac{\delta^- - \delta^+}{2} = \frac{\omega}{2c}(n^+ - n^-)z . \tag{1.86}$$

By substituting Eq (1.72) into Eq (1.86),

$$\theta = \frac{\omega n_0 z}{2c}\mathbf{Q}\cdot\mathbf{e}_\mathbf{k} = k_0 z Q_0 m_z . \tag{1.87}$$

Now it is clear to see from Eq (1.87) that the Kerr rotation is linearly dependent on the magnetization component in perpendicular direction. On the other hand, the origin of the ellipticity is from the imaginary part of the complex index of

refraction, which can also be proven using the similar method. Based on this nature, MOKE technique has been well developed as a powerful and convenient magnetometry for detecting the perpendicular magnetization of a magnetic material.

So far, we discussed that the Kerr rotation can be used to detect the perpendicular magnetization. Meanwhile, it is also capable to detect the in plane magnetization if we consider the second order of the complex permittivity tensor [72] as following:

$$\boldsymbol{\varepsilon}_{\mathbf{r}} = \varepsilon \begin{bmatrix} 1 & iQ_z & -iQ_y \\ -iQ_z & 1 & iQ_x \\ iQ_y & -iQ_x & 1 \end{bmatrix} + \begin{bmatrix} B_1 m_x^2 & B_2 m_x m_y & B_2 m_x m_z \\ B_2 m_x m_y & B_1 m_y^2 & B_2 m_y m_z \\ B_2 m_x m_z & B_2 m_y m_z & B_1 m_z^2 \end{bmatrix}, \tag{1.88}$$

where the second term is due to Voigt effect and associated with the quadratic MOKE. The quadratic MOKE is typically much smaller than polar MOKE in magnitude. In Eq (1.88), B_1 and B_2 are constant coefficients and $B_1 = B_2 = B$ in the spherical approximation. For an in plane magnetized sample that m_z=0, Eq (1.88) reduces to

$$\boldsymbol{\varepsilon}_{\mathbf{r}} = \varepsilon \begin{bmatrix} 1 & 0 & -iQ_y \\ 0 & 1 & iQ_x \\ iQ_y & -iQ_x & 1 \end{bmatrix} + B \begin{bmatrix} m_x^2 & m_x m_y & 0 \\ m_x m_y & m_y^2 & 0 \\ 0 & 0 & 0 \end{bmatrix}. \tag{1.89}$$

By applying second term in Eq (1.89) the similar algebraic operation that we used for polar MOKE, one can obtain its eigenvectors E_{Q1}= [1, 1, 0] and E_{Q2}= [1, −1, 0]. Also, the contribution of the quadratic term to the polarization rotation is proportional to $m_x m_y$.

In summary, the total Kerr rotation is given by

$$\theta(\mathbf{m}) = \alpha_{Polar} m_z + \beta_{Quadratic} m_x m_y + \cdots, \tag{1.90}$$

where α_{Polar} and $\beta_{\text{Quadratic}}$ are the coefficients for polar and quadratic MOKE, respectively.

REFERENCES

[1] S. Bader and S. Parkin,"*Spintronics*", Annu. Rev. Condens. Matter Phys. **1**, 71 (2010).

[2] I. Žutić, J. Fabian, and S. D. Sarma,"*Spintronics: Fundamentals and applications*", Reviews of modern physics **76**, 323 (2004).

[3] M. N. Baibich, J. M. Broto, A. Fert, F. N. Van Dau, F. Petroff, P. Etienne, G. Creuzet, A. Friederich, and J. Chazelas,"*Giant magnetoresistance of (001) Fe/(001) Cr magnetic superlattices*", Physical review letters **61**, 2472 (1988).

[4] G. Binasch, P. Grünberg, F. Saurenbach, and W. Zinn,"*Enhanced magnetoresistance in layered magnetic structures with antiferromagnetic interlayer exchange*", Physical review B **39**, 4828 (1989).

[5] J. Mathon and A. Umerski,"*Theory of tunneling magnetoresistance of an epitaxial Fe/MgO/Fe (001) junction*", Physical Review B **63**, 220403 (2001).

[6] Y. Wang, R. Ramaswamy, and H. Yang,"*FMR-related phenomena in spintronic devices*", Journal of Physics D: Applied Physics **51**, 273002 (2018).

[7] J. Sinova, S. O. Valenzuela, J. Wunderlich, C. Back, and T. Jungwirth,"*Spin hall effects*", Reviews of Modern Physics **87**, 1213 (2015).

[8] P. Li *et al.*,"*Spin–orbit torque-assisted switching in magnetic insulator thin films with perpendicular magnetic anisotropy*", Nature communications **7**, 1 (2016).

[9] X. Fan, J. Wu, Y. Chen, M. J. Jerry, H. Zhang, and J. Q. Xiao,"*Observation of the nonlocal spin-orbital effective field*", Nature communications **4**, 1 (2013).

[10] X. Fan, A. R. Mellnik, W. Wang, N. Reynolds, T. Wang, H. Celik, V. O. Lorenz, D. C. Ralph, and J. Q. Xiao,"*All-optical vector measurement of spin-*

orbit-induced torques using both polar and quadratic magneto-optic Kerr effects", Applied Physics Letters **109**, 122406 (2016).

[11] P. T. Callaghan, *Principles of nuclear magnetic resonance microscopy* (Oxford University Press on Demand, 1993).

[12] R. Grün,"*Electron spin resonance (ESR) dating*", Quaternary International **1**, 65 (1989).

[13] G. Rado and J. Weertman,"*Spin-wave resonance in a ferromagnetic metal*", Journal of Physics and chemistry of solids **11**, 315 (1959).

[14] M. Farle,"*Ferromagnetic resonance of ultrathin metallic layers*", Reports on progress in physics **61**, 755 (1998).

[15] L. Faddeev and L. Takhtajan,"*What is the spin of a spin wave?*", Physics Letters A **85**, 375 (1981).

[16] B. Guo and M.-C. Hong,"*The Landau-Lifshitz equation of the ferromagnetic spin chain and harmonic maps*", Calculus of Variations and Partial Differential Equations **1**, 311 (1993).

[17] T. L. Gilbert,"*A phenomenological theory of damping in ferromagnetic materials*", IEEE transactions on magnetics **40**, 3443 (2004).

[18] D. Jiles, *Introduction to magnetism and magnetic materials* (CRC press, 2015).

[19] J. M. Coey, *Magnetism and magnetic materials* (Cambridge university press, 2010).

[20] S. V. e. Von Sovskii, *Ferromagnetic resonance: the phenomenon of resonant absorption of a high-frequency magnetic field in ferromagnetic substances* (Elsevier, 2016).

[21] C. Kittel,"*Interpretation of anomalous Larmor frequencies in ferromagnetic resonance experiment*", Physical Review **71**, 270 (1947).

[22] A. Aharoni,"*Demagnetizing factors for rectangular ferromagnetic prisms*", Journal of applied physics **83**, 3432 (1998).

[23] P. Sharma,"*How to create a spin current*", Science **307**, 531 (2005).

[24] M. Johnson and R. H. Silsbee,"*Interfacial charge-spin coupling: Injection and detection of spin magnetization in metals*", Physical review letters **55**, 1790 (1985).

[25] S. Takahashi and S. Maekawa,"*Spin current, spin accumulation and spin Hall effect*", Science and Technology of Advanced Materials **9**, 014105 (2008).

[26] S. Maekawa, S. O. Valenzuela, E. Saitoh, and T. Kimura, *Spin current* (Oxford University Press, 2017), Vol. 22.

[27] V. K. Arora,"*Drift diffusion and Einstein relation for electrons in silicon subjected to a high electric field*", Applied Physics Letters **80**, 3763 (2002).

[28] K. Ando, T. Yoshino, and E. Saitoh,"*Optimum condition for spin-current generation from magnetization precession in thin film systems*", Applied Physics Letters **94**, 152509 (2009).

[29] J. Hirsch,"*Spin hall effect*", Physical Review Letters **83**, 1834 (1999).

[30] K. Ando *et al.*,"*Inverse spin-Hall effect induced by spin pumping in metallic system*", Journal of applied physics **109**, 103913 (2011).

[31] O. Mosendz, J. Pearson, F. Fradin, G. Bauer, S. Bader, and A. Hoffmann,"*Quantifying spin Hall angles from spin pumping: Experiments and theory*", Physical review letters **104**, 046601 (2010).

[32] S. Nonoguchi, T. Nomura, and T. Kimura,"*Nonlocal spin transports in nanopillar-based lateral spin valve*", Applied Physics Letters **100**, 132401 (2012).

[33] Ï. Î. J. Christenson,"*POSSIBILITY OF ORIENTING ELECTRON SPINS WITH CURRENT*", Phys. Rev. Lett **25**, 3l6 (1970).

[34] A. Manchon, J. Železný, I. M. Miron, T. Jungwirth, J. Sinova, A. Thiaville, K. Garello, and P. Gambardella,"*Current-induced spin-orbit torques in ferromagnetic and antiferromagnetic systems*", Reviews of Modern Physics **91**, 035004 (2019).

[35] E. Saitoh, M. Ueda, H. Miyajima, and G. Tatara,"*Conversion of spin current into charge current at room temperature: Inverse spin-Hall effect*", Applied physics letters **88**, 182509 (2006).

[36] N. Nagaosa, J. Sinova, S. Onoda, A. H. MacDonald, and N. P. Ong,"*Anomalous hall effect*", Reviews of modern physics **82**, 1539 (2010).

[37] T. Jungwirth, Q. Niu, and A. H. MacDonald,"*Anomalous Hall effect in ferromagnetic semiconductors*", Physical review letters **88**, 207208 (2002).

[38] L. Berger,"*Side-jump mechanism for the Hall effect of ferromagnets*", Physical Review B **2**, 4559 (1970).

[39] Y. Niimi, Y. Kawanishi, D. Wei, C. Deranlot, H. Yang, M. Chshiev, T. Valet, A. Fert, and Y. Otani,"*Giant spin Hall effect induced by skew scattering from bismuth impurities inside thin film CuBi alloys*", Physical review letters **109**, 156602 (2012).

[40] F. Vas'ko,"*Spin splitting in the spectrum of two-dimensional electrons due to the surface potential*", JETP Lett **30**, 541 (1979).

[41] Y. A. Bychkov and E. I. Rashba,"*Oscillatory effects and the magnetic susceptibility of carriers in inversion layers*", Journal of physics C: Solid state physics **17**, 6039 (1984).

[42] Q. Song, H. Zhang, T. Su, W. Yuan, Y. Chen, W. Xing, J. Shi, J. Sun, and W. Han,"*Observation of inverse Edelstein effect in Rashba-split 2DEG between SrTiO3 and LaAlO3 at room temperature*", Science advances **3**, e1602312 (2017).

[43] S. Ganichev, E. Ivchenko, V. Bel'Kov, S. Tarasenko, M. Sollinger, D. Weiss, W. Wegscheider, and W. Prettl,"*Spin-galvanic effect*", Nature **417**, 153 (2002).

[44] I. Garate and M. Franz,"*Inverse spin-galvanic effect in the interface between a topological insulator and a ferromagnet*", Physical review letters **104**, 146802 (2010).

[45] L. Berger,"*Exchange interaction between ferromagnetic domain wall and electric current in very thin metallic films*", Journal of Applied Physics **55**, 1954 (1984).

[46] M. D. Stiles and A. Zangwill,"*Anatomy of spin-transfer torque*", Physical Review B **66**, 014407 (2002).

[47] D. C. Ralph and M. D. Stiles,"*Spin transfer torques*", Journal of Magnetism and Magnetic Materials **320**, 1190 (2008).

[48] F. J. Jedema, A. Filip, and B. Van Wees,"*Electrical spin injection and accumulation at room temperature in an all-metal mesoscopic spin valve*", Nature **410**, 345 (2001).

[49] B. Diény,"*Giant magnetoresistance in spin-valve multilayers*", Journal of Magnetism and Magnetic Materials **136**, 335 (1994).

[50] J. C. Slonczewski,"*Current-driven excitation of magnetic multilayers*", Journal of Magnetism and Magnetic Materials **159**, L1 (1996).

[51] J. C. Slonczewski,"*Conductance and exchange coupling of two ferromagnets separated by a tunneling barrier*", Physical Review B **39**, 6995 (1989).

[52] J. Sun,"*Current-driven magnetic switching in manganite trilayer junctions*", Journal of Magnetism and Magnetic Materials **202**, 157 (1999).

[53] Q. Qi, X. Shi, and M. R. Gibbons, (Google Patents, 2004).

[54] S. Tehrani *et al.*,"*Recent developments in magnetic tunnel junction MRAM*", IEEE Transactions on magnetics **36**, 2752 (2000).

[55] Q. Qi and X. Shi, (Google Patents, 2003).

[56] A. Manchon and S. Zhang,"*Theory of nonequilibrium intrinsic spin torque in a single nanomagnet*", Physical Review B **78**, 212405 (2008).

[57] P. M. Haney, H.-W. Lee, K.-J. Lee, A. Manchon, and M. D. Stiles,"*Current induced torques and interfacial spin-orbit coupling: Semiclassical modeling*", Physical Review B **87**, 174411 (2013).

[58] V. P. Amin and M. D. Stiles,"*Spin transport at interfaces with spin-orbit coupling: Formalism*", Physical Review B **94**, 104419 (2016).

[59] V. Amin and M. Stiles,"*Spin transport at interfaces with spin-orbit coupling: Phenomenology*", Physical Review B **94**, 104420 (2016).

[60] I. M. Miron, G. Gaudin, S. Auffret, B. Rodmacq, A. Schuhl, S. Pizzini, J. Vogel, and P. Gambardella,"*Current-driven spin torque induced by the Rashba effect in a ferromagnetic metal layer*", Nature materials **9**, 230 (2010).

[61] I. M. Miron *et al.*,"*Fast current-induced domain-wall motion controlled by the Rashba effect*", Nature materials **10**, 419 (2011).

[62] M. Faraday,"*X. The Bakerian Lecture.—Experimental relations of gold (and other metals) to light*", Philosophical Transactions of the Royal Society of London, 145 (1857).

[63] G. Cavalleri, G. Spavieri, and G. Spinelli,"*The ampere and biot-savart force laws*", european Journal of Physics **17**, 205 (1996).

[64] P. Bhattacharya, R. Fornari, and H. Kamimura, *Comprehensive Semiconductor Science and Technology: Online Version* (Newnes, 2011).

[65] T. Haider,"*A review of magneto-optic effects and its application*", International Journal of Electromagnetics and Applications **7**, 17 (2017).

[66] J. Kerr,"*XLIII. On rotation of the plane of polarization by reflection from the pole of a magnet*", The London, Edinburgh, and Dublin Philosophical Magazine and Journal of Science **3**, 321 (1877).

[67] A. Stupakiewicz, A. Chizhik, M. Tekielak, A. Zhukov, J. Gonzalez, and A. Maziewski,"*Direct imaging of the magnetization reversal in microwires using all-MOKE microscopy*", Review of Scientific Instruments **85**, 103702 (2014).

[68] N. Ashcroft and N. Mermin,"*Solid state physics (brooks cole, 1976)*", Cited on **26** (1993).

[69] Z. Qiu and S. D. Bader,"*Surface magneto-optic Kerr effect*", Review of Scientific Instruments **71**, 1243 (2000).

[70] W. Voigt, *Magneto-und elektrooptik* (BG Teubner, 1908), Vol. 3.

[71] S. Bader,"*Smoke*", Journal of magnetism and magnetic materials **100**, 440 (1991).

[72] A. Hubert and R. Schäfer, *Magnetic domains: the analysis of magnetic microstructures* (Springer Science & Business Media, 2008).

[73] D. Fleisch, *A student's guide to Maxwell's equations* (Cambridge University Press, 2008).

[74] R. C. Jones,"*A new calculus for the treatment of optical systemsi. description and discussion of the calculus*", Josa **31**, 488 (1941).

[75] Š. Višňovský,"*Optics of magnetic multilayers*", Czechoslovak journal of physics **41**, 663 (1991).

[76] M. Nývlt,"*Optical interactions in ultrathin magnetic film structures*", Dizertační práce, Univerzita Karlova, Praha, srpen (1996).

Chapter 2

SPINTRONIC DEVICE FABRICATION AND CHARACTERIZATION

In this chapter, we introduce the fabrication and characterization of the spintronic devices employed in this research. We used magnetron sputtering and e-beam evaporation techniques to fabricate films and heterostructures using this research. Devices were fabricated using standard lithograph techniques. The basic magnetic properties of the magnetic materials are characterized by vibrating sample magnetometer, FMR or MOKE technique. Both electrical transport measurements and MOKE measurements have been used to detect the SOTs in magnetic heterostructures. The magnetization dynamics are also simulated using two micromagnetic simulation software, OOMMF and MuMax3.

2.1 Magnetic Films Deposition

Thin film technology plays an important role in design and manufacture of semiconductor devices and novel spintronic devices. In this section, we mainly introduce two physical-vapor deposition (PVD) techniques for magnetic film fabrication: sputtering and evaporation. The techniques of sputtering and evaporation were developed in the middle to late 1800s [1,2]. Sputter deposition is excellent for materials with high melting points. Magnetron sputtering is also a versatile way to create very dense films with good adhesion on a substrate or wafer. It has excellent precision control of film thickness and density. It is suitable for metallic or insulating coating with specific optical or electrical properties. Thermal evaporation is the

simplest form of PVD. It uses a resistive heat source to evaporate a source material within a chamber. This process is a good choice for materials with lower melting temperature. But for materials with high melting temperature, electron-beam (or e-beam) evaporation is much better than thermal evaporation because it allows direct transfer of a larger amount of energy into the source material than thermal evaporation. While magnetron sputtering is more versatile and have better control on film thicknesses, e-beam evaporation offers a higher material utilization efficiency and higher deposition rates. One of a key features for e-beam deposition is that it offers "line-of-sight" (directional) deposition, which are used to develop certain devices via shadow mask technique.

2.1.1 Magnetron Sputtering

Sputtering technique was first reported in 1852 by William Robert Grove and developed as a thin film deposition technology by Kenneth Kingdon and Irving Langmuir in 1923 [3]. Nowadays sputtering technique has been wildly used in semiconductor industries and research laboratories. The basic schematic of a magnetron sputtering system is shown in Figure 2.1. In a high vacuum chamber, a high voltage is applied between cathode (target) and anode (substrate) to ionize a sputtering gas such as Ar. The Ar^+ ions and electrons are accelerated towards the target and anode, respectively. The accelerated electron will collide with Ar atoms and promote ionization of Ar.

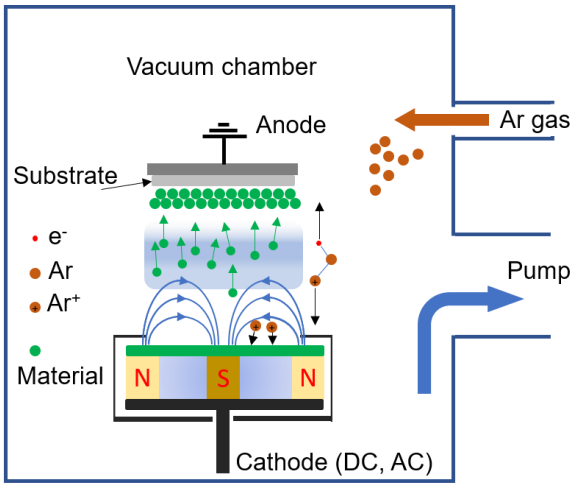

Figure 2.1 Schematic of a magnetron sputtering system. The representatives of the particles are listed on the left-hand side of the picture. Blue curves are the magnetic field lines produced by the permanent magnets. The green rectangle represents the target to be sputtered.

The bombardment of Ar^+ ions on target surface leads to energy and momentum transfer from ions to the target materials and knock off atoms of the target. These atoms travel to the anode and condense on the substrate to form a thin film [4]. Since Ar^+ ions are charged particles, their travelling path and velocity can be controlled by magnetic field produced by permanent magnets behind the negative cathode. Moreover, the magnetic field can also trap electrons over the negatively charged target due to the *Lorentz* force. This confinement not only enhances the deposition rate, but also prevent electrons from hitting the films deposited on substrate, thus reducing the damage of films due to high energic electrons.

There are several factors that affect the sputtering deposition rate such as the angle of incidence ions, incident ion energy, pressure of ion gas and the type of targets. The distribution of the ejected atoms shows a cosine-like relation with the incident angle that is defined with respect to the normal direction. The deposition rate

is not simply proportional to the ion gas pressure but reaches a maximum at a crucial pressure point. A lower pressure induces less scattering of sputtering-off particles while a higher pressure leads to more collisions. Since the collisions happen not only on target but also on the substrate surfaces, the previously coated film on the substrate possibly could be struck by those extra collisions, which to some extent decreases the deposition rate.

DC power supply is widely used for sputtering metallic materials. As for insulating target like oxides, it is difficult for Ar^+ ions to discharge through the oxides after bombardments. As a result, Ar^+ ions start to accumulate on target surface and gradually build up an electromotive force, which makes further bombarding on the target surface difficult. However, this problem can be solved by replacing DC power with a RF power supply which neutralizes the charge accumulation. Because electron has higher mobility than ion, more electrons reach at the insulating target surface than ions after a cycle of RF potential (positive half plus negative half). Hence the target becomes negatively self-biased which rejects electrons but confines a cluster of positive ions near the target surface. These ions will continue bombarding the target to form a continuous sputtering. Typically, an empirical frequency 13.56 MHz is the most used frequency for RF sputtering [4-6], and an impedance matching between the power supply and the chamber is required.

2.1.2 Electron-beam Evaporation System

Differing from well-known thermal evaporation, e-beam evaporation uses electrons beam with high energy to heat up the target material. The electrons in an e-beam evaporation system are generated from a charged filament and focused in strong magnetic field to form a directional electron beam [7-9]. In a high vacuum

environment as shown in Figure 2.2, when the target material is heated by electron beam, its surface atoms or molecules will leave the source surface once they acquire enough thermal energy. The evaporated atoms or molecules then travel in vacuum chamber and condense on the substrate.

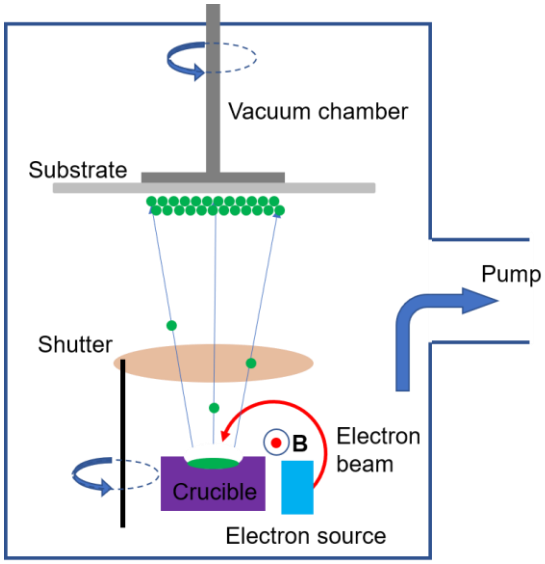

Figure 2.2 Schematic of an Electron-beam evaporator. The material being evaporated is marked by green color.

E-beam evaporation technique has several advantages. First, as mentioned before the source material can be heated up to a much higher temperature than thermal evaporation, which enables the evaporation of the materials with high melting point. Secondly, e-beam evaporation yields significantly higher deposition rates in a broad range from as low as 0.1nm/min to as high as 100nm/min. Thirdly, the flux of evaporated has better uniformity and directionality than sputtering method. This is because the evaporated atoms in e-beam system have a longer travelling path between the crucible and substrate, which significantly reduces the ratio of substrate area to the

area of spherical flux. This advantage makes e-beam evaporation very suitable for shadow mask deposition. Lastly, e-beam evaporation introduces very low degree of contamination from the crucible since it only heats the target source material instead of the entire crucible.

2.2 Vibrating Sample Magnetometer

Vibrating sample magnetometer [10] (VSM) is a standard instrument that measures the magnetic properties of materials. A simple schematic diagram of a VSM instrument is shown in Figure 2.3 where the sample fixed on a vibrating rob is placed at the center of a uniform static magnetic field. Due to the Faraday laws, moving magnetic sample in magnetic field induces the change of magnetic flux that can be captured by the pick-up coils. The detected signal is output in the format of electrical voltage. The induced voltage is proportional to the sample's magnetic moment. The lock-in amplifier is employed to measure the voltage signal by locking the reference signal to the frequency of sample vibrating. By sweeping the magnetic field back and forth, VSM measures a magnetic moment as a function of field, i.e., the magnetic hysteresis loop.

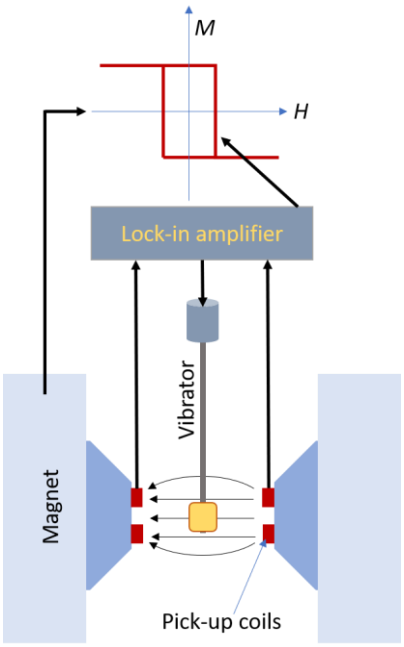

Figure 2.3 Schematic of a VSM. The yellow square is the sample under test. Four red rectangles fixed around the center of magnet poles are used to pick up the moment signal from the oscillating magnetic sample.

VSMs manufactured by Lake Shore Cryotronics or Quantum Design are widely used in many research laboratories for basic magnetic property characterizations. VSM made by Lake Shore has the similar configuration as shown in Figure 2.3. It is convenient to perform angle dependent measurements for thin film samples. However, the vibrating sample is in an open space, which limits its extension to temperature dependent measurement. This shortcoming is overcome in the VSM made by Quantum Design (QD). It has a closed chamber for the sample under test, the shield feature not only promises the temperature dependent measurements but also increases the signal accuracy since it eliminates the environmental noise perturbation. Another advantage of QD-VSM is its high field capability of about several tesla. The

disadvantage of this product is the limitation on angle dependent measurement because the field direction is parallel to the vibrating rod.

2.3 Ferromagnetic Resonant Measurement

A common FMR instrument consists of a microwave resonant cavity in an electromagnet. The sample is placed inside the cavity and illuminated within microwaves at a specific frequency *f*. The precession frequency f_0 of the magnetization can be tuned by scanning the applied magnetic field. If the resonant condition is satisfied at $f_0 = f$, the energy absorption of the sample from microwaves reaches the maximum. The main advantage of this cavity method is its high sensitivity. The major shortcoming is its narrow frequency. For broad frequency measurement, transmission lines such as striplines and co-planar waveguides (CPW) [11] are often used. A schematic diagram of a vector network analyzer FMR ((VNA-FMR in short) spectrometer is shown in Figure 2.4, where the magnetic thin film is placed on top of a CPW where its transmission line (S) and ground line (G) are connected to the VNA. Microwave current flows through the S line and generates a *rf* magnetic field that drives the precession motion of the magnetization in the sample. The microwave absorption spectrums can be obtained by measuring the S parameters in scanning dc magnetic field *H* at a fixed *f* or scanning *f* at a fixed *H*. The effective susceptibility of the sample can be characterized by the relationship: $\chi(H)=a\cdot\log[S_{12}(H)]$ where *a* is a constant [12]. The field and frequency corresponding to the absorption peak in the measured FMR spectrum are called resonant field and resonant frequency, respectively.

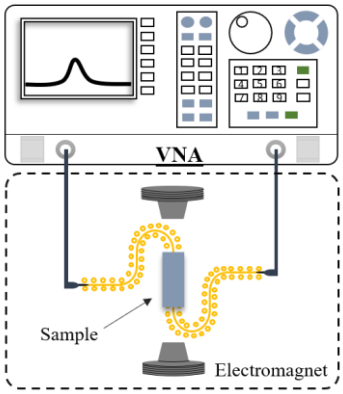

Figure 2.4 Typical FMR measurement system including a two ports VNA, CPW (yellow line) mounted on a stage with two SMA launchers connected at the two ends of the CPW. Electromagnet is used to applied external magnetic field along an in-plane direction of the film sample.

Near the resonance condition, one can take the approximation that $\omega_0 \approx \omega$ in Eq (1.8). Thus, the imaginary part of the off-diagonal element in susceptibility tensor becomes

$$\chi''_{xy} = \frac{-2\omega_m\omega_0\alpha\omega^2}{(\omega_0^2-\omega^2)^2+4\omega_0^2\alpha^2\omega^2} \approx -\frac{\omega_m}{2}\frac{\alpha\omega_0}{(\omega-\omega_0)^2+\alpha^2\omega_0^2}. \quad (2.1)$$

In this formula, $\chi''_{xy}(\omega)$ shows a *Lorentz* relationship with the frequency ω, which can be used to fit the measured frequency dependent FMR spectrum. The Eq (2.1) can also be written as a function of H by substituting $\gamma\Delta H_0/\alpha = \omega_0$ and $\gamma\Delta H/\alpha = \omega$ [13] into Eq (2.1),

$$\chi''_{xy} = \frac{-2\omega_m\omega_0\alpha\omega^2}{(\omega_0^2-\omega^2)^2+4\omega_0^2\alpha^2\omega^2} \approx -\frac{\omega_m}{2}\frac{\alpha\omega}{(\omega-\omega_0)^2+\alpha^2\omega^2} = -\frac{\omega_m}{2}\frac{\Delta H}{(H-H_0)^2+(\Delta H)^2} \quad , \tag{2.2}$$

where ΔH is the line width of FMR peak at half maximum and H_0 is the resonant field. This *Lorentz* type formula is often used to fit the FMR data to obtain resonant field and damping of the material.

2.4 Spintronic Device Fabrication

Device fabrication is an important part in spintronics related experiments. Standard lithography techniques have been widely used in fabricating devices in this research. In general, the lithography techniques can be categorized as mask and maskless lithography. Currently, the main forms of maskless lithography are laser and electron beam lithography.

2.4.1 Mask and Maskless Lithography

The photolithography, the representative of the mask lithography, is the process of forming a pattern in a layer of energy-definable photoresist. Photoresists are typically made from polymers that are sensitive to ultraviolet. For mask lithography, some area of the photoresist layer is covered by a hard mask during the exposure process. The covered photoresist can survive from the later developing process while the uncovered part will be removed to form the desired patterns. The patterned photoresist layer can be later used for physical etching or lift-off deposition. The drawback of the mask lithography is its inflexibility in changing the pattern designs.

That means one should always fabricate a new hard mask if pattern design needs to be changed.

On the contrary, the maskless lithography [14,15] directly transfers the pattern information onto the substrate without utilizing any intermediate hard mask. Instead of using hard mask, one needs to generate an electronically modifiable image that can be recognized by a direct writing system. This system can cast the image onto the photoresist by mean of direct writing technique as demonstrated in Figure 2.5(a). It extremely enhances the flexibility of pattern design when compared with hard mask lithography since one can easily modify the image of the pattern in a layout editor. In addition, the radiation is focused to a narrow beam that is scanned across the photoresist. With the help of high-precision step motor, the resolution of lithography can be enhanced to sub micrometer level.

To achieve a higher resolution, one might use electron beam lithography (EBL)[16-18] which writes pattern with sub-10nm resolution. In EBL, a highly focused beam of electrons scans on a material surface covered with an electron-sensitive photoresist according to a customized pattern design. Despite the high resolution of EBL, it also has some defects like secondary electron, back scattering and slower writing speed compared with other optical lithography. After the EBL writing, the exposed photoresist can be washed away in developing process as illustrated in Figure 2.5(b).

2.4.2 Ions Milling Etching and Lift-off Techniques

Etching is often used after the step of photoresist pattering. Traditionally it is the process of using strong acid to etch the unprotected parts of a metal surface to create a design, this is called wet etching. In modern manufacturing, different

chemical solvents have been used to properly etch the different materials. However, as heterostructures become more complicated and consist of many different materials, it is sometimes hard to find a suitable etching solution to etch away different materials with well-defined edge profile. In this case, ion Milling is often used. Ion milling is a physical etching technique that use the accelerated Ar ions to remove surface material substrate in high vacuum (10^{-5} Torr range). The principle is similar to sputtering in which Ar ions removes the target material. The etching depth can be well controlled by etching power and the processing time. However, the area covered by photoresist can be protected during the ion etching as shown in Figure 2.5(c). Since the continuous bombardment induced by Ar ions would heat up the targeted material, sample-under-etching must be cooled to protect sample structure.

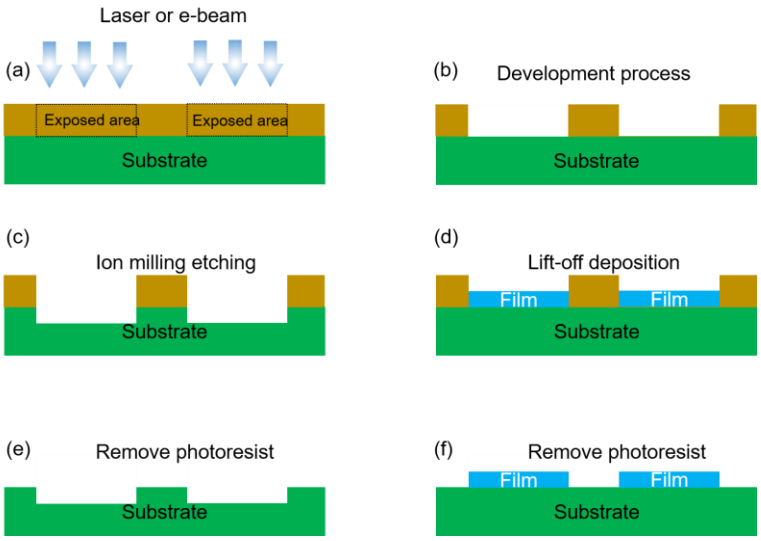

Figure 2.5 Demonstration of maskless lithography process. (a) Brown rectangle represents the layer of photoresist and arrows point the area to be exposed by laser or e-beam. (b) The exposed photoresist is etched by developer solution during development process. (c) Uncovered area is etched away by Ar ions while the covered parts remain. (d) Patterned photoresist forms slot where new material can be deposited into using sputtering or evaporation. (e) and (f) The sample after the process of ion milling and lift off, respectively.

Instead of subtracting the grown materials like etching down process, lift-off technique [19,20] is a method of depositing material on surface of a substrate covered by patterned photoresist. Typically, the thickness of the photoresist (several hundred nanometers) is much larger than the thickness of film to be deposited as shown in Figure 2.5(d). After the deposition, the film deposited on top of the photoresist will be removed together with the photoresist in a specific solvent. The scale of the minimal feature can be as small as nanometers if the photoresist is written by e-beam machine. lift-off method is an alternative way to patterning material when the etching method would induce undesirable effect to the layer underneath the target material. Lift-off is

very convenient in film deposition, but it also has some disadvantages. First, photoresist retention, this problem is often caused after the deposition that leads the photoresist could not be dissolved completely. The deposited material on top of the resist residue might lead failure of desired patterning. Secondly, sidewall attachment, during deposition especially for sputtering, the target material would be deposited on everywhere including the sidewall of the patterned photoresist. Those adhered material will be taken away together with photoresist in the last dissolving step. If the deposited film on the sidewall is connected to the film on the substrate, removing the sidewall film will also tears the edge of the material deposited on substrate, leading to a rough edge surface of the patterned device. However, this problem could be solved by creating undercut profile in a bilayer photoresist, which will be discussed later in Chapter 5.

2.5 Electrical Transport Measurement

Electrical measurement has been widely applied to study the transport properties of the carriers in conductors or semiconductors. It aims to investigate the response of the charge current induced electrical signal to the change of external stimuli such as electrical field, magnetic field, optical excitation, and temperature. In the field of spintronics, the transport of charges and spins are able to generate a variety of interesting phenomena such as giant magnetoresistance (GMR), tunnel magnetoresistance (TMR), Normal Hall effect (NHE), anomalous Hall effect (AHE), SHE, ISHE and spin magnetoresistance (SMR)[21-25] that all can be precisely characterized using electrical measurements. In this section, we will briefly introduce this important measurement in terms of the experiment setup, instrument control and its application in spintronics.

2.5.1 Instrumentation for Electrical Transport Measurement

Typically, there are two essential components in an electrical measurement: current source and voltmeter. Keithley 6221 AC and DC current source is often employed as a current source in our experiment for both regular DC static and high order harmonic electrical measurements. The 6221 model is a low current sourcing with very high sourcing accuracy of AC current output in the range of 4pA to 210mA. The 10MHz output update rate can generate smooth sine waves up to 100kHz, which makes it an ideal output source for lock-in applications such as measuring second and third harmonic device response. Moreover, the 6221 current source can work together with Keithley 2182A nanometer under the so called delta mode operation to extraordinarily eliminates the thermal contribution induced by the current flowing in device.

Another important instrument in electrical measurement is the lock-in amplifier which is a type of amplifier that can extract a signal at a known frequency (reference frequency) from a noisy environment. Lock-in amplifier itself can also output an AC voltage (5V, maximum) at a customized frequency which is self-locked as a reference frequency by detector. Then the analyzer can capture the signal contributed from this AC voltage. The amplifier also provides the reference-in option from external AC current or AC voltage source. To understand how a lock-in amplifier work, we assume the input signal is a sinusoidal wave $V_s\sin(\omega_s t+\theta_s)$ and lock-in amplifier has an internal reference $V_r\sin(\omega_r t+\theta_r)$ [26]. The phase sensitive detector has a mixer that multiply those two signals

$$\begin{aligned} V &= V_s V_r \sin(\omega_s t+\theta_s)\sin(\omega_r t+\theta_r) \\ &= \frac{1}{2}V_s V_r \cos[(\omega_s-\omega_r)t+(\theta_s-\theta_r)] - \frac{1}{2}V_s V_r \cos[(\omega_s+\omega_r)t+(\theta_s+\theta_r)] \end{aligned}. \quad (2.3)$$

The second term in Eq (2.3) is always zero after taking the average time integral whereas the first term is nonzero when $\omega_s = \omega_r$. Then one has

$$\bar{V} = \frac{1}{2} V_s V_r \cos(\theta_s - \theta_r) . \quad (2.4)$$

This is a measurable DC signal can be detected by lock-in amplifier. This voltage signal depends on both the signal amplitude and the phase difference.

In an electrical measurement, magnetic field is always employed to align the magnetic moment in magnetic materials. In general, a uniform small field can be generated using a pair of parallel Helmholtz coils while the large field can be produced by an electromagnet. Temperature is another important factor that may introduce many interesting phenomena in spintronic device. For instance, the temperature dependent magnetoresistance in magnetic material can indirectly reflects the change of spin scattering or the magnetization induced by changing the temperature. To assemble those factors in one unit, a powerful tool instrument named MPMS (Magnetic properties measurement system) has been developed to provide both large field (>10 T) and low temperature (2~330k) for electrical measurement.

2.5.2 Phenomenological Description of Electrical Voltages Induced by AMR, AHE and PHE

Since the orthogonal relation between the direction of the spin polarization, spin current and charge current directions, the spin related effects can induce charge accumulation forming voltage along both longitudinal and transverse direction in an electrical measurement. In a magnetic material, anisotropic magnetoresistance (AMR) effect [27] induce a voltage along longitudinal direction while transverse voltage might originate from AHE [28]and planner Hall effect (PHE). Despite the physical origins, they all can be phenomenologically expressed in form of resistances [29]

$$R_{xx} = R_0 + \frac{1}{2}\Delta R_{AMR}\sin^2\theta\cos^2\varphi \tag{2.5}$$

$$R_{xy} = \frac{1}{2}\Delta R_A\cos\theta + \frac{1}{2}\Delta R_P\sin^2\theta\sin 2\varphi \,, \tag{2.6}$$

where ΔR_{AMR}, ΔR_A and ΔR_P are the change in resistance due to the AMR, AHE and PHE, respectively. Suppose the charge current flows along *x* direction, the θ and φ are the polar and azimuth angles of the magnetization with respect to *z* and *x* direction, respectively. The Eqs (2.5) and (2.6) indicate that AMR contributed longitudinal signal is proportional to the projection of magnetization along the charge current direction while the transverse signal comes from two contributions including the AHE proportional to the out of plane magnetization m_z and PHE scaled with the product of the in plane component of magnetization, i.e., $m_x m_y$.

2.6 MOKE Measurement

2.6.1 Polar and Quadratic MOKE Measurements

We have introduced the basic principle of MOKE in Section 1.4.5 where we mainly derived the expression for polar and quadratic MOKE. In this section, we will discuss the setup of a MOKE measurement as shown in Figure 2.6. A polarizer in front of the laser source has been employed to purify the polarization of the laser beam. Since MOKE measures the reflected laser beam (green dash line) from the sample surface, a pellicle beam splitter (BS) is placed in front of the sample to separate the reflected light from a normal incident light (green solid line). There is another BS placed in front of the balanced detector (BBP, Nirvana 2007) to decompose the reflected beam into fast (green solid line) and slow axes (yellow dash line) separately. Thus, two beams are injected into the two channels of balanced

detector which detects the signal amplitude in each channel and outputs their amplitudes difference in voltage.

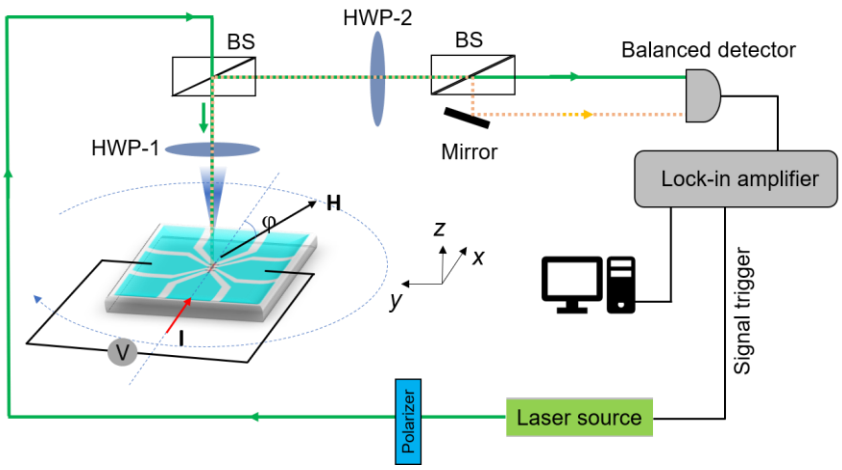

Figure 2.6 A schematics of our polar MOKE system. The laser source is a Ti:sapphire laser with wave length of 780 nm. The laser beam is focused on the center of a Hall bar structure made of magnetic material. A lock in amplifier is applied to sync the modulation frequency of the laser beam.

Wave plate is an optical device which alters the polarization of a light travelling through it. Waveplate is made from a birefringent material (such as quartz), for which the index of refraction is different for light polarized along the crystal axes (principal axes). It is known that the polarization of a light is determined by the phase difference between *s* and *p* components. The phase of each component can be shifted by letting the light passing a waveplate since *s* and *p* components have different velocities when they are traveling inside the waveplate. The phase shift can be expressed by

$$\Delta\phi = \frac{2\pi\Delta nL}{\lambda_0}, \tag{2.7}$$

where L is thickness of the waveplate along the traveling direction, λ_0 is the wavelength of light and n is the index of refraction [30]. There are two common types of waveplates: half wave plate (HWP, $\Delta\phi = \pi$) and quarter wave plate (QWP, $\Delta\phi = \pi/2$). For example, when a linearly polarized light wave passes through HWP, its polarization angle (with respect to a principal axis) is doubled because a 180 degrees phase is added to the component along the perpendicular principal axis as shown in Figure 2.7(a). And the linearly polarized light becomes circularly polarized light after passing through a QWP because a 90-degree phase shift is added as illustrated in Figure 2.7(b).

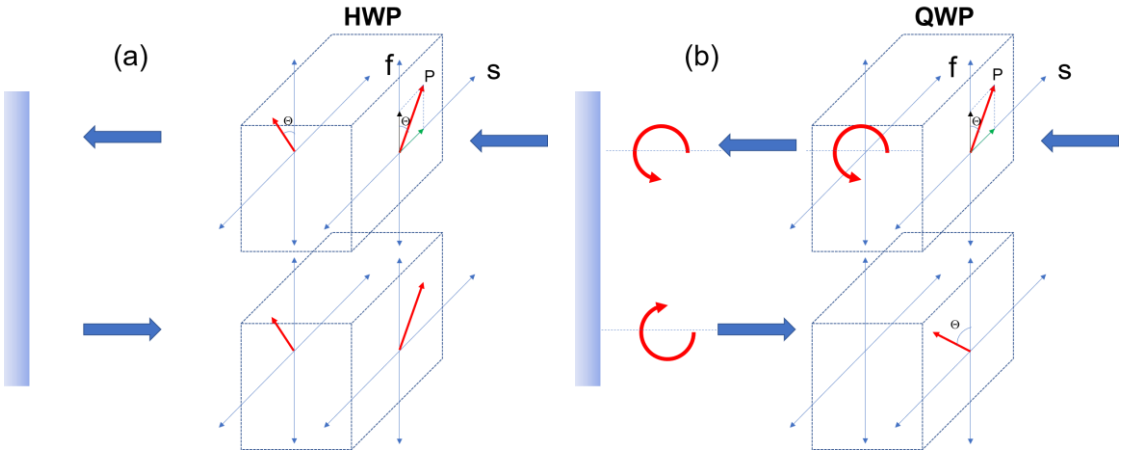

Figure 2.7 Change of polarization of laser beam passing through (a) HWP and (b) QWP twice after the reflection on a mirror. The incident light is initially polarized at an angle Θ with respect to fast axis.

In Figure 2.6, the laser beam passes the HWP-1 twice because of the reflection from the sample surface. In a MOKE setup with normal incidence, it is important to demonstrate how the polarization change after the reflected light passes through the

same wave plate again from the opposite side. At first, we suppose the incident light is a linearly polarized light wave,

$$\mathbf{E}_{(x,t)} = (E_f \hat{f} + E_s \hat{s}) e^{i(kz-\omega t)}, \tag{2.8}$$

where E_f and E_s are the amplitudes of the light in fast and slow axes, respectively. When the reflection occurs at the surface of a mirror, as shown in Figure 2.7(a) and (b), the polarization of the linearly polarized light does not change its polarization while the circularly polarized light gets an additional 180-degree phase thereby its chirality reverses after a mirror reflection. As a summary of polarization change shown in Figure 2.7(a) and (b), Table 2.1 gives the expression of the light wave at each pass. It shows that the reflected light is still linearly polarized after passing through either HWP or QWP twice. However, HWP does not change the polarization of the light while the QWP rotates the polarization to a symmetric position with respect to the fast axis direction. In real experiment, the misalignment of optical lens might lead to extra phase contribution to the light polarization. In addition, if the mirror is replaced with the real magnetic material, an additional phase shift is induced after the light gets reflected from sample surface due to MOKE. The MOKE measurement system is capable of detecting this magneto-optical interaction induced signal though it is tiny.

Table 2.1 A summary of light change at each pass of a wave plate. In this table the time and space dependent term $e^{i(kz-\omega t)}$ has been omitted for convenience.

Wave plate	Phase shift	First pass	Reflection by mirror	Second pass
Arbitrary	ϕ	$(E_f \hat{f} + E_s e^{i\phi} \hat{s})$	$(-E_f \hat{f} - E_s e^{i\phi} \hat{s})$	$(-E_f \hat{f} - E_s e^{i2\phi} \hat{s})$
HWP	π	$(E_f \hat{f} - E_s \hat{s})$	$(-E_f \hat{f} + E_s \hat{s})$	$(-E_f \hat{f} - E_s \hat{s})$

QWP	$\pi/2$	$(E_f \hat{f} + iE_s \hat{s})$	$(-E_f \hat{f} - iE_s \hat{s})$	$(-E_f \hat{f} + E_s \hat{s})$

It is noted that the HWP-2 in Figure 2.6 is used to balance the phase difference between the two lights being directed into the balanced detector. Zeroing the phase difference is often applied at the very beginning of a MOKE measurement to remove the offset due to the imbalance between two channels.

2.6.2 Time-resolved MOKE Measurement

The time-resolved (TR) MOKE system is designed to measure the magnetization dynamics driven by magnetic field pulses or current-induced SOTs. A pump pulse with a given polarization is used to prepare a spin population in a material of interest. The delay time of a probe pulse to pump pulse is then scanned to gather the MOKE signal which can be used to study the magnetization dynamics. In our system we synced the electrical pump pulse and optical probe pulse sequences, which allow us to use the laser to detect magnetization change induced by the electrical pulse. The diagram of our TR-MOKE system is displayed in Figure 2.8 (a). The synchronization diagram is shown is Figure 2.8 (b). The current pulses are synchronized to laser pulses. The laser source (Coherent Mira Ti:Sapphire, 150 *fs* fwhm, 76 MHz, center wavelength 780 nm) sends out laser pulses signal to an 81134A pulse pattern generator as an external reference to trigger the current pulses.

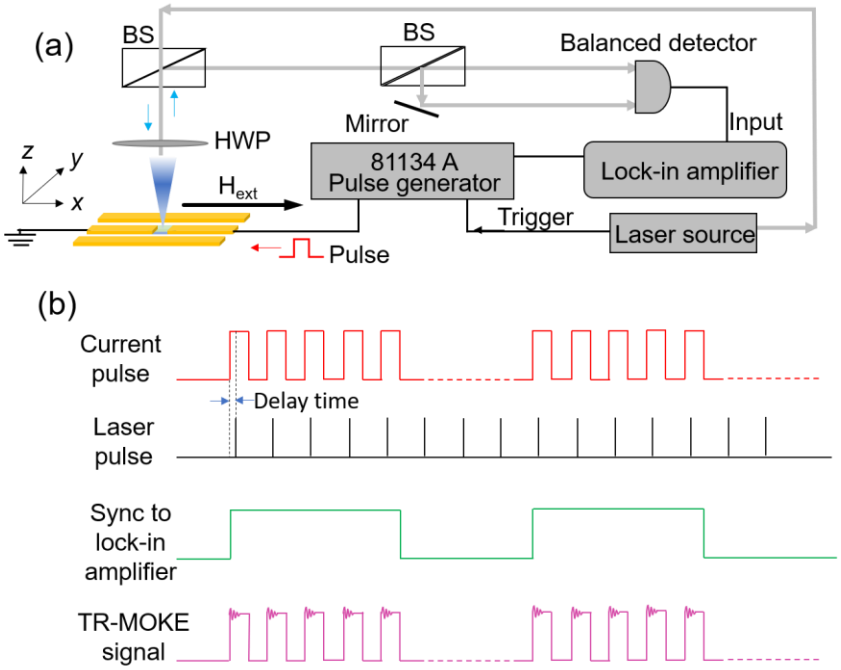

Figure 2.8 (a) The experimental setup of the TR-MOKE system. (b) Synchronization diagram for the electrical pulse and optical pulse trains.

Laser pulse width (femtoseconds) is much narrower than the width of the current pulse (ps~ns). Therefore, by scanning the delay time within a current pulse width, the laser can pick up the current pulse induced signal at each scanned time point. In our experiment, we keep the phase of probe laser pulse fixed and scan the onset of the current pulse relative to the laser pulse by controlling the delay time. Overall, TR-MOKE result displays the measured MOKE signal as a function of delay time. To enhance the signal to noise rate, we modulate the current pulses by sending the generator a digital signal (low frequency at 9.233 kHz, green square wave) from the Lock-in amplifier. In the modulated current pulses signal (red wave), each cycle contains 4096 pulses followed by 4096 zero pulses. Finally, taking the average of 4096 pulses induced MOKE signal dramatically reduces the background noises.

Since the electrical pump signal is at ps to ns level, the magnetic sample must be integrated into the signal line of a CPW to match the impedance. To design a sample with 50 Ω impedance, one needs to carefully characterize the sample's resistivity especially for multilayer samples. In addition, since the maximum output of 81134A pulse generator is only 2 V, one has to design the sample so that high enough current density can flow through the sample to generate observable SOT phenomena.

2.7 Micromagnetic Simulation

In Section 1.2, we introduced the macromagnetic formalism of the magnetization dynamics that was calculated by solving the nonlinear ordinary differential LLG equation under small precession angle approximation. That is a macrospin model and is applicable to infinitely large bulk magnetic materials or two dimensional magnetic thin films. However, in confined magnetic structures (except perfect ellipsoid) like nanostripes, nanoparticles and naowires, the macrospin model is no longer valid since the distribution of the magnetic moment is nonuniform due to the demagnetizing effect. Researchers have developed discrete spin models (Ising or Hisenberg theroy) which involves the nonuniformity factor in the calculation of a nanostructure, but it was limited by the computational ability if the size of magnetic structure is in micron or sub-micron level. Later, the micromagnetic continuum theory was developed to fill this gap. In micromagnetic simulations, the sample is divided into a great number of cells and each cell is treated as a single spin. The dynamics of the spins in the cells are then numerically calculated by integrating LLG equation over time. Two most popular micromagnetic simulator are OOMMF (Object Oriented Micromagnetic Framework) and Mumaxs3.

2.7.1 OOMMF

OOMMF software [31] was developed at the National Institute of Standards and Technology, Gaithersburg, MD by Mike Donahue and Don Porter in 1999. The script code is written in a "*mif*" file where the most of magnetic parameters like the saturation magnetization, exchange stiffness constant, magneto crystalline anisotropy, demagnetizing effect, and the external magnetic field can be defined. Here we list several often-used parameters:

- **Ms:** Saturation magnetization in unit of A/m.
- **A:** Exchange stiffness in unit of J/m.
- **H:** Magnetic field in unit of mT.
- **K1:** Crystalline anisotropy constant in unit of J/m^3. uniaxial|cubic.

  $K1 > 0$, the anisotropy axis is an easy axis.

  $K1 < 0$, the anisotropy axis is a hard axis.
- **γ :** The Landau-Lifshitz gyromagnetic ratio, in unit of m/(A.s). Default value is 2.21×10^5 if no defined.
- **α:** Damping coefficient in the range 0.004 to 0.15.

The structure of the program code is composed by statements and several Specify blocks. One need to announce the *mif* file version at the very beginning of the script. The variables used in the script should be defined using the "Parameter" or "Set" commands. OOMMF provides variety of extensions for different purposes like the definition of atlases, meshes, energies, evolver, and drivers. User can use those extensions in the script by calling them in a Specify block. It is noted that the user could define many types of effective fields using the energy extension like the external magnetic field, anisotropic field, demagnetizing field and so on.

There are two types of evolvers in OOMMF: time evolver and minimization evolver. When the simulation is started, the evolvers update the magnetization configuration step by step. The time evolver tracks LLG dynamics while the minimization evolver locates the local minima in the energy surface according to the energy minimization principle. Evolvers are controlled by the compatible drivers. For example, the time evolvers must be called by time drivers whereas the minimization evolvers must be paired with minimization drivers. In each iteration, the driver feeds back the magnetization configuration to the evolver to refresh the configuration and advance to the next operation order. In another word, evolvers are responsible for moving the simulation forward in individual steps while drivers coordinate the action of the evolver on the simulation as a whole by grouping steps into tasks and determine when a simulation stage or run is complete.

There are three time-evolvers and one minimization evolver in the standard OOMMF distribution. The time evolver includes Oxs EulerEvolve, Oxs RungeKuttaEvolve, and Oxs SpinXferEvolve. The minimization evolver has only Oxs CGEvolve. The EulerEvolve implements a simple first order Euler method to advance the LLG equation. The KuttaEvolve implements several Runge-Kutta methods for integrating the LLG with step size control. The SpinXferEvolve integrates a regular LLG equation with spin momentum terms including damping-like and field-like torque terms. It is a very useful simulation evolver that can model current induced phenomena related with spin transfer torque or spin orbit torques. It is noted that the Oersted field arising from the current is not included in this evolve. Lastly, the CGEvolve evolver is an in-development conjugate gradient minimizer without the preconditioning.

2.7.2 MuMax3

Mumax3 [32], written in Go language, is an open-source GPU-accelerated micromagnetic simulation program developed at the DyNaMat group of Prof. Van Waeyenberge at Ghent University. Mumax3 can solve the time and space dependent magnetization evolution in a magnetic material using a finite difference discretization. Mumax3 provides a few Runge-Kutta methods to advance the LLG equation. The Mumax3 provides many features for micromagnetic simulation such as Magnetostatic field, Heisenberg exchange, region exchange like RKKY coupling, Dzyaloshinskii-Moriya interaction (DMI), Spin-transfer torque, uniaxial magnetocrystalline anisotropy, thermal fluctuations, complex field, and current excitation. In addition, Mumax3 is able to remove the edge charges to simulate an infinitely large sample. As to the simulation speed, GPU-accelerated Mumax3 is of 1~2 orders faster than that of the CPU-based micromagnetic simulations like OOMMF.

REFERENCES

[1] D. M. Mattox, *Handbook of physical vapor deposition (PVD) processing* (William Andrew, 2010).

[2] D. M. Mattox,"*Physical vapor deposition (PVD) processes*", Metal Finishing **100**, 394 (2002).

[3] J. E. Greene,"*Tracing the recorded history of thin-film sputter deposition: From the 1800s to 2017*", Journal of Vacuum Science & Technology A: Vacuum, Surfaces, and Films **35**, 05C204 (2017).

[4] P. J. Kelly and R. D. Arnell,"*Magnetron sputtering: a review of recent developments and applications*", Vacuum **56**, 159 (2000).

[5] M. Cardona and Y. Y. Peter, *Fundamentals of semiconductors* (Springer, 2005).

[6] S. Swann,"*Magnetron sputtering*", Physics in technology **19**, 67 (1988).

[7] J. E. Mahan,"*Physical vapor deposition of thin films*", Physical Vapor Deposition of Thin Films, by John E. Mahan, pp. 336. ISBN 0-471-33001-9. Wiley-VCH, January 2000., 336 (2000).

[8] M. Paranthaman *et al.*,"*Growth of biaxially textured buffer layers on rolled-Ni substrates by electron beam evaporation*", Physica C: Superconductivity **275**, 266 (1997).

[9] H. R. Fallah, M. Ghasemi, A. Hassanzadeh, and H. Steki,"*The effect of annealing on structural, electrical and optical properties of nanostructured ITO films prepared by e-beam evaporation*", Materials Research Bulletin **42**, 487 (2007).

[10] S. Foner,"*Versatile and sensitive vibrating - sample magnetometer*", Review of Scientific Instruments **30**, 548 (1959).

[11] C. Line,"*Microstrip, Stripline, and CPW Design*".

[12] Y. Chen, X. Fan, Y. Zhou, Y. Xie, J. Wu, T. Wang, S. T. Chui, and J. Q. Xiao,"*Designing and tuning magnetic resonance with exchange interaction*", Advanced Materials **27**, 1351 (2015).

[13] M. Farle,"*Ferromagnetic resonance of ultrathin metallic layers*", Reports on progress in physics **61**, 755 (1998).

[14] W. C. Sweatt and R. H. Stulen, (Google Patents, 1999).

[15] K. C. Johnson, (Google Patents, 2001).

[16] C. Vieu, F. Carcenac, A. Pepin, Y. Chen, M. Mejias, A. Lebib, L. Manin-Ferlazzo, L. Couraud, and H. Launois,"*Electron beam lithography: resolution limits and applications*", Applied surface science **164**, 111 (2000).

[17] A. A. Tseng, K. Chen, C. D. Chen, and K. J. Ma,"*Electron beam lithography in nanoscale fabrication: recent development*", IEEE Transactions on electronics packaging manufacturing **26**, 141 (2003).

[18] M. A. McCord and M. J. Rooks,"*Electron beam lithography*", Handbook of microlithography, micromachining, and microfabrication **1**, 139 (1997).

[19] G. Dolan,"*Offset masks for lift - off photoprocessing*", Applied Physics Letters **31**, 337 (1977).

[20] E. C. Fredericks and H. N. Kotecha, (Google Patents, 1986).

[21] Y.-T. Chen, S. Takahashi, H. Nakayama, M. Althammer, S. T. Goennenwein, E. Saitoh, and G. E. Bauer,"*Theory of spin Hall magnetoresistance*", Physical Review B **87**, 144411 (2013).

[22] Z. Xiong, D. Wu, Z. V. Vardeny, and J. Shi,"*Giant magnetoresistance in organic spin-valves*", Nature **427**, 821 (2004).

[23] H. Nakayama *et al.*,"*Spin Hall magnetoresistance induced by a nonequilibrium proximity effect*", Physical review letters **110**, 206601 (2013).

[24] J. Fischer, M. Althammer, N. Vlietstra, H. Huebl, S. T. Goennenwein, R. Gross, S. Geprägs, and M. Opel,"*Large Spin Hall Magnetoresistance in Antiferromagnetic α− Fe 2 O 3/Pt Heterostructures*", Physical Review Applied **13**, 014019 (2020).

[25] B. G. Park *et al.*,"*A spin-valve-like magnetoresistance of an antiferromagnet-based tunnel junction*", Nature materials **10**, 347 (2011).

[26] J. H. Scofield,"*Frequency‐domain description of a lock‐in amplifier*", American journal of physics **62**, 129 (1994).

[27] T. McGuire and R. Potter,"*Anisotropic magnetoresistance in ferromagnetic 3d alloys*", IEEE Transactions on Magnetics **11**, 1018 (1975).

[28] N. Nagaosa, J. Sinova, S. Onoda, A. H. MacDonald, and N. P. Ong,"*Anomalous hall effect*", Reviews of modern physics **82**, 1539 (2010).

[29] M. Hayashi, J. Kim, M. Yamanouchi, and H. Ohno,"*Quantitative characterization of the spin-orbit torque using harmonic Hall voltage measurements*", Physical Review B **89**, 144425 (2014).

[30] A. Asundi, L. Tong, and C. G. Boay,"*Phase-shifting method with a normal polariscope*", Applied optics **38**, 5931 (1999).

[31] M. J. Donahue and M. Donahue, *OOMMF user's guide, version 1.0* (US Department of Commerce, National Institute of Standards and Technology, 1999).

[32] A. Vansteenkiste, J. Leliaert, M. Dvornik, M. Helsen, F. Garcia-Sanchez, and B. Van Waeyenberge,"*The design and verification of MuMax3*", AIP advances **4**, 107133 (2014).

Chapter 3

ENHANCED FMR FREQUENCY AND INTENSITY IN MAGNETIC TRILAYERS

3.1 Motivation

FMR has been widely used to characterize the magnetic properties of magnetic materials at high frequency. We have introduced the FMR in Section 1.2 by deriving the dispersion relation especially in the case of an in-plane magnetized ferromagnetic film as in Eq (1.10). The FMR measurement has also been introduced in Section 2.3.

In general, the FMR of the material is studied in regard to its resonant frequency and magnitude. For example, as demanded by the modern storage technique, the magnetic storage devices need to operate at a higher and higher speed for fast switching which requires the increase on resonant frequency of magnetic materials. According to the Eq (1.10), the resonant frequency can be increased by applying high magnetic field or using magnetic materials with high saturation magnetization. However, the former approach is impractical in real applications while the latter approach is limited since it is very difficult to develop new materials with higher saturation magnetization. On the other hand, In the magnetic radar absorbing material, the high absorption in a large scale of resonant frequency is demanded, which means the increase on resonant magnitude.

Enhancing the FMR frequency via increasing the effective anisotropic field has attracted much attention from researchers. The manipulation of the magnetic anisotropy, as reported, can be achieved by using multiferroic materials [1],

magnetoelastic effect [2], and electric field control [3]. Recently, tuning the FMR via exchange coupling has attracted great attention since exchange coupling can be significantly larger than the anisotropy and thus allow a wide range of tuning [4-7]. For example, in a typical ferromagnetic material (FM), the effective field of the exchange coupling could be as high as 10^4 kOe, equivalent to about 28 THz [8]. While it is difficult to tune the exchange coupling inside a FM, it is easy to tune the exchange coupling at the interface between two FM layers, leading to a large tuning of FMR. The concept should be distinguished from the exchange coupling between FM and antiferromagnetic layer (AFM), which is much weaker than the exchange coupling at the FM/FM interface.

The exchange coupled FM bilayers exhibits two resonant modes: 1) acoustic mode (AM) in which the moments in two FM layers precess in phase and 2) optical mode (OM)in which the moments in two FM layers precess out-of-phase [9,10]. The resonance frequency of OM is generally higher than that of AM due to the induced effective field by exchange coupling at the interface between two FM layers. In addition, by varying the EC strength, one can also turn the energy exchange between two layers, as a result, change the FMR magnitude.

In addition, the resonance frequency of OM is very sensitive to the interface exchange coupling just like two coupled harmonic oscillators. This situation should also be distinguished from commonly discussed oscillatory coupling between two FM layers separated by a spacer layer such as Cu, Cr, and Ru [5,6,11,12], which is mediated via Ruderman–Kittel–Kasuya–Yosida (RKKY) interaction [13-18]. In this work we theoretically and experimentally demonstrate that, with coupled FM bilayer, one can (1) significantly enhance the resonance frequency using OM, (2) enhance the

intensity of the OM by increasing the contrast in the saturation magnetization of two constituent FM layers, and (3) increase the intensity of OM with increasing applied magnetic field or frequency. While the feature (1) is very useful to enhance the operating frequency of a spintronic device, feature (2) and (3) could be very useful for microwave absorption applications.

The study of exchange coupling has been widely reported in coupled system with a FM/NM/FM structure where the top and bottom ferromagnets are the same materials separated by a normal metal. However, the study on coupled system with different ferromagnets has been rarely reported. The influence of magnetization anti-symmetry on the FMR modes in coupled system also becomes interesting. In this work, we selected two common ferromagnets, $Co_{90}Fe_{10}$ and $Ni_{80}Fe_{20}$ (Py, permalloy), to construct the coupled magnetic bilayers where the magnetization in each layer is in plane but with different magnitudes. As a single layer, those two soft ferromagnets are well known magnetic materials and have been well studied in regard of both static and dynamic properties. To increase the contrast in magnetization, we dope the Cu element into Py during the film fabrication using co-sputtering method, which decreases the magnetization in Py layer.

3.1.1 Modeling FMR in Coupled Ferromagnetic Bilayer

At first, we build a model to simulate the magnetization dynamics in a coupled bilayer system starting from the LLG equation. One can write down the modified LLG equation for each layer in a coupled bilayer by introducing an effective field due to the exchange coupling between two FM layers. In a linear regime, the equation is written as

$$\frac{d\mathbf{M}_\rho}{dt} = -|\gamma|\mathbf{M}_\rho \times \mu_0 \mathbf{H}_{\mathbf{eff}\rho} + \frac{\alpha_\rho}{M_{\rho s}}(\mathbf{M}_\rho \times \frac{d\mathbf{M}_\rho}{dt}), \tag{3.1}$$

where ρ is the index of FM layer, γ is the gyromagnetic ratio, μ_0 is the permeability of the vacuum, α is the Gilbert damping factor, H_{eff} is the total effective field and $M_{\rho s}$ is the saturation magnetization of the layer ρ.

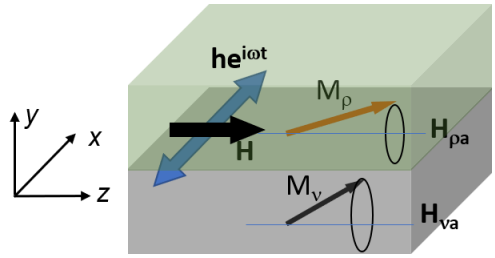

Figure 3.1 The magnetization in coupled ferromagnetic layers labeled by $M_{\rho s}$ and $M_{\nu s}$. External magnetic field is applied in z direction whereas a microwave induced in plane rf magnetic field is in x direction.

With the structure and field orientation shown in Figure 3.1, the time-dependent magnetization and the total effective field are given in Eqs. (3.2) and (3.3), respectively:

$$\mathbf{M}_\rho = \mathbf{M}_\rho(t) = (m_{\rho x}e^{i\omega t}, m_{\rho y}e^{i\omega t}, M_{\rho s}), \tag{3.2}$$

$$\mathbf{H}_{\mathbf{eff}\rho} = (he^{i\omega t}, -m_{\rho y}e^{i\omega t}, H + H_{\rho\alpha}) + A_{\rho\nu}\mathbf{M}_\nu, \tag{3.3}$$

where ρ, ν = 1, 2 are the indexes of the two FM layers. $m_{\rho x}$ and $m_{\rho y}$ are the x and y components of the dynamic magnetization in layer ρ, respectively, $\omega = 2\pi f$ is the microwave frequency. The z component of the magnetization is approximated to be the saturation magnetization because the precessing angle is very small in linear regime (no switching). The total effective field in the layer ρ is consisting of the *rf* magnetic field $he^{i\omega t}$ in x direction, the effective demagnetizing field $H_d = m_y e^{i\omega t}$ in y

direction, the external magnetic field H and the effective anisotropic field H_a in z direction[19]. Here we neglect the dipolar field since the measured films have large lateral dimensions over the thickness. The exchange coupling effect induced effective field is written in the form of

$$\mathbf{H}_{EC(\nu\to\rho)} = A_{\rho\nu}\mathbf{M}_{\nu}, \tag{3.4}$$

where $A_{\rho\nu}$, differing from the exchange stiffness in unit, is used to represent the exchange coupling strength exerted on the layer ρ by the layer ν. Knowing that the exchange coupling (EC) energy between two FM layers is defined as [20]

$$E_{EC} = -J\frac{\mathbf{M}_{\rho}\cdot\mathbf{M}_{\nu}}{M_{\rho s}M_{\nu s}}, \tag{3.5}$$

where J is the exchange coupling coefficient. With Eq. (3.5) the IEC induced effective field can also be given in the form of

$$\mathbf{H}_{EC(\nu\to\rho)} = \frac{J}{t_{\rho}M_{\rho s}M_{\nu s}}\mathbf{M}_{\nu}, \tag{3.6}$$

where t_ρ is the thickness of the layer ρ. By comparing Eq. (3.4) and (3.6), it is concluded that $A_{12} = A_{21}$ holds in the bilayer when $t_1 = t_2$, which would further simply the model for coupled bilayer composed of different ferromagnetic materials.

According to Eq. (3.1)–(3.3), we can combine and write the coupled LLG equations of the two FM layers into matrix equation. Finally the susceptibility tensor χ [21] of the coupled system can be obtained as (See Appendix A for the detailed derivation)

$$\boldsymbol{\chi} = \begin{bmatrix} \chi_{1x,1x} & 0 & \chi_{1x,2x} & 0 \\ \chi_{1y,1x} & 0 & \chi_{1y,2x} & 0 \\ \chi_{2x,1x} & 0 & \chi_{2x,2x} & 0 \\ \chi_{2y,1x} & 0 & \chi_{2y,2x} & 0 \end{bmatrix}, \tag{3.7}$$

where element $\chi_{\rho i,vj}$ ($i, j = x, y$) denotes the response of the i component of magnetization in the layer ρ to the j component of rf field in the layer v. To be consistent with our experimental configuration, we only take into account the rf magnetic field in x direction. For film samples, the $\chi_{\rho x}$ could be significantly larger than $\chi_{\rho y}$ due to the demagnetizing effect. Therefore, we take the sum of the x component in χ as effective susceptibility $\chi=\chi_{1x,1x}+\chi_{1x,2x}+\chi_{2x,1x}+\chi_{2x,2x}$. In our simulation, we calculate the imaginary part of the complex number susceptibility Im(χ), which corresponds to the experimentally measured absorption part of FMR.

3.1.2 Numerical Simulation in Coupled CoFe/NiFe System

We first extract the needed parameters for our simulation like the saturation magnetization, effective anisotropic field, and damping factor of single CoFe and NiFe layers via FMR measurements. The FMR measurement setup has been introduced in the Section 2.3 and the sample configuration is displayed in Figure 3.2 (a). We measured FMR of single CoFe(10) and NiFe(10) layers (the numbers in parentheses are thicknesses in nanometers). By fitting the FMR peak as a function of the applied field and the FMR linewidth as a function of frequency, we can determine $\mu_0 M_{s\_CoFe}$= 1.63 T, $\mu_0 M_{s\_NiFe}$= 0.94 T, $\mu_0 H_{a\_CoFe}$= 2.4 mT, $\mu_0 H_{a\_NiFe}$= 6.5 mT, $\alpha_{\_CoFe}$= 0.016, $\alpha_{\_NiFe}$= 0.009. Both films have very weak anisotropies, and the external magnetic field can easily align the magnetization parallelly in the same direction in bilayer samples.

In Figure 3.2 (b), we show the measured FMR curves of CoFe(10nm, black square), NiFe(10 nm, red circle) and CoFe(10)/Ta(0.5)/NiFe(10) (blue triangle) samples at a microwave frequency of 13 GHz. The FMR peak of NiFe appears at a higher field than that of CoFe since NiFe has a relatively lower magnetization, which can be easily understood from the Kittel equation in Eq (1.10) that small

magnetization requires a larger magnetic field to excite FMR at a fixed frequency. Two peaks are observed in CoFe/Ta/NiFe sample due to the exchange coupling between CoFe and NiFe. The peak at high field is the AM mode while the one at low field is the OM mode. It is obvious that the magnitude of OM is much smaller than that of AM mode since the magnetization in two layers are precessing out-of-phase. Here, a 0.5nm Ta spacer is inserted between two ferromagnets to decrease the coupling so the OM can be observed clearly.

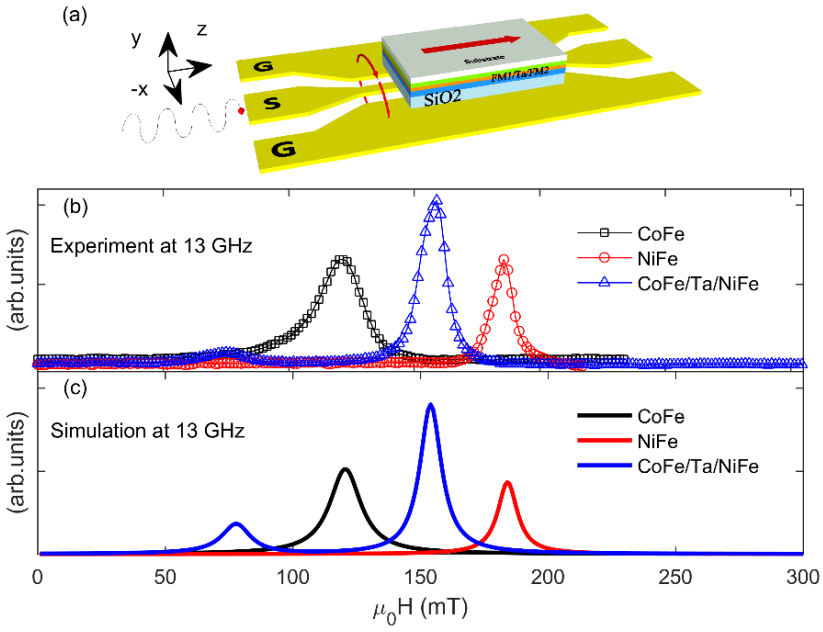

Figure 3.2 (a) The schematics of sample on a CPW in FMR measurement. Microwave is injected into signal line (S) which induces an ac magnetic field along *x-y* plane. The red arrow indicates the direction of the applied magnetic field and anisotropy field. The field scan of (b) experimental and (c) simulated FMR curves of $Co_{90}Fe_{10}$(10), $Ni_{80}Fe_{20}$(10) and CoFe(10)/Ta(0.5)/NiFe(10) tribilayer structure. The frequency of the microwave is fixed at 13 GHz.

As shown in Figure 3.2 (b) and (c), our simulation results match the experimental results very well in both position and magnitude. In this simulation the exchange strength is set $A_{12} = 0.027$. This experiment validates our model, which can thus be to further understand the properties of the bilayer and optimize the properties. For example, OM occurs at high frequency but with a very small magnitude. If we want to design microwave absorbing materials, we would like to enhance the magnitude.

We simulate the frequency dependence of the two modes on the external dc field in $Co_{90}Fe_{10}(10)/Ni_{80}Fe_{20}(10)$ bilayer with $A_{12} = 0$ (Figure 3.3(a)) and $A_{12} = 0.025$ (Figure 3.3(b)). The dark areas in the color map show the position of FMR peaks with their intensities illustrated by the side bar. When there is no coupling between two layers, i.e $A_{12} = 0$, two resonances correspond FMR of $Co_{90}Fe_{10}(10)$ and $Ni_{80}Fe_{20}(10)$ layers, respectively. The FMR intensity for CoFe layer is stronger because of its higher saturation magnetization. On the other end, the FMR peak for NiFe has a narrower width in frequency, indicating the damping constant is smaller, i.e. $\alpha_{NiFe} < \alpha_{CoFe}$. The exchange coupling between two layers lead to the appearance of the OM and AM, in which OM has much higher resonant frequency compared to that of CoFe layer whereas the resonance frequency of AM is only slightly higher than that of NiFe layer. In addition, unlike the decoupled layers, there is a clear separation between OM and AM, especially in low field region. Specifically, OM frequency is about 6 GHz above the AM frequency at $H = 0$. This manifests the net enhancement of resonant frequency induced by the effective field induced by exchange coupling.

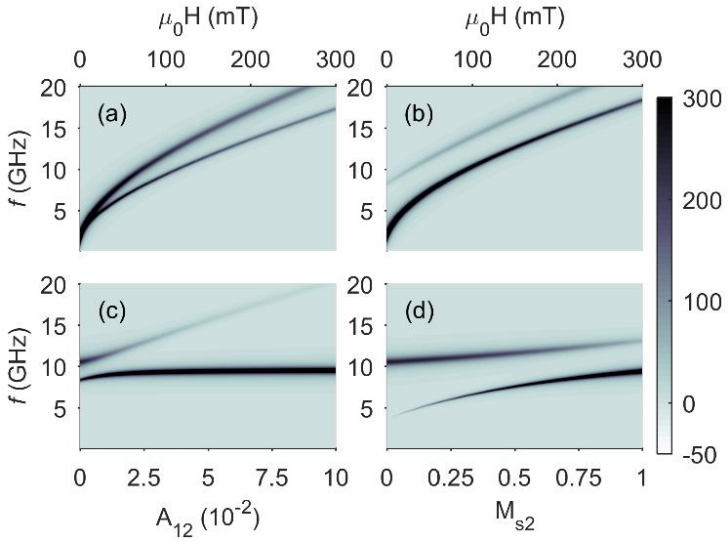

Figure 3.3 The imaginary part of calculated susceptibility as a function of the frequency and magnetic field for CoFe/NiFe bilayer with the exchange strength of (a) A_{12} = 0 and (b) A_{12} = 0.025. The dark areas formed in the color maps represent the two FMR modes. The upper/lower branches correspond to OM/AM, respectively, with value represented by the side bar except the case with A_{12} = 0. (c) The two modes as a function of the frequency and A_{12} at a fixed magnetic field of 80 mT. (d) The two modes as function of frequency and M_{s2} at fixed A_{12} = 0.025 and $\mu_0 H$ = 80 mT.

The OM and AM as a function of the exchange coupling strength at a fixed field of 80 mT is shown in Figure 3.3(c). As expected, OM is more sensitive to the exchange coupling strength whereas AM is only weakly depending on the exchange strength. It is noted that here we only consider the bilinear coupling in our simulation. As A_{12} increases, the OM mode intensity decreases while the AM mode increases till saturation, which is in agreement with the calculated results in [22].

The intensity of AM for FeCo/NiFe bilayers is strong due to in-phase precession in two layers, whereas the intensity of OM is much weaker due to out-of-phase precession between two layers. OM is of more interesting for high frequency

applications. For spintronic applications based on giant magnetoresistance (GMR) in $FM_{pin}/NM/FM_{free}$ structure where subscripts represent pinned and free layers, respectively, FM_{free} layer can be replaced with coupled FM1/FM2 bilayers to take the advantage of the OM mode. In this case, GMR is only sensitive to interface layer, i.e. the magnetization precession angle in FM1 layer. Therefore, the weak OM intensity does not matter since the precession angle in each layer does not change much compared with precession angle of individual layer at their ferromagnetic resonance, as we have illustrated before in using this structure as microwave detector[5]. However, the intensity of OM certainly matters if absorption is needed in the applications. Therefore, we also investigate how one can improve the intensity of the OM. Due to the out-of-phase precession in OM, one clear solution is to reduce the magnetization of one of FM layers. Figure 3.3(d) shows the dependence of two resonance modes as a function of varying the magnetization (M_{s2}) in NiFe of CoFe/NiFe bilayer with A_{12}=0.025 and in $\mu_0 H$ = 80 mT magnetic field. Indeed, the intensity of OM (upper branch) significantly increases with decreasing M_{s2}. For AM branch, both frequency and intensity are decreasing with reducing M_{s2} due to the decrease in the total magnetization of the bilayer. (The simulation scripts have been listed in Appendix B which can be run on MATLAB platform)

3.2 Experiment Results

3.2.1 Tailor OM and AM Modes in $Co_{90}Fe_{10}(10)/Ta(t)/ (Ni_{80}Fe_{20})_{1-x}Cu_x(10)$ Samples

In our simulation, we study the dependence of FMR modes on the exchange coupling strength and the magnetization in NiFe layer. We next experimentally verify these simulations. For sample preparation, we insert a thin heavy metal Ta between

CoFe and NiFe layers for the purpose of manipulation of the interfacial exchange coupling by varying the Ta thickness. In addition, we also change the magnetization in NiFe layer by fabricating $(Ni_{80}Fe_{20})_{1-x}Cu_x$ alloy films. The magnetization change in NiFe layer can be achieved by doping Cu into NiFe while keep the thickness of the layer fixed. All samples were grown on Si substrates at room temperature under an Ar pressure of 4.5×10^{-3} Torr in a magnetron sputtering system that has a base pressure of 1.4×10^{-7} Torr. Control samples of single layer of $Co_{90}Fe_{10}(10)$, $Ni_{80}Fe_{20}(10)$, $Ni_{52}Fe_{13}Cu_{35}(10)$ and $Ni_{44}Fe_{11}Cu_{45}(10)$ were also fabricated. The last two ternary alloy films were grown by co-sputtering of $Ni_{80}Fe_{20}$ and Cu targets [23]. The thickness of the Cu doped samples is controlled by sputtering rate calculated from the deposition rate calibration. Composition ratio was controlled by varying the sputtering power on Cu target. Three different trilayer samples were fabricated with structure of $Co_{90}Fe_{10}(10)/Ta(t)/Ni_{80}Fe_{20}(10)$, $Co_{90}Fe_{10}(10)/Ta(t)/Ni_{52}Fe_{13}Cu_{35}(10)$ and $Co_{90}Fe_{10}(10)/Ta(t)/Ni_{44}Fe_{11}Cu_{45}(10)$ where the Ta layer was grown in wedge shape of variable thickness t from 0 to 1 nm by off center deposition. All the samples are capped with a 5 nm SiO_2 layer to prevent samples from oxidation. Samples with wedged Ta layer were cut equally into 11 pieces of rectangle sample (10 mm×2 mm) with spacer layer thicknesses changing from 0 to 1 nm. The anisotropic easy axes in the FM layers have been purposely induced along the long sides of the samples.

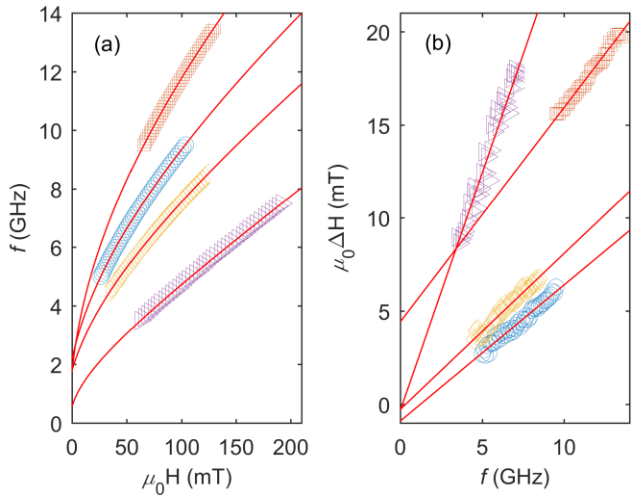

Figure 3.4 (a) The dispersion relation in individual magnetic layer: $Co_{90}Fe_{10}$ (squares), $Ni_{80}Fe_{20}$ (circles), $Ni_{52}Fe_{13}Cu_{35}$ (diamonds) and $Ni_{44}Fe_{11}Cu_{45}$ (triangles). They have the same thickness of 10 nm. (b) The linewidth of FMR peaks as a function of resonant frequencies.

We first conduct the FMR measurement on the control samples. The resonant frequency as a function of magnetic field (dispersion relation) is present in

Table 3.1 a summary of magnetic properties in single layer.

	$Co_{90}Fe_{10}$	$Ni_{80}Fe_{20}$	$Ni_{52}Fe_{13}Cu_{35}$	$Ni_{44}Fe_{11}Cu_{45}$
$\mu_0 Ms$ (T)	1.63	0.94	0.57	0.18
$\mu_0 Ha$ (mT)	2.4	6.5	7.1	2.3
α	0.016	0.009	0.012	0.035

Figure 3.4(a). The red curves are the fittings to the data using the Kittle equation, which gives result of the in plane effective magnetization and H_a. On the other hand, the dependence of the line width of the FMR peak on the resonant frequency f is shown in Figure 3.4(b). The linear relationship can be fitted using $\Delta H=\alpha(4\pi f/\gamma)$ and

the Gilbert damping can be determined from the slope of the fit line. All the extracted parameters from the data fitting in Figure 3.4 (a) and (b) are summarized in Table 3.1. It is found that with increasing the concentration of Cu, the magnetization in $(Ni_{80}Fe_{20})_{1-x}Cu_x$ alloy samples is decreasing while the damping factor is increasing. This is because the ratio of magnetic NiFe alloy is reducing with doping more and more nonmagnetic Cu in a fixed volume. In addition, the Cu atoms in $(Ni_{80}Fe_{20})_{1-x}Cu_x$ alloy plays a role as purity that leads the enhancement of the energy consumption, i.e., a larger damping.

In Figure 3.5(a)−(i), we plot the measured FMR signals in samples of $Co_{90}Fe_{10}(10)/Ta(t)/(Ni_{80}Fe_{20})_{1-x}Cu_x(10)$ where t = 0, 0.5, 1 nm and x = 0, 35, 45. As expected, the AM of $Co_{90}Fe_{10}$ (10)/$Ni_{80}Fe_{20}$(10) in Figure 3.5 (a) has the highest intensity, to which we have normalized the magnitudes of FMR signals measured in all other samples for clarity. The comparison between Figure 3.5 (a), (d) and (g), where t=0, 0.5, 1 nm, respectively, shows that OM (upper branch) gradually appears and becomes stronger with increasing the Ta thickness. The maximum resonant frequencies at $\mu_0 H$ = 100 mT are 11.7 GHz(AM), 14.0 GHz(OM), and 12.8 GHz(OM), respectively. Similar phenomenon also has been observed in samples with x = 35 (middle panel) or 45 (right panel). It is noted that the highest resonant frequency of OM should be found in the sample with t = 0, but it is too weak to be observed in our experiment. These experimental behaviors are clearly in good agreement with the simulations in Section 3.1.2. In addition, for samples with t = 0 as shown in Figure 3.5 (a)−(c), only the AM modes have been observed and the intensity is reducing with increasing x due to the reduction of the total magnetization of the bilayers. When t = 0.5 nm, both AM and OM are observed as shown in Figure 3.5

(d)−(f). Interestingly, their intensities exhibit opposite trends as a function of the applied field, i.e., OM(AM) branch becomes stronger(weaker) with the applied magnetic field. The simulations (Figure 3.3(b)) show similar results, although the effect not as strong as the experimental results. In general, the magnetic susceptibility decreases with increasing field (frequency), the opposite trend in OM mode suggests the difference between the susceptibilities in two FM layers outweighs the reduction of the susceptibilities as a function of the applied field (frequency). This can be a useful feature in applications.

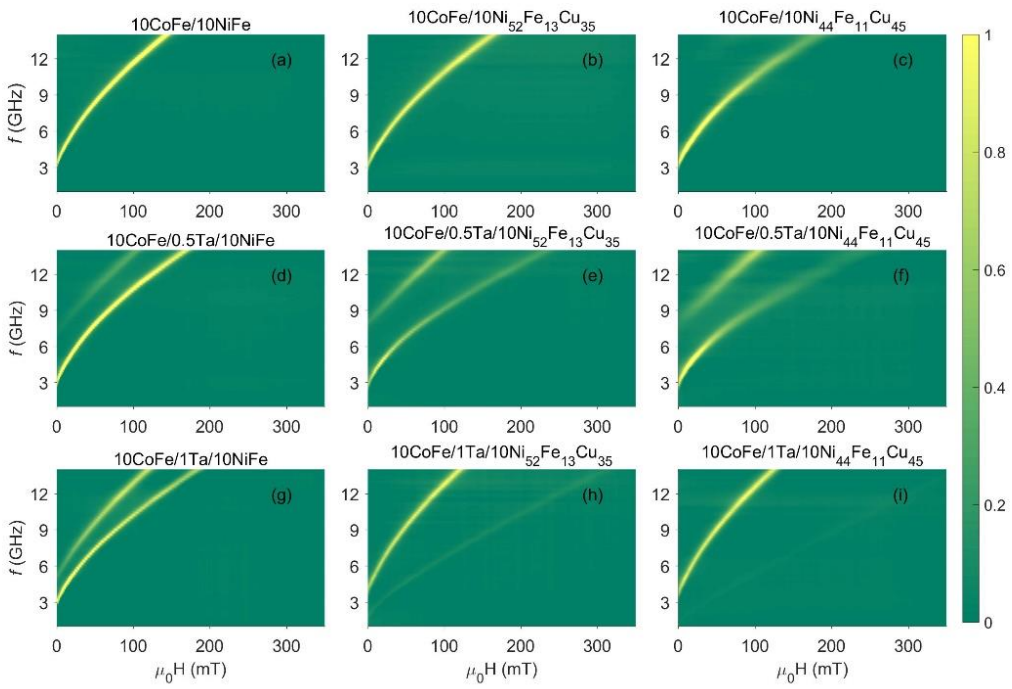

Figure 3.5 The measured FMR signals shown in the form of color maps for CoFe/Ta/$(Ni_{80}Fe_{20})_{1-x}Cu_x$ samples. The left, middle, and right panels correspond to samples with x = 0, 35, and 45, respectively. The top, middle, and bottom panels correspond to samples with Ta thickness t = 0, 0.5, and 1nm, respectively. The magnitude of FMR signal in all color maps are normalized to the maximum magnitude in (a).

It is also found that the frequency of the OM at $\mu_0 H$ = 100 mT does not change much (~14 GHz) with increasing the Cu concentration in $(Ni_{80}Fe_{20})_{1-x}Cu_x$ layer, while the intensity at this frequency has been enhanced by 210%. The enhancement is even larger at a higher resonant frequency. On the contrary, increasing the Cu composition reduces both the resonant frequency and intensity of AM. For samples with t = 1 nm in Figure 3.5 (g)−(i), the exchange coupling is significantly weakened by the thick Ta

spacer such that the OM and AM are approximately corresponding to the FMR signal of single $Co_{90}Fe_{10}$ and $(Ni_{80}Fe_{20})_{1-x}Cu_x$ layer, respectively. However, the crucial difference from individual layers is the intensity of OM increases with increasing field (frequency), a feature that cannot observed in single FM layer.

3.2.2 Analyses of Spacer Thickness Dependent Exchange Coupling

Up to now, we have demonstrated that both AM and OM in coupled $Co_{90}Fe_{10}(10)/Ta(t)/(Ni_{80}Fe_{20})_{1-x}Cu_x(10)$ samples can be substantially tailored by the Ta spacer thickness or magnetization difference between two FM layers. We now quantitatively investigate the dependence of exchange coupling strength as a function of the spacer thickness and the saturation magnetization.

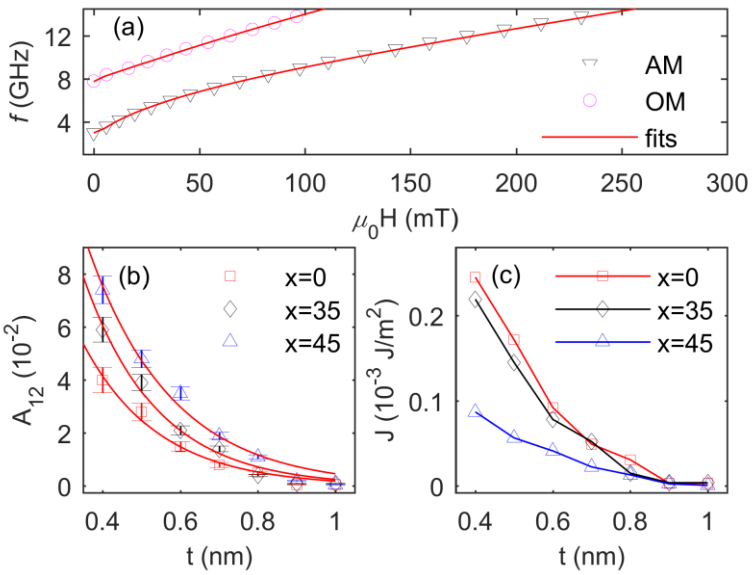

Figure 3.6 The fitting (red lines) to FMR dispersion relations (open symbols are extracted resonant frequencies vs fields) in sample $Co_{90}Fe_{10}(10)/Ta(0.5)/Ni_{52}Fe_{13}Cu_{35}(10)$. (b) Extracted A_{12} as a function of the Ta thickness t in three series of samples with x = 0, 35, 45. (c) Calculated exchange coupling coefficient J corresponding to the samples in (b).and M_{s2} at fixed A_{12} = 0.025 and $\mu_0 H$ = 80 mT.

The exchange coupling strength A_{12} can be extracted by fitting the measured OM and AM spectra. As shown in Figure 3.6(a) the best fit (red curves) to the experimental data (open symbols) gives $A_{12} = 0.039$ in sample $Co_{90}Fe_{10}(10)/Ta(0.5)/Ni_{52}Fe_{13}Cu_{35}(10)$. The thickness dependence of A_{12} is presented in Figure 3.6(b) where the squares, diamonds and triangles symbols represent samples with $x = 0$, 35, 45, respectively. It is found that A_{12} inversely depends on t in all samples, regardless of Cu dopant in NiFe. In Figure 3.6(c) we show the thickness-dependent exchange coupling coefficient J calculated using Eq (3.4) and (3.6). Again, for a fixed Cu concentration, J continuously decreases with increasing the Ta thickness. A similar behavior has been reported in a CoFeB/Ta/CoFeB trilayer[24]. Such a monotonic dependence on the spacer layer thickness, instead of an oscillatory variation of J, suggests the Néel "orange-peel" coupling, which predicts an exponential decay of coupling energy on spacer thickness [25-27], is a dominant mechanism in our samples. To further confirm there is no antiferromagnetic (AFM) coupling in our samples, we have compared the magnetic hysteresis loops of single layer and coupled trilayer samples as shown in Figure 3.7(a). In $Co_{90}Fe_{10}(10)/Ta(0.5)/Ni_{80}Fe_{20}(10)$ sample we observe a single loop with coercivity in between those of single $Ni_{80}Fe_{20}(10)$ and $Co_{90}Fe_{10}(10)$ layer. As comparison in Figure 3.7(b), we replace the 0.5 nm Ta with a 0.5 nm Ru spacer and the measured hysteresis loop shows very different feature from Ta-spaced sample. The multi-stage hysteresis loop indicates the AFM coupling in Ru-spaced sample [28]. The hysteresis loop of CoFe(10)/Ta(0.5)/NiFe(10) does not exhibit this step-like profile, which suggests no established AFM coupling in this sample, i.e., direct FM coupling dominates. All those results further confirm the domination of FM coupling in our samples with Ta spacer layer.

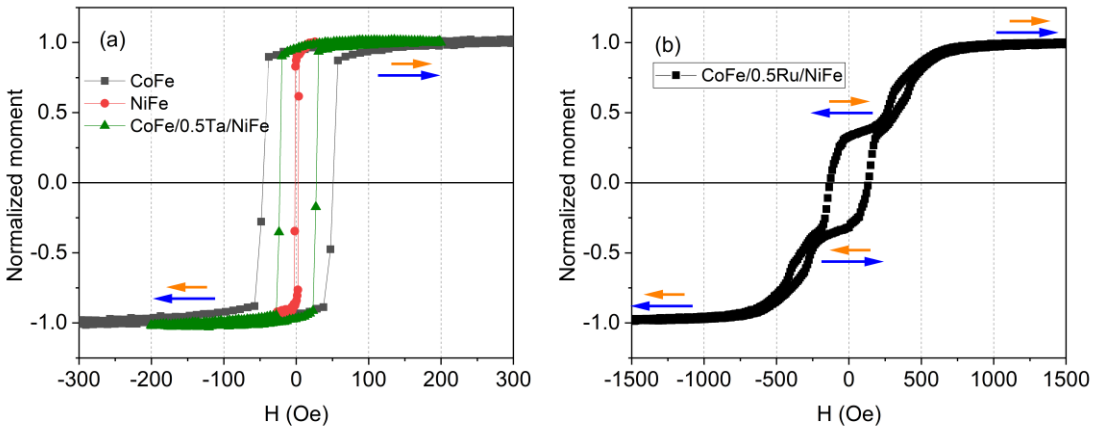

Figure 3.7 The magnetic hysteresis loops of the samples were measured in Magnetic Property Measurement System (MPMS) at room temperature. (a) black squares, red solid circles and green triangles represent the data of CoFe(10), NiFe(10) and CoFe(10)/Ta(0.5)/NiFe(10), respectively. (b) control sample CoFe(10)/Ru(0.5)/NiFe(10). The orientation of the magnetization in CoFe layer and NiFe layer are labeled by blue arrow and orange arrow, respectively.

3.3 Néel "Orange Peel" Coupling

Our fitting results show that the dependence of J on the thickness of spacer t has no oscillatory nature, which highly recommends the domination of Néel "orange-peel" coupling in our trilayer samples. Néel "orange-peel" coupling was proposed to explain the hysteresis loop shift (exchange coupling) measured in a spin valve structure. It attributes the shift field to the roughness of interface in in the pinned layer due to correlated waviness of the magnetic layers.

For in-plane magnetization in each FM layer, theoretical model of the "orange-peel" coupling gives the coupling coefficient [29,30]

$$J(t) = \frac{\pi^2 h^2}{\sqrt{2}\lambda} M_{\rho s} M_{vs} \exp[-\frac{2\pi\sqrt{2}}{\lambda} t], \qquad (3.8)$$

where t is the thickness of spacer, h is the interface roughness amplitude and λ is the wavelength of roughness modulation. According to Eq (3.4), (3.6) and (3.8), the exchange coupling strength A_{12} can be written by

$$A_{12}(t) = \frac{\pi^2 h^2}{\sqrt{2}\lambda t_{FM}} \exp[-\frac{2\pi\sqrt{2}}{\lambda} t], \tag{3.9}$$

where t_{FM} is the thickness of FM layer, i.e., 10 nm in our case. We can use Eq (3.9) to fit the data in Figure 3.6(b), which leads to h = 0.32 nm, 0.39 nm and 0.41 nm and λ = 4.3 nm, 4.1 nm, 4.7 nm for trilayer samples with x = 0, 35, 45, respectively. Increasing values of h with x suggests that the Cu doping in NiFe layer increases its roughness. We confirm this by measuring the roughness of our samples using the Atomic Force Microscopy. The microscopic images are shown in Figure 3.8.

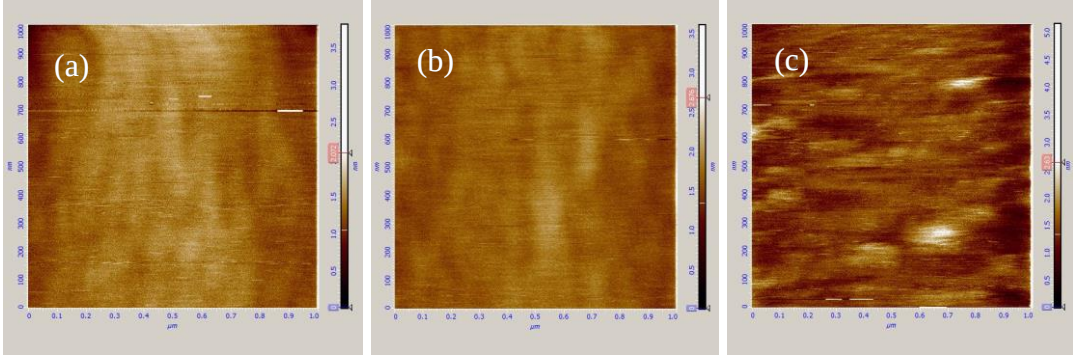

Figure 3.8 The microscopic images of the film surfaces of the sample (a) $Ni_{80}Fe_{20}$(10), (b) $Ni_{52}Fe_{13}Cu_{35}$(10) and (c) $Ni_{44}Fe_{11}Cu_{45}$(10). The surface topographies were obtained by scanning a 1μm×1μm area using Atomic Force Microscope.

The measured average roughness R is 0.11 nm, 0.16 nm, 0.23 nm for the 0.5 nm Ta spaced samples with x = 0, 35, 45, respectively. This increasing trend of the surface roughness with the concertation of doped Cu in NiFe layer is consistent with our fit

result. This suggests that “orange-peel” mode is applicable to describe the coupling in our trilayers. It should also be noted that a larger doping always gives rise to a relatively higher value of A_{12} (Figure 3.6(b)), but smaller value of J (Figure 3.6(c)). This is because in the definition of A_{12} we exclude the contribution from the magnetization terms (see Eq (3.8) and (3.9)). Given the thickness of each layer, A_{12} only depends on the interfacial roughness, which is useful to exam the interfacial contribution to exchange coupling in our trilayers. When the magnetization is considered, J is a better parameter to describe the exchange coupling. It is now understandable that introduction of nonmagnetic Cu impurities enhances the interface roughness and thus the exchange coupling strength, and, on the other hand, reduces magnetization in one of the FM layers and decreases the energy exchange density.

3.4 Summary

In this chapter, we have systematically investigated two magnetic resonance modes in ferromagnetically coupled FM1/NM/FM2 layers. The two modes are calculated by correlating each FM layer via exchange-coupling-induced effective fields. Experimentally, the frequency and intensity of the two modes in CoFe/Ta/NiFe(Cu) trilayer systems are taiored by the Ta spacer thickness as well as the saturation magnetization in NiFe(Cu) alloy layer. Both our theoretical simulation and experiment clearly demonstrate that the resonance frequency of the OM can be significantly higher than that of individual layer and the intensity of the OM can be significantly enhanced by increasing the contrast in the saturation magnetization in two FM layers. It is also found that the intensity of the OM, unlike the FMR of a single FM layer, increases with increasing applied magnetic field or frequency, which can be very useful in microwave applications. Finally, the exponential relation of the exchange

coupling strength as a function of the Ta layer thickness suggests the domination of FM coupling in our samples, which can be explained by the “orange-peel” coupling theory. The increased coupling strength with the concentration of Cu dopant is attributed to the increasing roughness in our samples by doping.

REFERENCES

[1] Z. Hu *et al.*,"*Non-volatile ferroelectric switching of ferromagnetic resonance in NiFe/PLZT multiferroic thin film heterostructures*", Scientific reports **6**, 32408 (2016).

[2] Y. Chen, A. Yang, M. R. Paudel, S. Stadler, C. Vittoria, and V. Harris,"*Microwave magnetoelectric coupling and ferromagnetic resonance frequency tuning of a Co 2 MnSb/GaAs/PZN-PT heterostructure*", Physical Review B **83**, 104406 (2011).

[3] R. Xiong, W. Zhang, B. Fang, G. Li, Z. Li, Z. Zeng, and M. Tang,"*Ferromagnetic resonance manipulation by electric fields in Ni81Fe19/Bi3. 15Nd0. 85Ti2. 99Mn0. 01O12 multiferroic heterostructures*", Applied Physics Letters **113**, 172407 (2018).

[4] X. Liu, H. T. Nguyen, J. Ding, M. Cottam, and A. Adeyeye,"*Interlayer coupling in Ni 80 Fe 20/Ru/Ni 80 Fe 20 multilayer films: Ferromagnetic resonance experiments and theory*", Physical Review B **90**, 064428 (2014).

[5] Y. Chen, X. Fan, Y. Zhou, Y. Xie, J. Wu, T. Wang, S. T. Chui, and J. Q. Xiao,"*Designing and tuning magnetic resonance with exchange interaction*", Advanced Materials **27**, 1351 (2015).

[6] S. Li, Q. Li, J. Xu, S. Yan, G. X. Miao, S. Kang, Y. Dai, J. Jiao, and Y. Lü,"*Tunable optical mode ferromagnetic resonance in FeCoB/Ru/FeCoB synthetic antiferromagnetic trilayers under uniaxial magnetic anisotropy*", Advanced Functional Materials **26**, 3738 (2016).

[7] D. Richardson, K. Srinivasan, A. Kalitsov, A. Ajan, S. Jain, S. Katz, and M. Wu,"*Interlayer Exchange Coupling in Magnetic Hard-Soft Bilayered Structures*", Physical Review Applied **11**, 044016 (2019).

[8] R. C. O'handley, *Modern magnetic materials: principles and applications* (Wiley, 2000).

[9] W. Muir, J. Cochran, J. Rudd, B. Heinrich, and Z. Celinski,"*Observation of the exchange-coupled modes in Fe (001)/Pd/Fe (001) ultrathin trilayers*", Journal of magnetism and magnetic materials **93**, 229 (1991).

[10] B. Heinrich, S. Purcell, J. Dutcher, K. Urquhart, J. Cochran, and A. Arrott,"*Structural and magnetic properties of ultrathin Ni/Fe bilayers grown epitaxially on Ag (001)*", Physical Review B **38**, 12879 (1988).

[11] F. Keffer and C. Kittel,"*Theory of antiferromagnetic resonance*", Physical Review **85**, 329 (1952).

[12] K. Lenz, T. Toliński, J. Lindner, E. Kosubek, and K. Baberschke,"*Evidence of spin-pumping effect in the ferromagnetic resonance of coupled trilayers*", Physical Review B **69**, 144422 (2004).

[13] P. Bruno and C. Chappert,"*Ruderman-Kittel theory of oscillatory interlayer exchange coupling*", Physical Review B **46**, 261 (1992).

[14] D. Edwards, J. Mathon, R. Muniz, and M. Phan,"*Oscillations of the exchange in magnetic multilayers as an analog of de Haas–van Alphen effect*", Physical review letters **67**, 493 (1991).

[15] M. D. Stiles,"*Exchange coupling in magnetic heterostructures*", Physical Review B **48**, 7238 (1993).

[16] M. Belmeguenai, T. Martin, G. Woltersdorf, M. Maier, and G. Bayreuther,"*Frequency-and time-domain investigation of the dynamic properties of interlayer-exchange-coupled Ni 81 Fe 19 ／ Ru ／ Ni 81 Fe 19 thin films*", Physical Review B **76**, 104414 (2007).

[17] Y. Wei *et al.*,"*Exponentially decaying magnetic coupling in sputtered thin film FeNi/Cu/FeCo trilayers*", Applied Physics Letters **106**, 042405 (2015).

[18] D. T. Pierce, J. A. Stroscio, J. Unguris, and R. Celotta,"*Influence of Cr growth on exchange coupling in Fe/Cr/Fe (100)*", Physical Review B **49**, 14564 (1994).

[19] H. Chen, X. Fan, W. Wang, H. Zhou, Y. Gui, C.-M. Hu, and D. Xue,"*Electric detection of the thickness dependent damping in Co90Zr10 thin films*", Applied Physics Letters **102**, 202410 (2013).

[20] Z. Zhang, L. Zhou, P. Wigen, and K. Ounadjela,"*Angular dependence of ferromagnetic resonance in exchange-coupled Co/Ru/Co trilayer structures*", Physical Review B **50**, 6094 (1994).

[21] A. Franco and P. Landeros,"*Ferromagnetic resonance of an heterogeneous multilayer system with interlayer exchange coupling: an accessible model*", Journal of Physics D: Applied Physics **49**, 385003 (2016).

[22] A. Layadi,"*Effect of biquadratic coupling and in-plane anisotropy on the resonance modes of a trilayer system*", Physical Review B **65**, 104422 (2002).

[23] S. Mathias *et al.*,"*Probing the timescale of the exchange interaction in a ferromagnetic alloy*", Proceedings of the National Academy of Sciences **109**, 4792 (2012).

[24] T. McKinnon, P. Omelchenko, B. Heinrich, and E. Girt,"*FMR study of interlayer exchange coupling in FeCoB| Ta| FeCoB trilayers with in-plane anisotropy*", Journal of Applied Physics **123**, 223903 (2018).

[25] L. Néel,"*Magnetisme-sur un nouveau mode de couplage entre les animantations de deux couches minces ferromagnetiques*", Comptes Rendus Hebdomadaires Des Seances De L Academie Des Sciences **255**, 1676 (1962).

[26] B. Schrag *et al.*,"*Néel "orange-peel" coupling in magnetic tunneling junction devices*", Applied Physics Letters **77**, 2373 (2000).

[27] J. Moritz, F. Garcia, J. Toussaint, B. Dieny, and J. Nozières,"*Orange peel coupling in multilayers with perpendicular magnetic anisotropy: Application to (Co/Pt)-based exchange-biased spin-valves*", EPL (Europhysics Letters) **65**, 123 (2004).

[28] J. Fassbender, L. Bischoff, R. Mattheis, and P. Fischer,"*Magnetic domains and magnetization reversal of ion-induced magnetically patterned Ruderman-Kittel-Kasuya-Yoshida-coupled Ni 81 Fe 19 ／ Ru ／ Co 90 Fe 10 films*", Journal of applied physics **99**, 08G301 (2006).

[29] T. Luciński, A. Hütten, H. Brückl, T. Hempel, S. Heitmann, and G. Reiss,"*Magnetoresistive properties of Ni80Fe20/Co1/CuAgAu/Co2 pseudo - spin - valves*", physica status solidi (a) **196**, 97 (2003).

[30] B. Schrag, A. Anguelouch, G. Xiao, P. Trouilloud, Y. Lu, W. Gallagher, and S. Parkin,"*Magnetization reversal and interlayer coupling in magnetic tunneling junctions*", Journal of Applied Physics **87**, 4682 (2000).

Chapter 4

INVESTIGATION OF SPIN ORBIT TORQUES IN FERROMAGNETIC HETEROSTRUCTURES VIA TIME-RESOLVED MOKE MEASUREMENT

4.1 Motivation

It is known that the STT-MRAM has the potential to become a leading storage technology due to its high storage density and low power consumption. As shown in Figure 1.5 (a), a flowing of charge current through the fixed layer of MTJ unit can generate a spin current (due to spin filter effect) which can exert torque on the free layer to switch it. However, this switching relies on the thermal fluctuation of the magnetization in fixed layer and requires a high critical switching current. Instead of using the perpendicular charge current, the SOT-MRAM technology, as in Figure 1.5 (b), uses a in plane charge current flowing in a heavy metal that is adjacent to the free layer. Due to the spin orbit coupling (SOC) in HM, a transverse spin current is generated and injected into upper free layer. This spin current will exert two torques on free layer for switching, damping-like (DL) and field-like (FL) torques. The switching in SOT-MRAM is independent on the magnetization in the fixed layer and more efficient than STT-MRAM.

The SOTs induced two effective fields can also drive the magnetization dynamic and subsequently finalize the magnetization to a steady position. Many methods have been developed to extract SOTs when the system is in a steady state, but rare reports regarding the affection of SOTs during the unsteady magnetization dynamics. We are interested in this SOTs driven dynamics and curious that whether

the SOTs can be extracted from the measured magnetization dynamics. In this chapter, we will discuss how we measure this ultra-fast dynamics and extract the SOTs from the unsteady state.

4.2 Spin Orbit Torque Driven Magnetization Dynamics

In Section 1.4, we have introduced SOTs induced by current flowing in a FM/NM heterostructure. Compared with STT, SOTs own a higher efficiency in magnetization switching and can extend its application to the switching of magnetic insulators and antiferromagnets. Two SOTs are determined by the spin polarization and magnetization of the magnetic layer as described in Eq (1.41). While the microscopic origins of SOTs are still debatable, the contribution of these two torques to the magnetization dynamics can be described by the Landau–Lifshitz–Gilbert–Slonczewski equation [1,2],

$$\frac{d\mathbf{m}}{dt} = -\gamma(\mathbf{m}\times\mathbf{H}_{eff}) + \alpha(\mathbf{m}\times\frac{d\mathbf{m}}{dt}) - \tau_{\mathbf{DL}}\mathbf{m}\times(\mathbf{m}\times\boldsymbol{\sigma}) - \tau_{\mathbf{FL}}\mathbf{m}\times\boldsymbol{\sigma}\,, \qquad (4.1)$$

where $\boldsymbol{m}$ is the reduced magnetization vector, γ is the gyromagnetic ratio, α is the damping factor, $\boldsymbol{\sigma}$ is the polarization direction of the incoming spin (generally in-plane and orthogonal to the current flow direction), $\boldsymbol{H}_{eff}$ is the total effective field that includes the external field $\boldsymbol{H}_{ext}$, anisotropy field $\boldsymbol{H}_{ani}$ and charge current-induced Oersted field $\boldsymbol{h}_{Oe}$. When the magnetic moments are orthogonal to the vector $\boldsymbol{\sigma}$, τ_{DL} and τ_{FL} can be considered as equivalent effective fields $\boldsymbol{h}_{DL}$ and $\boldsymbol{h}_{FL}$ in the direction of $\boldsymbol{m}\times\boldsymbol{\sigma}$ and $\boldsymbol{\sigma}$ with amplitude of $(\hbar/2e)(j\varepsilon/M_s t_{FM})$ and $(\hbar/2e)(j\varepsilon'/M_s t_{FM})$ [3-5], respectively, where $\hbar$ is the reduced Planck's constant, e is the electron charge, j is the charge current density, M_s is the saturation magnetization, t_{FM} is the thickness of the ferromagnetic layer, ε (half of the spin Hall angle θ_{SH} of the HM material) and ε' are the efficiencies of $\boldsymbol{h}_{DL}$ and $\boldsymbol{h}_{FL}$, respectively.

There has been great interest in the role of SOTs in magnetization dynamics because of the applications of HM/FM heterostructures in magnetic memory devices. Two theoretical models have been proposed to understand the underlying mechanism: 1) the macro-spin approximation and 2) the micromagnetic model. The macro-spin approximation assumes all microscopic magnetic moments respond identically and coherently to excitations. In the macro-spin model, $\boldsymbol{h}_{DL}$ induces the rotation of magnetization and $\boldsymbol{h}_{FL}$ assists the precession of magnetization about the $\boldsymbol{\sigma}$ vector [5,6]. Micromagnetic models are based on the idea that the magnetization reversal is triggered by random nucleation and executed by the domain wall propagation across the magnetic layer. In the micromagnetic model, $\boldsymbol{h}_{FL}$ triggers the reversal process and $\boldsymbol{h}_{DL}$ is responsible for driving the domain expansion [7-9].

The DL and FL torques have been widely studied experimentally through the measurement of magnetoresistances, like the mostly applied second Harmonic measurement [10-13]. Alternatively, SOTs can also be studied using an all-optical MOKE measurement [14,15]. We also want to note that MOKE-based SOT measurements are immune to thermal effects, providing an advantage relative to electrical measurements such as second harmonic measurement that are impacted by thermal gradients. However, these quasi-DC experiments cannot probe SOT-driven magnetization dynamics, in particular the fast oscillations that can be induced by FL torque. TR MOKE has emerged as a powerful to explore magnetization dynamics [6,16,17]. However, most of the attention has been focused on the effect of SOTs on switching properties and there has been little work regarding the extraction of SOTs from dynamic measurements. One reason is that the dynamic oscillations of the magnetization are influenced by the magnetization and effective damping of the

materials, the total effective fields, and more, which makes the analysis complicated. On the other hand, if one can fit the measured magnetization dynamics with an appropriate theory [18,19], it would provide a means of extracting all the relevant parameters.

In this chapter, we demonstrate the extrapolation of the current induced effective fields $\boldsymbol{h}_{DL}$ and $\boldsymbol{h}_{FL}$ in Py(3)/Pt(3) and Ta(3)/CoFeB(3) bilayers using the TR MOKE measurement. As a control experiment, we also characterize the values of those two fields from DC MOKE measurement for comparison with the results measured by TR MOKE.

4.3 Measuring SOT Effective Fields Using DC MOKE

From Eq (1.90), we know that the polar MOKE measures out-of-plane magnetization m_z while the quadratic MOKE signal is proportional to $m_x m_y$. Figure 4.1 shows a FM/HM heterostructure with the unit magnetization vector **m** of the FM layer initially oriented at a direction characterized by a polar angles θ_M and azimuthal φ_M with respect to z and *x* axes, respectively. Thus, the Eq (1.90) can be equivalently written as

$$\theta_{KR}(\theta, \varphi) = \alpha_{Polar} \cos\theta_M + \frac{1}{2}\beta_{Quadratic} \sin^2\theta \sin 2(\varphi_M - \varphi_{pol}) . \qquad (4.2)$$

Here we use θ_{KR} to represent Kerr rotation and φ_{pol} is the polarization angle of the incident laser. It is noted that in Eq (1.90) the φ_{pol} is set to be zero but here we include this parameter. When a current pass through the bilayer, the magnetization in FM layer subjects to $\boldsymbol{h}_{DL}$ field that is in perpendicular to the film plane and $\boldsymbol{h}_{FL}$ field in the film plane and transverses to the current direction according to Eq (4.1). As a result, $\boldsymbol{h}_{DL}$ and $\boldsymbol{h}_{FL}$ fields will rotate **m** out-of-plane and in-plane towards y-direction by a small

angle $\Delta\theta_M$ and $\Delta\varphi_M$, respectively. To the first order approximation for an in-plane magnetized FM layer,

$$\Delta\theta_M = \frac{h_{DL}}{H_{ext} + H_a + M_s}, \tag{4.3}$$

$$\Delta\varphi_M = \frac{h_{FL} + h_{Oe}}{H_{ext} + H_a}, \tag{4.4}$$

where H_a is the in-plane anisotropy effective field and h_{Oe} is the current induced Oersted field along the *y*-direction if the current is flowing along the *x*-direction.

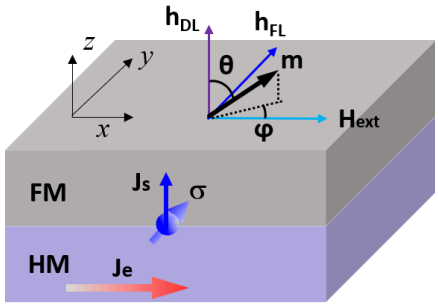

Figure 4.1 Diagram of the effective fields in a FM/HM heterostructure. A spin current polarized in transverse direction is produced and driven along out-of-plane direction. θ_M and φ_M are the polar and azimuthal angles of **m**, respectively.

In DC MOKE measurements, the current induced Kerr rotation can be obtained by taking the derivative of Eq (4.2) with respect to θ_M and φ_M.

$$\begin{aligned}\Delta\theta_{KR} = &-\alpha_{Polar}\sin\theta_M\Delta\theta_M \\ &+\beta_{Quadratic}\sin\theta\cos\theta\sin 2(\varphi_M - \varphi_{pol})\Delta\varphi_M + \sin^2\theta\cos 2(\varphi_M - \varphi_{pol})\Delta\varphi_M\end{aligned}. \tag{4.5}$$

In our sample the initial state is $\theta_M = \pi/2$ and $\varphi_M = 0$, which further simplifies Eq (4.5) to

$$\Delta\theta_{KR} = -\alpha_{Polar}\sin\theta_M\Delta\theta_M + \beta_{Quadratic}\cos 2\varphi_{pol}\Delta\varphi_M . \tag{4.6}$$

It is seen from Eq (4.3), (4.4) and (4.6) that the $\boldsymbol{h}_{DL}$ dominates the change on polar MOKE signal while $\boldsymbol{h}_{FL}$ dominates the change on quadratic MOKE signal. Therefore,

the two effective fields can be measured separately by isolating polar and quadratic signal from each other. If we use a linearly polarized leaser with the polarization φ_{pol} = 45°, the second term in Eq (4.6) vanishes. Only polar MOKE signal is measured by balanced detector. On the other hand, if we use a circularly polarized leaser, the first term contributes nothing to the Kerr rotation since the out-of-plane magnetization does not change the polarization of a circularly polarized light. Thus, the second term is solely measured.

The film structures and magnetic hysteresis loops are shown in Figure 4.2. we reverse the //HM/FM sequence (// indicates the substrate side) in //3Py/3Pt bilayer sample since Py is easily to be oxidized and the top Pt layer also plays a role as capping layer. When a charge current $\boldsymbol{j}$ flows along the x axis, the spin current with polarization ($\boldsymbol{\sigma}$) in the y direction ($\boldsymbol{j}_s = \theta_{SH}\boldsymbol{\sigma} \times \boldsymbol{j}$) [20-22] flows into the Py layer due to the bulk SHE in the Pt layer or the interfacial Rashba effect at the HM/FM interface. The magnetization of the Py was initially saturated by a static external magnetic field along the x axis. Under this geometry, the DC polar MOKE is proportional to m_z, tilted by the effective field $\boldsymbol{h}_{DL}$. The in-plane Oersted field $\boldsymbol{h}_{Oe//}$ induced by the current in the HM layer points in the same direction as $\boldsymbol{h}_{FL}$ in the Py /Pt sample as drawn in Figure 4.2 (a), but points in the direction opposite $\boldsymbol{h}_{FL}$ in the //3Ta/3CoFeB as shown in Figure 4.2 (b). We show the normalized magnetic hysteresis loops of the two samples Figure 4.2 (c) and (d), respectively, obtained by sweeping the magnetic field along the in-plane easy (y) and hard (x) axes in MPMS. The sharp square loops indicate the existing effective anisotropic fields along the easy axes and the coercivities were found to be 2.6 Oe in //3Py/3Pt and 3.7 Oe in //3Ta/3CoFeB.

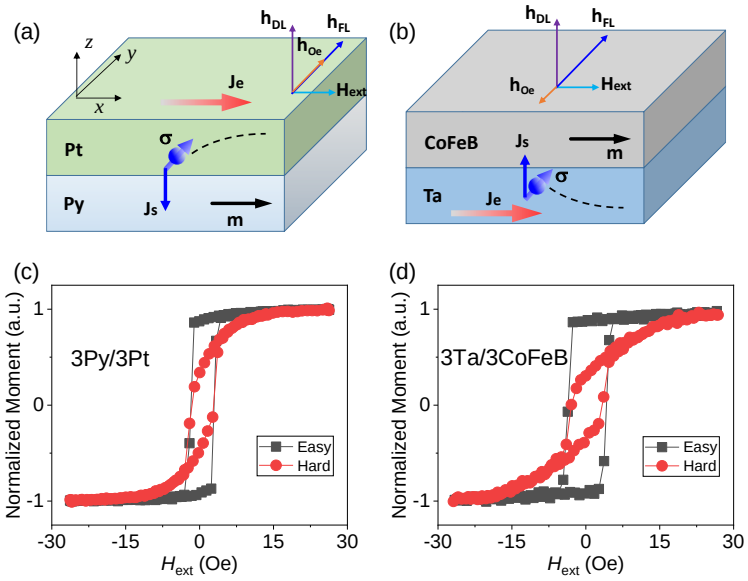

Figure 4.2 (a), (b) Schematic of //3Py/3Pt and //3Ta/3CoFeB sample structure and the current-induced effective fields. Magnetization in Py layer is aligned in the same direction with current. Spin current j_s with spin polarization in y direction flowing into Py layer exerts out-of-plane $\boldsymbol{h}_{DL}$ and in-plane $\boldsymbol{h}_{FL}$. $\boldsymbol{h}_{FL}$ and $\boldsymbol{h}_{Oe}$ point opposite directions in two samples due to opposite HM/FM growth sequence and opposite spin Hall angles in Pt and Ta layers. (c) and (d) Magnetic hysteresis loop of //3Py/3Pt and //3Ta/3CoFeB samples, respectively.

The geometry of the device for DC MOKE measurement is shown in Figure 4.3. The bilayer sample used for DC MOKE measurements was patterned into a 50 × 50 μm^2 square where the laser will shine on. Besides, to calibrate the perpendicular h_{DL} field, along current direction two 50-μm-wide metal wires made of 10Ti/80Au were placed on two sides of the sample with a center-to-center distance of 100 μm. The two wires were connected in series when a DC current passes through them, such that the induced out-of-plane Oersted field is doubled and in-plane Oersted fields is cancelled at the center of the bilayer sample, giving rise to a well-defined calibration

field. (The device design is created by Clewin 5 software and attached in Appendix C).

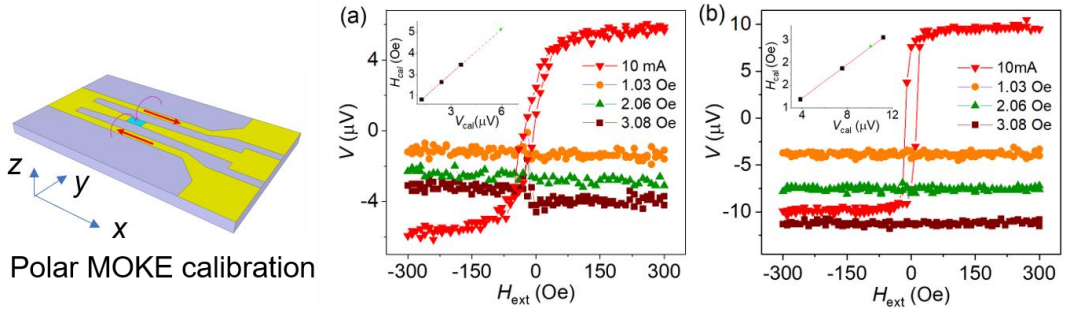

Figure 4.3 The structure of our device for polar MOKE measurements. The light blue area represents the FM/HM sample which are inserted into a calibration wire indicated by yellow area. (a) and (b) show the measured results for Py(3)/Pt(3) and Ta(3)/CoFeB(3), respectively.

The setup of our DC MOKE measurement was introduced in Section 2.6.1. With setting φ_{pol} = 45°, the contribution of polar MOKE is obtained and shown in Figure 4.3 (a) and (b) for Py/Pt and Ta/CoFeB samples, respectively. An effective electrical current of 10 mA is applied to the //3Py/3Pt sample. We compute using a parallel resistor model that 7 mA flows through the Pt layer, corresponding to the current density $j_{Pt} = 4.7\times10^{10}$ A/m^2. The θ_{KR} (in units of balanced bridge photodiode voltage) as a function of $\boldsymbol{H}_{ext}$ is shown in Figure 4.3 (a) where a hysteresis loop is observed because $\boldsymbol{h}_{DL}\sim\boldsymbol{m}\times\boldsymbol{\sigma}$. We note that we focused the laser spot to a spot size less than 4 μm at the center of the 50-μm-wide sample such that the induced out-of-plane Oersted field ($\boldsymbol{h}_{Oe\perp}$) from the current was negligible in our experiments. The amplitude of $\boldsymbol{h}_{DL}$ was calibrated by passing current through the calibration wires

parallel to the sample, which introduces calibration field $\boldsymbol{h}_{cal}$ in the same direction as $\boldsymbol{h}_{DL}$. The θ_{KR} induced by $\boldsymbol{h}_{cal}$ is constant as a function of $\boldsymbol{H}_{ext}$ as shown in Figure 4.3 (a) because the calibration field is independent of the magnetization direction. In addition, the θ_{KR} is linearly proportional to the calibration field strength as shown in the inset of Figure 4.3 (a). From these calibrations $\boldsymbol{h}_{DL}$ is determined to be 5.23 Oe in the //3Py/3Pt bilayer. The value of $\boldsymbol{h}_{DL}$ corresponds to $\beta_{\mathrm{Pt\_}DL}$=8.9 nm where β is the SOT efficiency, defined as the ratio of induced effective field to current density in HM layer in unit of Oe/(Am^{-2}) or nm.

We next compute the spin Hall angle θ_{SH} by using the equation $(\hbar/2e)(j\theta_{SH}/2M_{\mathrm{s}}t_{FM}) = h_{DL}$. We note that the effective magnetization M_{eff} is related to M_{s} and the uniaxial anisotropy field H_a by the relationship $4\pi M_{\mathrm{eff}} = 4\pi M_{\mathrm{s}} - H_a$. $4\pi M_{\mathrm{eff}}$ is of order 10^4 Oe, while $H_a \leqslant 40$ Oe. We therefore make the approximation of $M_{\mathrm{eff}} \approx M_{\mathrm{s}}$, resulting in $(\hbar/2e)(j\theta_{SH}/2M_{\mathrm{eff}}t_{FM}) = h_{DL}$. Using the value of M_{eff_Py} extracted from the FMR measurements (760 emu/cm^3, we show the data later), we calculate a spin Hall angle for the //3Py/3Pt sample of $\theta_{SH} = 0.077$. Similarly, for the //3Ta/3CoFeB sample an electrical current of 10 mA corresponds to $j_{\mathrm{Ta}} = 2.1\times10^{10}$ A/m^2 and we determine $\beta_{\mathrm{Ta\_}DL} = -10.6$ nm and $\theta_{SH\_\mathrm{Ta}} = -0.112$ from the measured data shown in Figure 4.3 (b). Here, $M_{eff\_\mathrm{CoFeB}} = 960$ emu/cm^3 was used in the calculation. All the extracted values for these parameters for Pt and Ta are similar to previously reported values [14,23].

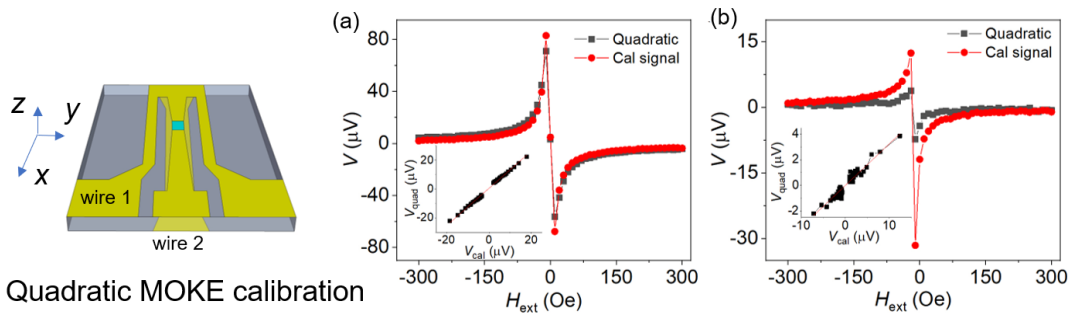

Figure 4.4 The structure of our device for quadratic MOKE measurements. The calibration wire 2 is attached underneath the substrate. (a) and (b) show the measured results for Py(3)/Pt(3) and Ta(3)/CoFeB(3), respectively.

To characterize the FL torque, we studied the θ_{KR} as a function of $\boldsymbol{H}_{ext}$ (red squares) in the Py/Pt and Ta/CoFeB samples as shown in Figure 4.4 (a) and (b), respectively. The θ_{KR} changes sign at $H_{ext} = 0$ because the quadratic signal is proportional to the product of $m_x \cdot m_y$ where m_y keeps the same orientation but m_x changes sign when $\boldsymbol{H}_{ext}$ is reversed. The distinctive $1/H$ relation with H_{ext} was observed in our experiment similar to previous reports [14]. To calibrate the $\boldsymbol{h}_{FL}$, we measured the field dependent θ_{KR} signal from the samples while only a calibration field was applied in the y direction without passing the current through the samples. The calibration field was produced by a 300-μm-wide and 100-nm-thick metallic strip on a Si substrate that is placed underneath the sample. The calibration wire was designed to be wider than the sample width to produce a uniform in-plane magnetic field. A current of 700 mA was passed through the calibration wire, which induces a magnetic field of 2.10 Oe calculated by Biot-Savart Law. By taking the linear regression shown in the insets, the corresponding FL field of the black squares data can be determined

that Pt and Ta, respectively, produced h_{FL_Pt} = 1.56 Oe and h_{FL_Ta} = 0.71 Oe, which lead to β_{Pt_FL}= 2.6 nm in 3Py/3Pt and β_{Ta_FL}= 2.7 nm in 3Ta/3CoFeB, respectively.

4.4 Measuring SOT Effective Fields Using Time-resolved MOKE

We now move beyond the study of SOTs in the quasi-static regime to investigate the SOT-induced magnetization dynamics in the time domain. We perform TR MOKE measurements on Py/Pt and Ta/CoFeB samples. The principle of TRMOKE measurements has been discussed in Section 2.6.2. The pulse generator drives the magnetization dynamics with 2 V voltage pulses, corresponding to j_{Pt}=2.39×10^{10} A/m^2 and j_{Ta} =1.20×10^{10} A/m^2, respectively, in the Pt and Ta layers of the two samples.

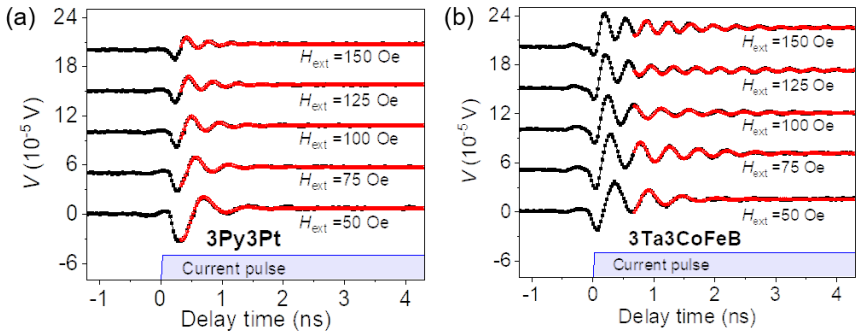

Figure 4.5 (a) and (b) The dependence of the measured TRMOKE signal on the delay time for 3Py/3Pt and 3Ta/3CoFeB, respectively. The blue area represents the duration of the current pulse. Measured signal (black squares) at different external magnetic fields from 50 Oe to 150 Oe are offset for clarity. The red curves that overlap the black data points are fit to the experimental data with the formula $\sin(2\pi f_0 t+\varphi)\cdot\exp(-t/t_\alpha)$.

The induced θ_{KR} as a function of delay time Δt for the 3Py/3Pt and 3Ta/3CoFeB samples from H_{ext} = 50 Oe to 150 Oe are shown in Figure 4.5 (a) and (b).

The start of the current pulse, schematically depicted by the blue bar at the bottom of Figure 4.5 (a) and (b), defines $\Delta t = 0$, i.e. when the optical probe pulse arrives simultaneously with the rising edge of the current pulse. In response to the current pulse, m_z, which is proportional to the measured voltage (y-axis), undergoes a fast oscillation that decays to a new equilibrium value that depends on both the external magnetic field and the current amplitude. A Fast Fourier Transform (FFT) of the oscillation data (not shown) confirms that there is a single precession frequency. We therefore fit the decaying oscillations with the formula $\sin(2\pi f_0 t+\varphi)\cdot\exp(-t/t_\alpha)$, where f_0 is the oscillation frequency, φ is the phase of the magnetization precession and t_α is the exponential decay time [24]. In Figure 4.6 (a), the oscillation frequencies extracted via fits to this functional form (solid data points) are plotted as a function of the applied magnetic field, together with the ferromagnetic resonant frequency (open data points) measured with an FMR spectrometer. We note that the precession frequencies obtained via this fit are in good agreement with those obtained by FFT. The red curve is a fit to the FMR data using the Kittle equation. We find that the dispersion relation extracted from the TR MOKE measurements agrees well with an extension of the FMR fit, indicating that in TR MOKE measurement the magnetization is precessing at FMR frequency. From the fitting curves, the extracted effective magnetizations are $M_{eff\_Py} = 760$ emu/cm^3 and $M_{eff\_CoFeB} = 960$ emu/cm^3, while the effective anisotropic fields are $H_{a\_Py} = 31$ Oe and $H_{a\_CoFeB} = 40$ Oe. The damping of oscillatory TRMOKE signal at each applied field can be calculated using the relationship $\alpha = 1/t_\alpha\gamma(M_s/2 + H)$ for in-plane magnetization in our samples [19]. The calculated data is plotted in Figure 4.6 (b) and fit by the red curves using the widely applied exponential relation $\alpha(H_{ext}) = \alpha_1\exp(-H_{ext}/H_0) + \alpha_0$, where α_1 is the coefficient, H_0 is a constant, and α_0 is

the effective damping [25]. The effective damping in 3Py/3Pt and 3Ta/3CoFeB samples were found to be 0.024 and 0.008, respectively. They are very close to the damping values $\alpha_{Py/Pt} = 0.022$ and $\alpha_{Ta/CoFeB} = 0.009$ extracted from FMR measurements as shown in the inset of Figure 4.6 (b). This result indicates the SOT induced magnetization oscillation alternatively can be used to measure effective damping in FM/HM bilayer even at low magnetic field range, while the traditional FMR measurements typically need to apply a high magnetic field to saturate the film sample in case of the multi domains.

To fully understand the oscillation spectra, we performed micromagnetic simulations using Object Oriented Micromagnetic Framework (OOMMF) software from NIST [26]. A general simulation script has been attached in Appendix D). We defined the sample size in our simulation to be the same as the real sample size (20 μm(x) × 250 μm(y) × 3 nm(z)) used in the experiment with the mesh size of 100 nm(x) × 100 nm(y) × 1 nm(z). The LLG equation was numerically solved using the Oxs_SpinXferEvolve module where both DL and FL terms are included. The constant external magnetic field was applied in the x direction. In the simulation, we used the values of magnetization, anisotropic field, and damping determined from the fits to experimental oscillatory polar MOKE signal. The initial magnetization in our simulation was defined along the x axis while the effective anisotropic field was set along the y axis because even a minimal magnetic field (50 Oe) is strong enough to initialize the magnetization direction [see Figure 4.2(c) and (d)]. The computation includes a single current pulse of 6.6 ns duration starting at $t = 0$ ns with 50 ps rising and falling edges, identical to the pulse shape applied in the TR MOKE experiment. The intensity of the current pulse was assigned with the same value as the calculated

current density in HM from the experiment. Moreover, a uniform in-plane Oersted field along the *y* axis (h_{Oe_Py} = 0.45 Oe and h_{Oe_CoFeB} = −0.22 Oe, which are pulse current induced Oersted fields evaluated by the currents flowing through HM metal layer via Ampere's law) was also included in our simulation. The out-of-plane Oersted field was neglected because the laser spot (2 μm in diameter) was focused on the sample center position. The spin Hall angles used in our simulation were extracted from the DC MOKE experiment. Both spin polarization vectors σ_{Py} and σ_{CoFeB} were set in the positive *y* direction in view of the opposite spin Hall angle signs between the Pt and Ta layers which were, respectively, deposited on the top of the Py and the bottom of the CoFeB layers.

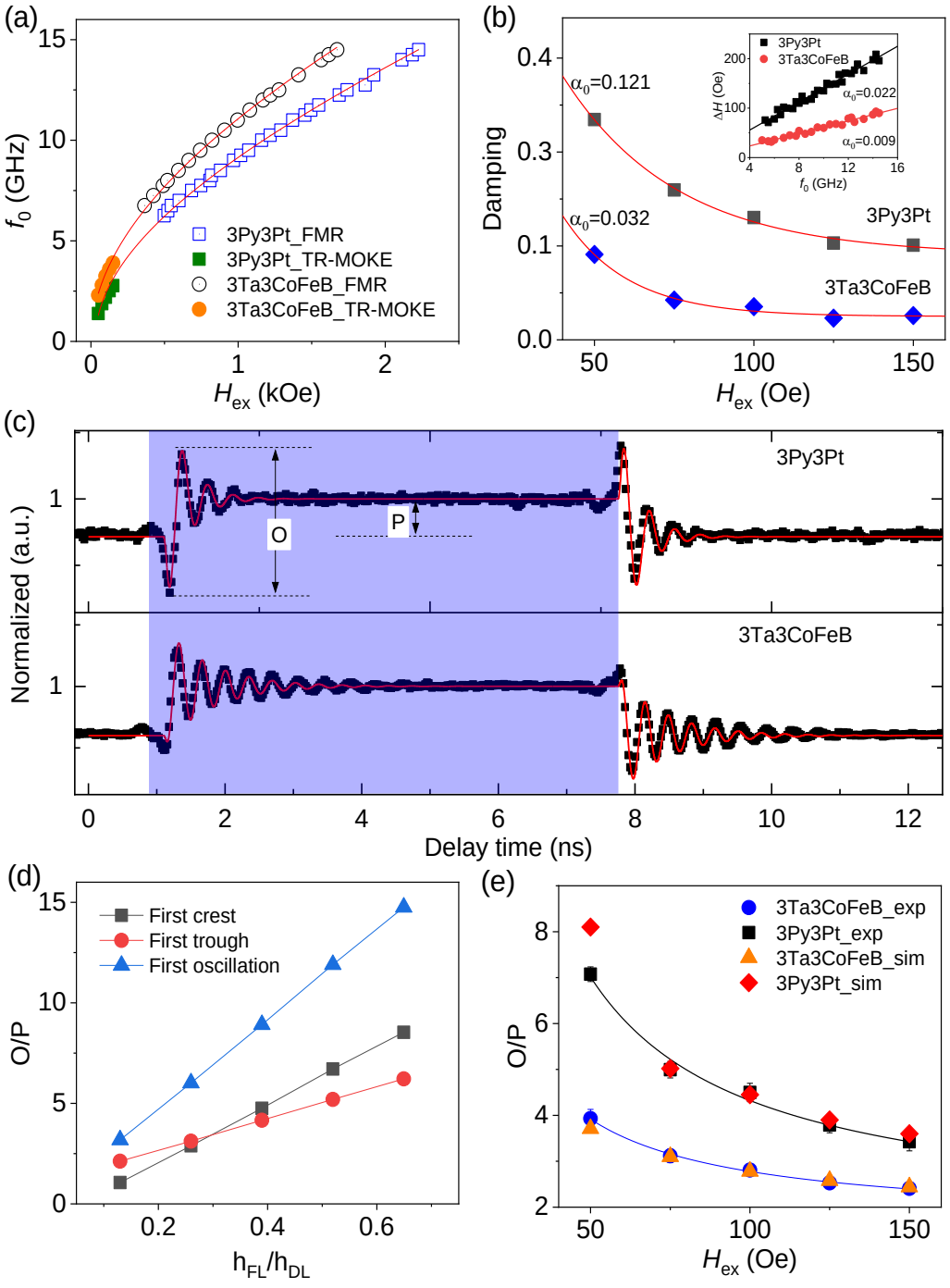
(a)
f_0 (GHz)
H_{ex} (kOe)
3Py3Pt_FMR
3Py3Pt_TR-MOKE
3Ta3CoFeB_FMR
3Ta3CoFeB_TR-MOKE
(b)
Damping
H_{ex} (Oe)
α_0=0.121
α_0=0.032
3Py3Pt
3Ta3CoFeB
ΔH (Oe)
f_0 (GHz)
α_0=0.022
α_0=0.009
(c)
Normalized (a.u.)
O
P
3Py3Pt
3Ta3CoFeB
Delay time (ns)
(d)
O/P
h_{FL}/h_{DL}
First crest
First trough
First oscillation
(e)
O/P
H_{ex} (Oe)
3Ta3CoFeB_exp
3Py3Pt_exp
3Ta3CoFeB_sim
3Py3Pt_sim

Figure 4.6 (a) The oscillation frequencies extracted from TRMOKE measurements (solid data points) and resonant frequencies from FMR measurements (open data points) as a function of H_{ext} for 3Py/3Pt and 3Ta/3CoFeB samples. The red curves are a fit using the Kittle equation. (b) The damping extracted from the TRMOKE data as a function of the applied field. The inset is the linear fit of the FMR linewidth as a function of the frequency using equation $\Delta H = 4\pi f\alpha/\gamma$. (c) Measured TRMOKE response to a current pulse applied over the time window indicated by the blue shaded area for the 3Py/3Pt (top panel) and 3Ta3CoFeB (bottom panel) samples. The solid black squares are experimental data that are fitted (red curves) using micromagnetic OOMMF software. The intensities of the first oscillation cycle and the plateau, i.e. "O" and "P", are indicated by arrows. (d) The extracted ratio *O/P* as a function of the ratio of h_{FL}/h_{DL} in the simulated Py/Pt system at H_{ext}=150 Oe. (e) The dependence of *O/P* on the external magnetic field in 3Py/3Pt and 3Ta/3CoFeB samples. The black squares and blue spheres represent experimental results. Up and down triangles refer to simulation results. The experimental data were fit using $a/H + b$, where a = 269.5, b = 1.6 for 3Py/3Pt and a = 113.9, b = 1.6 for 3Ta/3CoFeB.

In our simulation, we at first characterized how the two SOTs affect the oscillation behavior of the magnetization as shown in Figure 4.7. By increasing the prefactor ε' of FL torque from 0.1 to 0.3, we found the magnitude of the oscillation (*O*) is increasing with ε' while the plateau (*P*) is independent on ε'. On the other hand, when we increase the ε from 0.05 to 0.15, the *O* does not change obviously with the DL torque prefactor ε but P is proportional to ε. Those results also illustrate the previously mentioned statement that the $\boldsymbol{h}_{DL}$ induces the rotation of magnetization and $\boldsymbol{h}_{FL}$ assists/triggers the precession of magnetization. In this evolver, DL coefficient $\varepsilon = \theta_{SH}/2$, is the half of the spin Hall angle of the HM material, which determines the stable position of the magnetization (in this case, the m_z) induced by current pulse. In the meanwhile, FL coefficient ε' determines the amplitude of the oscillations. Therefore, we can fit the experimentally measured oscillatory curve by tuning ε'

where ε is determined from the Hall angle of the FM material and damping factor is measured from FMR measurements.

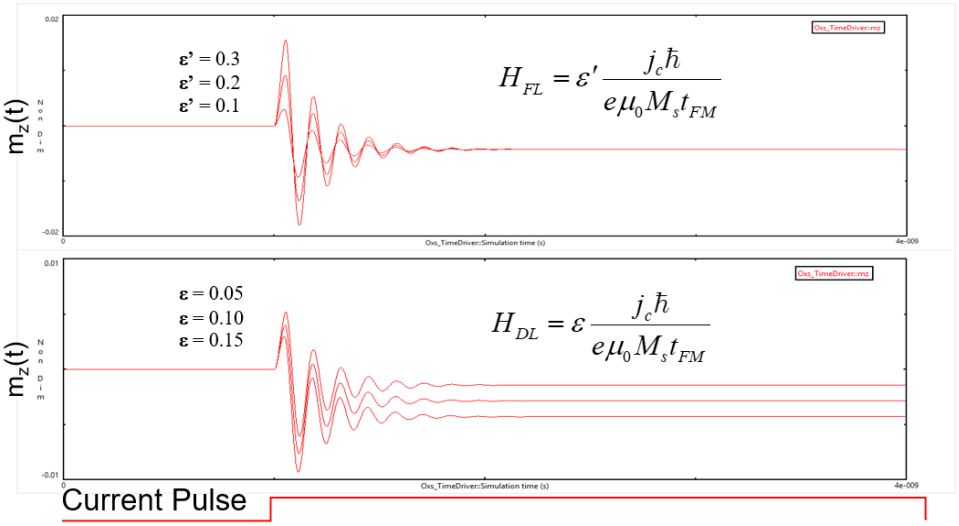

Figure 4.7 Simulation results about the impacts of $\boldsymbol{h}_{DL}$ and $\boldsymbol{h}_{FL}$ fields on the oscillation behaviors of the $m_z(t)$ component. A higher ε' gives rise to a larger oscillation amplitude in the first cycle and a higher ε results in a bigger plateau indicating the stable position of m_z in presence of the pulse.

The fit results obtained from the OOMF simulations (red curves) are shown in Figure 4.6 (c) and match the experimental results very well. This indicates that both $\boldsymbol{T}_{FL}$ and $\boldsymbol{T}_{DL}$ do not change at high frequency. Using the OOMF simulations, we examine the dependence of the plateau value (P in Figure 4.6 (c)) on the value of h_{DL} and h_{FL}. The results (not shown) reveal that P (and thus Δm) depends only on h_{DL} and not on h_{FL}. Therefore, h_{DL} can be extracted from TR MOKE just like the DC case. The extracted values are $h_{DL\_Py/Pt} = 2.62$ Oe and $h_{DL\_Ta/CoFeB} = 1.40$ Oe. With current densities of $j_{Pt} = 2.39\times10^{10}$ A/m^2 and $j_{Ta} = 1.20\times10^{10}$ A/m^2, we obtain SOT efficiencies of the DL terms of $\beta = 8.8$ nm and $\beta = -10.2$ nm for the 3Py3Pt and 3Ta/3CoFeB

samples, respectively, which are very close to the values in the DC case (β = 8.9 nm in 3Py3Pt and β = −10.6 nm in 3Ta/3CoFeB). Through the simulation studies, we also find that the ratio *O/P* (*O* strands for the oscillation amplitude in the first cycle) depends linearly on the ratio of h_{FL}/h_{DL} , as shown in Figure 4.6 (d).

It is noted that in our simulation the *O/P* ratio is almost independent on the mesh size even when we reduce the mesh size to 10 nm × 10 nm, which is smaller than the exchange length. It turns out that the change on *O/P* ratio is less than 1% when one changes the cell size from 10 nm × 10 nm to 100 nm ×100 nm. We find that this linear relationship holds whether *O* is defined as the amplitude of the first trough (red points) or crest (black points). The same result is found in the Ta/CoFeB system but is not shown. With this information, the best fit to the oscillation patterns could be quickly determined by changing h_{FL} to match the *O/P* ratio, leading to the determination of $h_{FL\_Py/Pt}$ = 0.72 Oe and $h_{FL\_Ta/CoFeB}$ = 0.30 Oe.For the Py/Pt system. The ratio of $(h_{FL}/h_{DL})_{\_Py/Pt}$ = 0.28 is in good agreement with the ratio of 0.29 determined from the DC MOKE measurement. For the Ta/CoFeB system, the ratio of $(h_{FL}/h_{DL})_{\_Ta/CoFeB}$ = 0.22 is smaller than the value of 0.26 extracted from the DC MOKE measurement. There are two possible reasons for this discrepancy. First, there is strong interface intermixing at the Ta/CoFeB interface. This has been observed in a few previous experiments and interpreted using a drift-diffusion model[27,28]. This effect may contribute to the SOTs in a manner not captured by our simulation. Second, because current-induced $h_{Oe//}$ partially cancels the h_{FL} due to the layer sequence, the measured magnitude of the oscillation is weak compared with the plateau value seen in Figure 4.6 (c). In this case, even a small deviation in h_{FL} would cause a large error on calculation of h_{FL}/h_{DL}.

In addition to the linear relationship between the *O/P* and h_{FL}/h_{DL} ratios, we also found the ratio *O/P* is inversely proportional to H_{ext}, as shown in Figure 4.6 (e). We demonstrate that *O/P* is inversely proportional to H_{ext} by showing that the experimental data are well fit by a function of form $a/H+b$ with b values very close to zero. The fit value for coefficient a is loosely related to the Oersted field. The inverse proportionality between the ratio *O/P* and H_{ext} is also found in our simulation results, which show excellent agreement with the experimental data. We note that the plateau (*P*) is independent of H_{ext}. Therefore, the first oscillation amplitude *O* follows the $1/H_{ext}$ dependence, having the same dependence as $m_y(H_{ext})$ [see Figure 4.4 (a) and (b)]. This suggests that the initial oscillation in m_z tends to follow m_y and is then suppressed by the large demagnetization field H_D, ultimately reaching a final state with a *P* value that is independent of H_{ext} because H_{ext} is negligible compared with H_D.

4.5 Summary

In summary, we use TRMOKE to measure the magnetization dynamics induced by SOTs in two ferromagnetic heterostructures, 3Py/3Pt and 3Ta/3CoFeB. We show that the SOT effective fields h_{DL} can be extracted from the plateau value (*P*) and h_{FL} can be extracted from fitting the TRMOKE spectrum by varying h_{FL} to match the *O/P* ratio. The extracted effective fields and their efficiencies are in good agreement with those extracted from DCMOKE measurements, indicating that the effective fields do not change at high frequency. These studies provide insight into how h_{FL} and h_{DL} affect the magnetization dynamics. The method to extract h_{FL} and h_{DL} from TRMOKE data may be extendable to other HM/FM bilayer systems.

REFERENCES

[1] S. Zhang, P. Levy, and A. Fert,"*Mechanisms of spin-polarized current-driven magnetization switching*", Physical review letters **88**, 236601 (2002).

[2] J. Slonczewski,"*Currents and torques in metallic magnetic multilayers*", Journal of magnetism and magnetic materials **247**, 324 (2002).

[3] J. Yoon, S.-W. Lee, J. H. Kwon, J. M. Lee, J. Son, X. Qiu, K.-J. Lee, and H. Yang,"*Anomalous spin-orbit torque switching due to field-like torque–assisted domain wall reflection*", Science advances **3**, e1603099 (2017).

[4] M.-H. Nguyen, D. Ralph, and R. Buhrman,"*Spin torque study of the spin Hall conductivity and spin diffusion length in platinum thin films with varying resistivity*", Physical review letters **116**, 126601 (2016).

[5] W. Legrand, R. Ramaswamy, R. Mishra, and H. Yang,"*Coherent subnanosecond switching of perpendicular magnetization by the fieldlike spin-orbit torque without an external magnetic field*", Physical Review Applied **3**, 064012 (2015).

[6] J. M. Lee *et al.*,"*Oscillatory spin-orbit torque switching induced by field-like torques*", Communications Physics **1**, 1 (2018).

[7] N. Perez, E. Martinez, L. Torres, S.-H. Woo, S. Emori, and G. Beach,"*Chiral magnetization textures stabilized by the Dzyaloshinskii-Moriya interaction during spin-orbit torque switching*", Applied Physics Letters **104**, 092403 (2014).

[8] G. Finocchio, M. Carpentieri, E. Martinez, and B. Azzerboni,"*Switching of a single ferromagnetic layer driven by spin Hall effect*", Applied Physics Letters **102**, 212410 (2013).

[9] O. Lee, L. Liu, C. Pai, Y. Li, H. Tseng, P. Gowtham, J. Park, D. Ralph, and R. Buhrman,"*Central role of domain wall depinning for perpendicular magnetization switching driven by spin torque from the spin Hall effect*", Physical Review B **89**, 024418 (2014).

[10] C. O. Avci, K. Garello, M. Gabureac, A. Ghosh, A. Fuhrer, S. F. Alvarado, and P. Gambardella,"*Interplay of spin-orbit torque and thermoelectric effects in ferromagnet/normal-metal bilayers*", Physical Review B **90**, 224427 (2014).

[11] C. O. Avci, A. Quindeau, C.-F. Pai, M. Mann, L. Caretta, A. S. Tang, M. C. Onbasli, C. A. Ross, and G. S. Beach,"*Current-induced switching in a magnetic insulator*", Nature materials **16**, 309 (2017).

[12] K. Garello *et al.*,"*Symmetry and magnitude of spin–orbit torques in ferromagnetic heterostructures*", Nature nanotechnology **8**, 587 (2013).

[13] P. Li *et al.*,"*Spin–orbit torque-assisted switching in magnetic insulator thin films with perpendicular magnetic anisotropy*", Nature communications **7**, 1 (2016).

[14] X. Fan, A. R. Mellnik, W. Wang, N. Reynolds, T. Wang, H. Celik, V. O. Lorenz, D. C. Ralph, and J. Q. Xiao,"*All-optical vector measurement of spin-orbit-induced torques using both polar and quadratic magneto-optic Kerr effects*", Applied Physics Letters **109**, 122406 (2016).

[15] H. Celik *et al.*,"*Vector-Resolved Magnetooptic Kerr Effect Measurements of Spin–Orbit Torque*", IEEE Transactions on Magnetics **55**, 1 (2018).

[16] M. Baumgartner *et al.*,"*Spatially and time-resolved magnetization dynamics driven by spin–orbit torques*", Nature nanotechnology **12**, 980 (2017).

[17] H. Shibata, M. Okano, and S. Watanabe,"*Ultrafast control of coherent spin precession in ferromagnetic thin films via thermal spin excitation processes induced by two-pulse laser excitation*", Physical Review B **97**, 014438 (2018).

[18] H. Chen, X. Fan, W. Wang, H. Zhou, Y. Gui, C.-M. Hu, and D. Xue,"*Electric detection of the thickness dependent damping in Co90Zr10 thin films*", Applied Physics Letters **102**, 202410 (2013).

[19] J. Walowski, M. D. Kaufmann, B. Lenk, C. Hamann, J. McCord, and M. Münzenberg,"*Intrinsic and non-local Gilbert damping in polycrystalline nickel studied by Ti: sapphire laser fs spectroscopy*", Journal of Physics D: Applied Physics **41**, 164016 (2008).

[20] J. Sinova, S. O. Valenzuela, J. Wunderlich, C. Back, and T. Jungwirth,"*Spin hall effects*", Reviews of Modern Physics **87**, 1213 (2015).

[21] A. M. Humphries, T. Wang, E. R. Edwards, S. R. Allen, J. M. Shaw, H. T. Nembach, J. Q. Xiao, T. J. Silva, and X. Fan,"*Observation of spin-orbit effects with spin rotation symmetry*", Nature communications **8**, 1 (2017).

[22] E. Saitoh, M. Ueda, H. Miyajima, and G. Tatara,"*Conversion of spin current into charge current at room temperature: Inverse spin-Hall effect*", Applied physics letters **88**, 182509 (2006).

[23] X. Fan, J. Wu, Y. Chen, M. J. Jerry, H. Zhang, and J. Q. Xiao,"*Observation of the nonlocal spin-orbital effective field*", Nature communications **4**, 1 (2013).

[24] W. Hiebert, A. Stankiewicz, and M. Freeman,"*Direct observation of magnetic relaxation in a small permalloy disk by time-resolved scanning Kerr microscopy*", Physical Review Letters **79**, 1134 (1997).

[25] M. Tang, W. Li, Y. Ren, Z. Zhang, S. Lou, and Q. Jin,"*Magnetic damping and perpendicular magnetic anisotropy in Pd-buffered [Co/Ni] 5 and [Ni/Co] 5 multilayers*", RSC advances **7**, 5315 (2017).

[26] M. J. Donahue and M. Donahue, *OOMMF user's guide, version 1.0* (US Department of Commerce, National Institute of Standards and Technology, 1999).

[27] J. Torrejon, J. Kim, J. Sinha, and M. Hayashi, in *Spin* (World Scientific, 2016), p. 1640002.

[28] M. Cecot *et al.*,"*Influence of intermixing at the Ta/CoFeB interface on spin Hall angle in Ta/CoFeB/MgO heterostructures*", Scientific reports **7**, 1 (2017).

Chapter 5

MAGNETOELECTRIC DEVICE FABRICATIONS

5.1 Motivation

In an magnetoelectric (ME) material, an electric field **E** induces a magnetic moment $\mathbf{M}=\alpha_{ME}\mathbf{E}$, where α_{ME} is the tensor of ME susceptibility. Magnetoelectric (ME) properties were predicted by Curie in 1894 [1] and latter experimentally demonstrated by Debye [2]. The expression of ME effect can be obtained from the expansion of the free energy with respect to the electrical field **E** and magnetic field **H**, respectively [3]:

$$F(E,H) = F_0 - P_{si}E_i - M_{si}H_i - \frac{1}{2}\varepsilon_{ij}E_iE_j - \frac{1}{2}\mu_{ij}H_iH_j - \alpha_{ij}E_iH_j - \ldots, \qquad (5.1)$$

Here, we only keep the lower-order terms in Eq (5.1).

$$\begin{aligned} P_i(E,H) &= -\frac{\partial F}{\partial E_i} \\ &= P_{si} + \varepsilon_{ij}E_j + \alpha_{ij}H_j + \ldots \end{aligned}, \qquad (5.2)$$

$$\begin{aligned} M_i(E,H) &= -\frac{\partial F}{\partial H_i} \\ &= M_{si} + \mu_{ij}H_j + \alpha_{ij}E_j + \ldots \end{aligned}, \qquad (5.3)$$

where P_{si} and M_{si} denote the spontaneous polarization and magnetization, ε_{ij} and μ_{ij} are the electric and magnetic susceptibilities. The tensor $\alpha_{ij}=\alpha_{ME}$ is the induced polarization in P_i by a magnetic field or the induced magnetization in M_i by an electrical field. Therefore, the third term in both Eq (5.2) and (5.3) are from the contribution of magnetoelectric coupling. As a result, the applied *E* field can induce additional magnetization while the *H* field can also induce additional polarization in a

ME material. ME response is only allowed in materials that break the time-reverse symmetry and spatial inversion symmetry [4]. Such violation of time-reversal symmetry can extrinsically occur through the application of an external magnetic field or intrinsically in the form of long-range magnetic ordering. Breaking time and spatial inversion symmetry can be realized by magnetic order and electric polarization, respectively.

Evidence of ME properties has also been reported in the materials including $GaFeO_3$, $Ni_3B_7O_{13}I$, $LiMnPO_4$ or $Y_3Fe_5O_{12}$ [5]. However, the ME effect had not received enough attention at the beginning since the effect is very small. This includes the antiferromagnetic Cr_2O_3, on which the spintronic devices discussed in this Chapter is based on. Dzyaloshinskii showed the violation of time-reversal symmetry in Cr_2O_3 in 1960 [6], and the inherited ME effect was soon confirmed experimentally in 1961 [7]. Only until very recently after researches demonstrated the simultaneous application of electric and magnetic field can switch the Neel vector in Cr_2O_3, which in turn can switch the magnetization of a neighboring FM layer [8], the researches focus ME devices have blossomed since it can potentially cost little energy to switch the magnetization.

In the simplest microscopic description of ME compound Cr_2O_3, the application of the electric field shifts the Cr^{3+} ions on different sublattices to non-equivalent positions where the Cr^{3+} ions experience distinct strength of the crystal field. As a result, this electric field changes the single ion anisotropy and modifies the exchange integrals between the ions [9]. As a result, a perpendicular magnetic anisotropy is induced in Cr_2O_3 with α_{zz}= 4.13 ps m^{-1}[10]. Typically, this *E* field is applied via a biased DC voltage and this induced anisotropy is named voltage

controlled magnetic anisotropy (VCMA). This ME induced magnetic moment remains small. For example, if a typical electric field with the order of 10^5 Vm^{-1} is applied on a millimetre-sized Cr_2O_3 sample, the magnetic moment is only of the order of 10^{-5} μ_B per Cr atom. However, if the *E* field goes to 10^9 Vm^{-1} that is the dielectric breakdown values of Cr_2O_3, the magnetic moment can be enhanced to several percent of μ_B per Cr atom. Such an electrical property can be literarily achieved in thin film of Cr_2O_3 with a small bias.

Since the ME induced magnetic moment is tiny, the measurement had to be conducted in a complex detection apparatus as discussed in reference [7]. However, if an ME layer is adjacent to a FM layer, the tiny magnetization can significantly exchange coupled with FM. Thus, one can characterize the switching of the induced moment in ME layer via its exchange coupling to other magnets [11].

5.2 ME Device Introduction

While there is no net magnetization in the interior of Cr_2O_3, there is net magnetization at the surface where spin compensation cannot be completed. The surface magnetization can be switched as the Neel vectors in Cr_2O_3 are isothermally switched by the electric field (or voltage bias). This can cause the magnetization of a neighboring FM to switch due to the exchange coupling. Such a switching causes little energy compared with SOT-driven switching. In this Chapter, we discuss the project of developing a spintronic memory based on this phenomenon.

5.2.1 Description of ME-based Memory Devices

The proposed memory cell is shown in Figure 5.1 consisting of ME AFM (Cr_2O_3) and a magnetic tunnel junction (MTJ) made of two FM layers separated by an

insulator barrier. The operation principle is we write information via a bias applied cross the ME AFM that switch its surface magnetization and it in turn switch the magnetization of the bottom FM layer. The switching of the magnetization of the bottom FM layer can be read out via magneto-tunnel-resistance that depends on the relative orientation of the magnetizations in two FM layers, being low when they are parallel and high when they are antiparallel. The ME layer of Cr_2O_3 samples were prepared by our collaborator Prof. Christian Binek at the University of Nebraska at Lincoln [8]. The perpendicular MTJs have the basic structure of $[Co/Pd]_n$/Ta/CoFeB(x)/ MgO(y)/ CoFeB(z)/Ta (x, y and x are the thicknesses in nanometers), where CoFeB(z)/Ta is the top FM layer (top electrode), MgO(y) is the tunneling barrier and $[Co/Pd]_n$/Ta/CoFeB(x) is the bottom FM layer (bottom electrode). Here, the [Co/Pd] multilayer is used to establish the perpendicular magnetic anisotropy (PMA) which is coupled to the upper CoFeB through the Ta layer. The PMA in CoFeB layer can be achieved by tuning the thickness of CoFeB and the adjacent Ta layers. The Ta is a necessary buffer layer for the upper CoFeB to promote the PMA. The whole MTJ stacks are grown on top of a 100 nm Cr_2O_3 samples and patterned into Hall bar shape for electrical measurement.

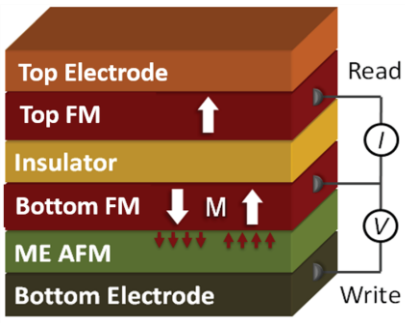

Figure 5.1 Proposed magnetic memory cell based on ME device.

The schematic of our ME device is shown in Figure 5.2(a) and the real pattern design has been attached in Appendix E. We implement two methods to read out the switching of the bottom FM layer in MTJ: (1) anomalous Hall effect (AHE) via a Hall bar structure, and (2) magnetoresistance via MTJ. The 800 nm-width Hall bar structure was patterned by etching down the MTJ stack (blue) to reach the bottom FM layer. The etching has to be very precise since the bottom FM layer is less than 10 nm. The 4 terminals of the Hall bar are marked as yellow on top of Ru layer, which also serve as bias contact for bottom Cr_2O_3. On top of this Hall bar, a MTJ is patterned so that the MTJ is embedded in SiO_2 (Gray) and a top window is opened to connect the top FM layer with an Au contact (yellow pad at the center). Therefore, in one device we can measure either AHE of bottom free layer using the four bottom electrodes or the TMR of the MTJ between the top electrode and one of the bottom electrodes. By passing a dc current along the longitudinal direction of the Hall bar, AHE signal is detected from the induced transverse voltage. On the other side, TMR voltage can be measured between top and bottom electrodes by injecting a DC current through the MTJ stacks. We conduct those two measurements on a probe station where an external magnetic field with maximum of 500 Oe is applied perpendicularly. In order to have the VCMA excitation, one must apply an electric bias on Cr_2O_3 film. There is a 10 nm conducting V_2O_3 film (brown) deposited prior to the growth of Cr_2O_3 film. A bias voltage then can be applied on Cr_2O_3 film through one of the bottom electrodes and V_2O_3 film as shown in Figure 5.2(a).

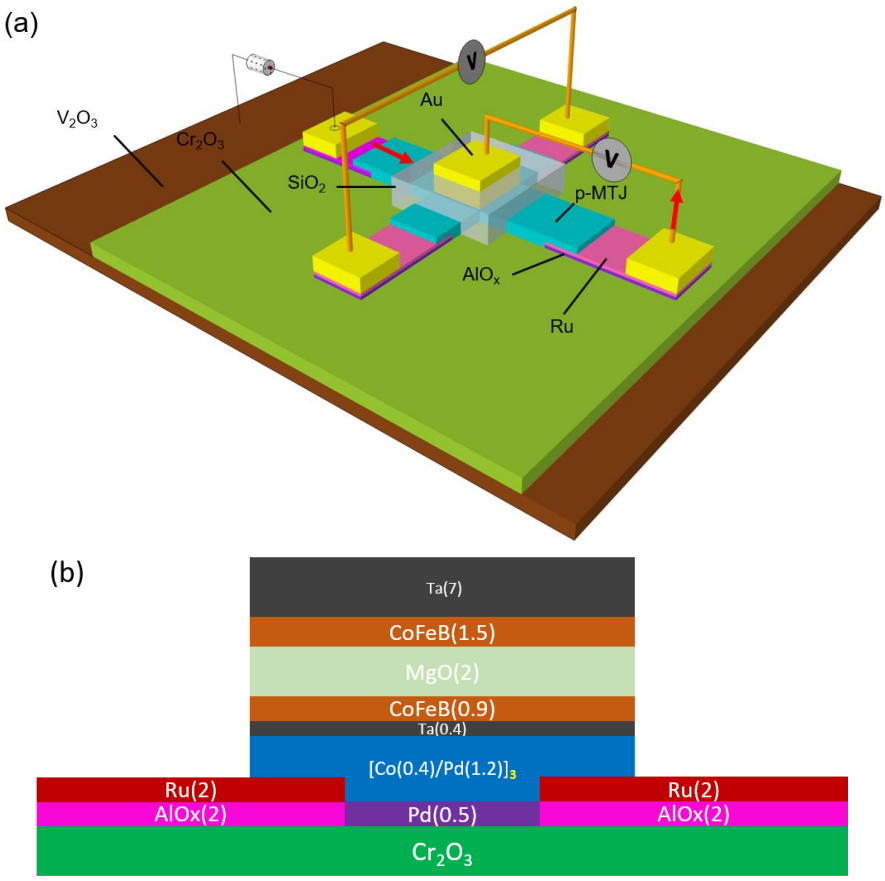

Figure 5.2 (a) Schematic of integrated ME memory device and the illustration of electrical measurement on this ME device. (b) Stacks of MTJs and bottom contact pads. The numbers in the parenthesis are in unit of nano meters.

5.2.2 Structure Design

The biggest challenge in fabricating this ME device is to properly connect the terminals of small Hall bar to their corresponding big contact pads. First, we cannot simply grow the contact pads directly on Cr_2O_3 film since the large contact pads increases the number of pin holes in Cr_2O_3 film, causing a large leaking current and making bias cross the Cr_2O_3 film impossible. Our collaborators, Prof. Joathan Bird and Uttam Singisetti groups at University of Buffalo, have conducted leakage studies on

Cr_2O_3 film. They have demonstrated that, for sufficiently small contact sizes (50 μm), a high resistance values could be achieved as much as GΩ. Such contacts should be suitable for investigations of voltage-induced magneto-electric switching. In this regard, the size of our Hall bar (width: length ≈ 0.8 μm: 30 μm) is small enough to prevent the leakage problem. However, it is impracticable to shrink the size of electrical contact pad to this size for later electrical measurement on a probe station. Typically, contact pad has a size of 300 μm × 300 μm. To meet all those requirements, we need to isolate the big contact pads and simultaneously keep the good connection to the terminals of the Hall bar as shown in the real design in Appendix E (a).

Isolating the contact from Cr_2O_3 film requires an insulator layer underneath the contact pads, which means we must grow the "insulator layer/contact pads" structure prior to depositing the Hall bar. We first grow Al_2O_3/contact and open a window to access Cr_2O_3 as illustrated in Figure 5.2 (b). In addition, this contact layer cannot be too thick. Otherwise, the bottom FM stack, which is less than 10 nm thick, cannot make a good contact with a thick contact pad. This makes a normal contact typically made of 10 nm Ti/100 nm Au unpractical in this device design. To solve this problem, we replace the thick Ti/Au layers with a very thin metallic layer Ru (2 nm) (red layer). This layer was extended out, on which thick Ti/Au contact pads can be made. There are two advantages of using Ru layer: 1) RuO is also conducting [12] so Ru layer can be exposed for processing, and (2) thin Ru layer is very smooth. The atomic force microscopy (AFM) measurement on 2 nm Ru layer shows a very small roughness of 0.14 nm as shown in Figure 5.3 (a).

The fabrication of the top contact pad presents another challenge. The fabrication requires the isolation of this top contact from all contacts to the middle

layer, i.e., bottom FM layer. We added an insulator layer (a 40 nm SiO_2) as shown in Appendix E (b). In addition, we also need to leave a small opening in insulator layer to contact the top electrode of the MTJ. We used a cross opening opened exactly on top of the Hall bar. This cross opening must be smaller than the width of the Hall bar, which is 0.8 μm.

5.3 Challenges in Fabrication

5.3.1 Leakage Test Through Contact Pad

Leakage, as discussed above, is a major roadblock to successfully fabricate the ME devices. We have to anticipate the possible electrical leakage in each fabrication step. For example, the leakage from big contact pad is very possible and it can be avoided by inserting a thin insulator underneath the contact pad. The AlO_x fabricated via reactive sputtering in a magneto sputtering system, is employed to isolate the contact pads from Cr_2O_3 film. To test the insulating property of the AlO_x layer, we have tested the I-V behavior in an (200 nm)Au/ (2 nm)AlO_x/(200 nm)Au pillar structure with a diameter of 250 μm, and the result is shown in Figure 5.3 (b). The I-V curve displays a very good insulating behavior such that the 2nm AlO_x can be used as insulator in our device.

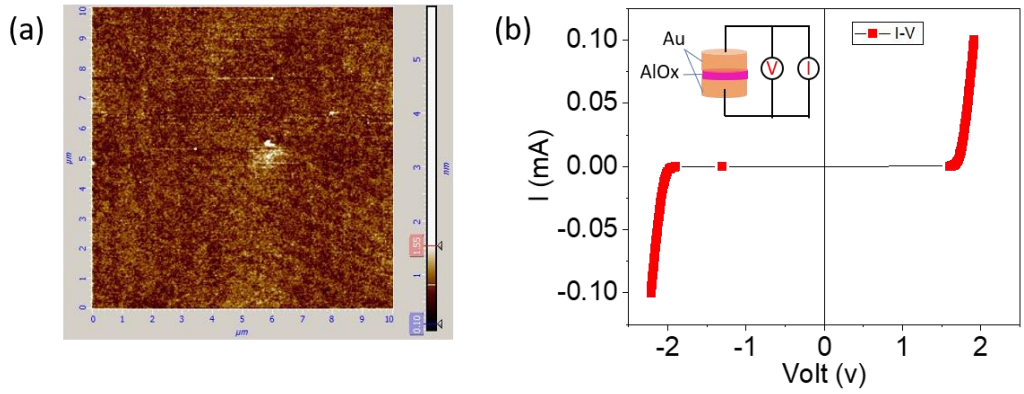

Figure 5.3 (a) The AFM picture of 2 nm Ru layer grown on Si wafer. (b) The I-V curve of 2 nm AlO_x thin film grown on top of a 100 nm Au layer.

5.3.2 Formation of Undercut Profile in Small Feature

Lift-off process has been widely used in patterning small-dimension features for microelectronics. In Section 2.4.2, we have introduced the basic lithography procedures of lift-off technique. When one uses a photoresist (PR) for lift-off removal, it is important to form an undercut profile in the sidewall of the resist. This profile will prevent deposited film from contacting the side wall of PR so that a subsequent removal of PR will not remove or damage the film. If the sidewall profile has a volcano-shaped profile as sketched in Figure 5.4 (b), lift-off can be very difficult. An under-cut sidewall as shown in Figure 5.4 (a) will solve the problem. The best solution is to further expand the under-cut space using bilayer PRs as shown in Figure 5.4 (c) where the two PRs are developed separately after the laser writing or e-beam writing.

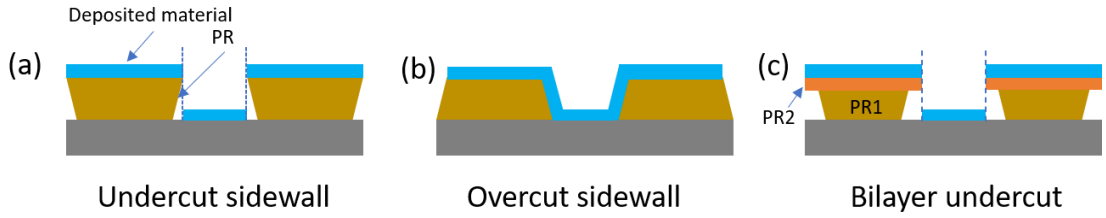

Figure 5.4 Comparison of a) undercut sidewall profile, b) overcut sidewall profile and c) bilayer undercut profile.

The selection of the two PRs depends on the exposure light sources and the writing resolution. In maskless microlithography, we typically use the positive PRs LOR5A/AZ-MIR701 or LOR5A/AZ-1512 for laser writing. It is noted that the thickness of each layer is determined by the spin rate of the PR coating. In addition, the size of the undercut profile is up to the development time in the developer (AZ-MIF-300). Since the bottom layer LOR has a faster etching rate than that of the upper PR layer, the undercut profile always shows the feature as depicted in Figure 5.4 (c). When the pattern feature scales to sub-micro or nano meters, EBL should be employed and the corresponding PRs we used are LOR3A(150 nm)/CSAR(70 nm). We apply two-steps development after the e-beam writing as shown in Figure 5.5. First, developer AR600-546 is used to remove the exposed CSAR resist such that unexposed area is left after the developing. Secondly, the developer AZ-MIF-300K-47 can isotopically etch the LOR3A no matter they are e-beam exposed or unexposed as drawn in Figure 5.5 (c). The etching is selective in each developing step, which means developer only targets the corresponding PR and has nothing to do with the others. If the development time is not sufficient, the bilayer PRs form an uncompleted undercut as in Figure 5.5 (d), which will result in a failure of lift-off. The real etching of LOR resist by developer is isotropic and radiate in a sector shape inside the PR, thus the

etching starts from the uncovered area and sculptures the LOR resist as shown in Figure 5.5 (c) and (d). Therefore, the real sidewall of undercut formed by bilayer PRs is an arc instead of straight wall. By properly controlling the development time, the profile of a well-formed undercut is displayed as in Figure 5.5 (e). The width of the undercut profile formed by bilayer PRs is larger than that of single PR, which significantly decreases the possibility of the adhesion on the sidewall as shown in Figure 5.5 (f), especially for the sputtered material.

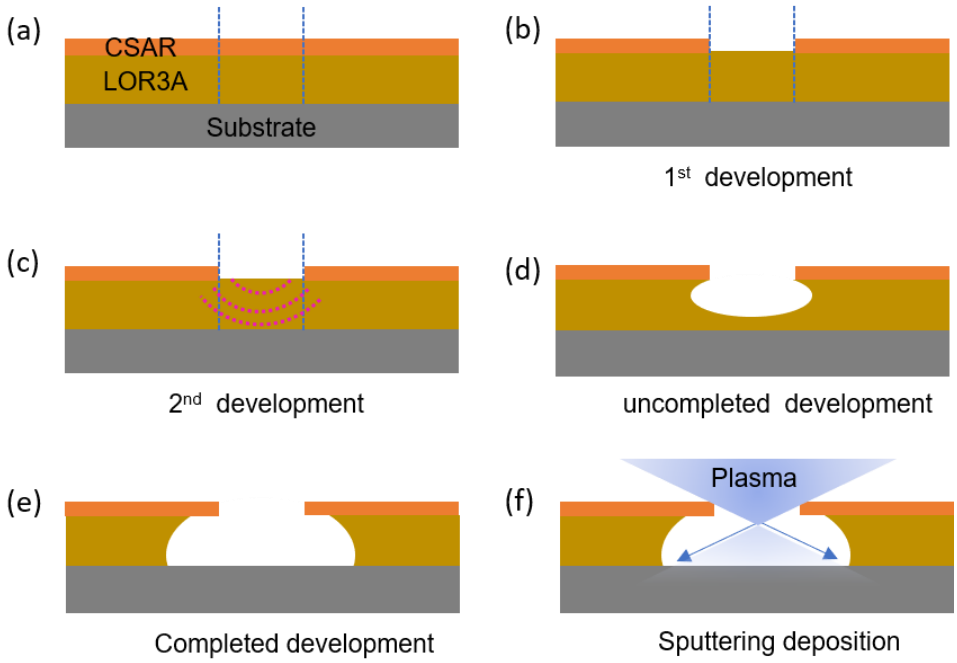

Figure 5.5 Demonstration of the formation of a undercut using bilayer PRs. (a) Coating LOR3A/CSAR on a substrate. The two dotted lines confine the exposure area by e-beam. (b) (c) Two steps of the development process. (d) Undercut profile when the etching of LOR layer is uncompleted. (e) Profile of a completed development for LOR layer. (f) The sputtering deposition inside a bilayer undercut.

This bilayer PRs undercut has been employed in our device fabrication to form the patterns for both lift-off and physically etching processes. The most challenging part is patterning the PR mask for the lift-off of SiO_2 layer. As mentioned before, we need to isolate the area around the Hall bar with SiO_2 but leave a small opening for the electrical connection to the top electrode of the MTJ. In this case, the PRs on top of the Hall bar should be left after the developing, and the covered area of the PRs should be smaller than the width (0.8 μm) of the Hall bar as shown in Figure 5.6 (a). Differ from the regular lift-off pattern, there is very limited area (0.8 μm ×0.8 μm) to build up this bilayer PRs covering with undercut profile. Due to the isotropically etching property of LOR3A, the width of the CSAR in Figure 5.6 (a) should be two times larger than of the thickness of the LOR3A, which ensures no PR residual left on the exposure area after the development. LOR3A has the thickness of 150 nm and the width of the Hall bar is 800 nm. Taking this into consideration, we design the width of the CSAR in Figure 5.6 (a) is 600 nm which stays in the safe range. In this case, properly controlling the development time for LOR3A layer is crucial. If the developing time is too short, there will be residual left. If over development happens, the bilayer undercut will collapse. After a developing time of 25 seconds, the remaining PRs in a clear cross feature is observable. In our e-beam writer dosage test, it was found the cross feature is durable in varying the dose within a range from 160 to 250 uC/cm^2. Beside calibrating the developing time, we also change the simple square opening into a cross shaped opening as shown in Figure 5.6 (b). This helps to increase the area of LOR3A layer such that it can firmly support the upper CSAR. However, the misalignment between this little cross and the Hall bar as shown in Figure 5.6 (c) is undesirable, this kind of opening will lead to the shortage of MTJ after the Au is

deposited into the opening. Therefore, we need an accurate alignment during the EBL writing. In another word, the key point is to keep enough LOR3A underneath the cross area to hold the CSAR layer and the LOR3A under the exposed area should be removed completely.

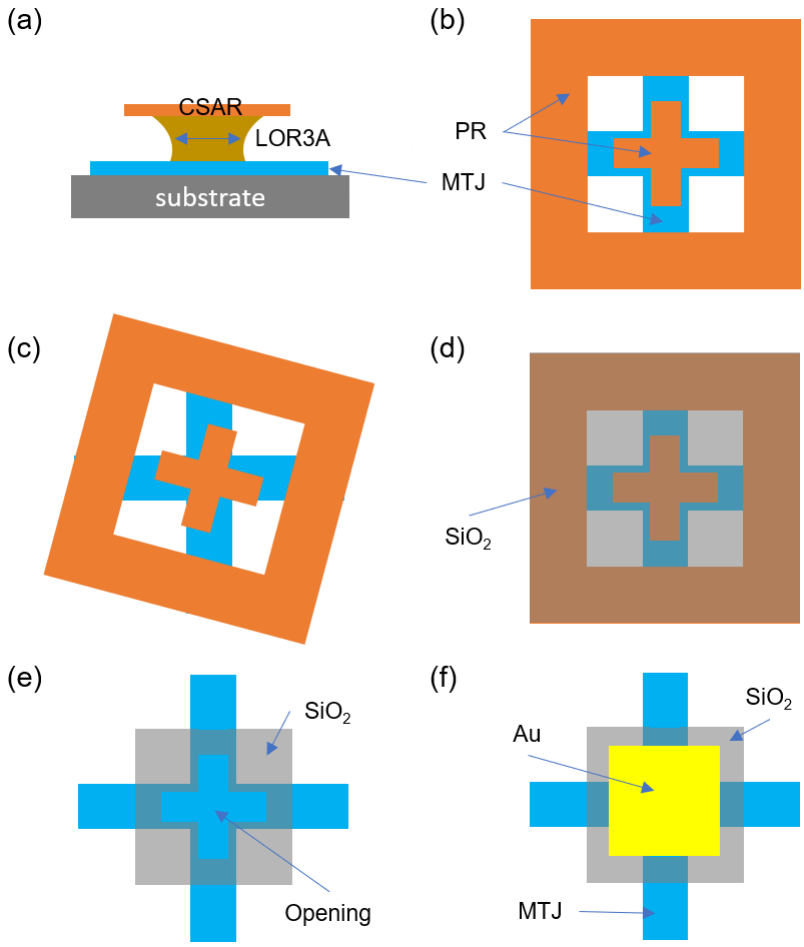

Figure 5.6 (a) The perpendicular cross section of the patterned PRs that is on top the MTJ Hall bar. (b) Patterned PRs (Orange area) for deposition of insulator layer. (c) Patterned PRs pattern with bad alignment. (d) Growth of insulator layer SiO_2 (gray area) on top of (b). (e) Lift-off PRs and patterned SiO_2 left with a cross opening. (f) Top electrode Au layer covers the cross opening.

Once the patterns in in Figure 5.6 (b) is ready, we subsequently deposit a 40 nm SiO_2 layer on the PRs as shown in Figure 5.6 (d). After the deposition, we immerse the sample in a solvent named N-Methyl-2-pyrrolidone (NMP) to remove the PRs mask. After that we also need to wash the sample using isopropyl alcohol (IPA) to clean up the residuals of NMP on the sample. Finally, a patterned SiO_2 layer as shown in Figure 5.6 (e) is left after PRs have been removed completely. The following step is to grow the Ti/Au layers using lift-off technique to cover the crossing opening as shown in Figure 5.6 (f). It is noted that the size of Ti/Au layer should be smaller than that of SiO_2 layer for insolation purpose.

5.4 Integration of ME device

5.4.1 Exchange Coupling in ME device

As mentioned previously that multilayer $[Co/Pd]_n$/Ta/CoFeB(x) is used as a part of the bottom electrode of the MTJ. The [Co/Pd] multilayer has strong PMA and is used to exchange couple with the surface magnetization on the lower Cr_2O_3 layer and to promote PMA in upper CoFeB layer. There is a reason why we do not deposit CoFeB layer directly on top of the Cr_2O_3 layer. In a pMTJ structure, the CoFeB layer must be very thin ($\approx$ 1nm) to promote its PMA, but we need the bottom electrode of the MTJ to be thick enough to connect with the contact pad as shown in Figure 5.2 (b). Simply increasing the bottom CoFeB thickness will significantly reduce its PMA while the [Co/Pd] multilayer does not have this shortcoming.

We first develop the recipe of growing [Co/Pd] multilayers with a good PMA by varying the thickness of Co and Pd layer, respectively. The VSM measured results of samples, Pd(0.7)[Co(0.6)/Pd(x)]$_3$, Pd(0.7)[Co(1.0)/Pd(x)]$_3$, are summarized in

Figure 5.7. We observe very sharp hysteresis loops in samples with Co thickness is 0.6 nm and the coercivity is slightly increasing with Pd thickness. On the other side, sharp switching has not been observed in samples with Co thickness is 1.0 nm, which indicates that the PMA can be well established when Co is thinner than 1.0 nm.

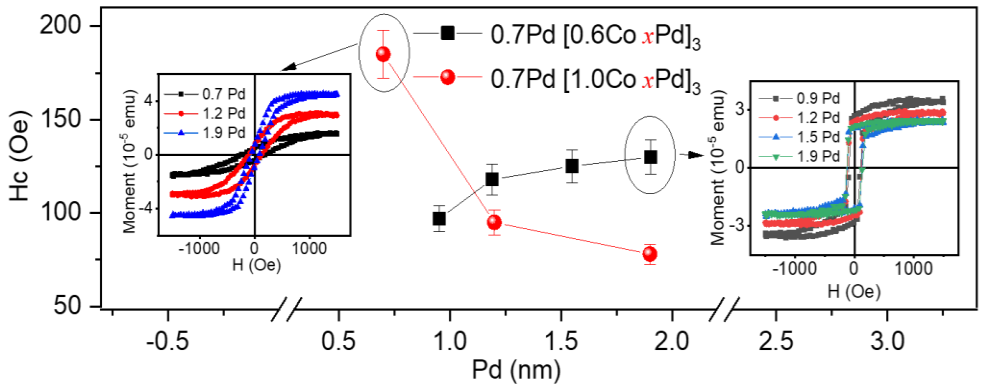

Figure 5.7 The coercivity of [Co/Pd] multilayer as a function of Pd layer thickness.

To characterize the exchange coupling between Cr_2O_3 and [Co/Pd], we fabricate a control device by depositing a Hall bar shaped Pd(0.7)[Co(0.4)/Pd(1.2)]$_3$ multilayer on top of the Cr_2O_3. The SEM image of the Hall bar shaped device is shown in Figure 5.8 (a). To prevent the electric leakage from contact pads, we also insert a thin AlO_x layer underneath the contact pads as shown in Figure 5.8 (b). A bias voltage can be applied on Cr_2O_3 from one of the contact pads through the small Hall bar. The measured AHE hysteresis loop in Figure 5.8 (c) suggests a good PMA in Pd(0.7)[Co(0.4)/Pd(1.2)]$_3$. It is found that the coercivity stays in the range between 122~140 Oe when the width of the hall bar changes from 0.5 μm to 3.0 μm. In Figure 5.8 (d), we compare the data of the device before and after the VCMA treatment. The

treatment includes two steps with: 1) applying a 2 kOe perpendicular magnetic field for 5 mins, and 2) subsequently applying a 1.2 V dc voltage on Cr_2O_3 through the contact pad. The treatments are done at room temperature. It is found that the Pd(0.7)[Co(0.4)/Pd(1.2)]$_3$ multilayer shows a broader AHE hysteresis loop with a center shift of 47 Oe after the treatment, which is a signature of established interfacial exchange coupling between Cr_2O_3 and [Co/Pd] multilayer.

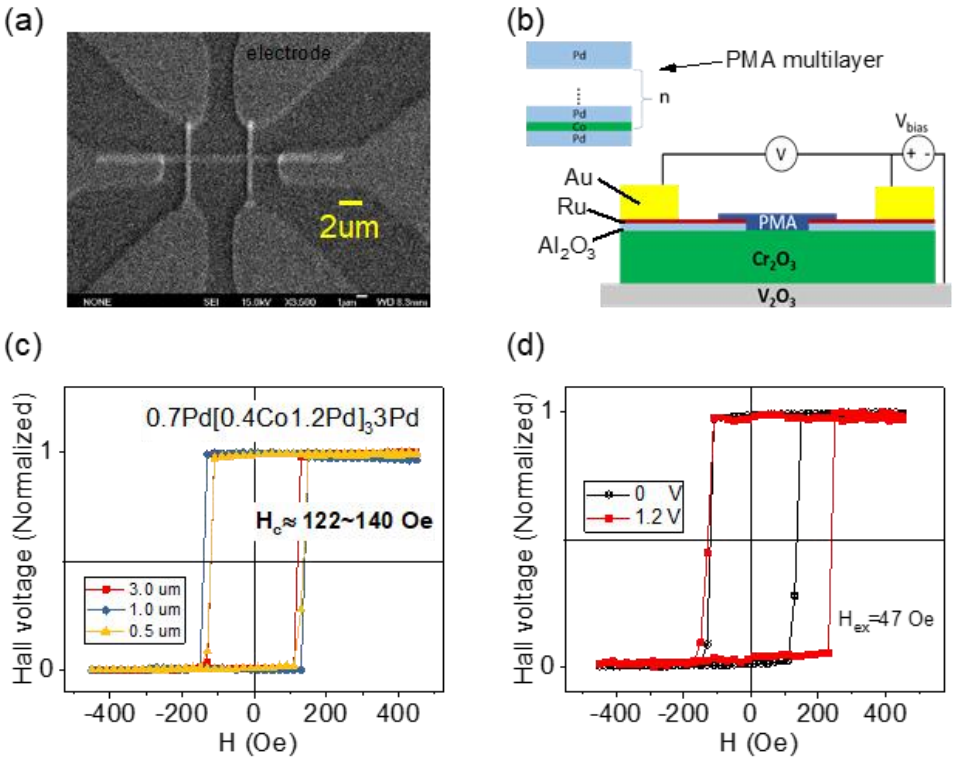

Figure 5.8 (a) The SEM picture of the Hall bar structure of Pd(0.7)[Co(0.4)/Pd(1.2)]$_3$ multilayers on Cr_2O_3. The width of the Hall bar is 1.0 μm. (2) The schematics of the Hall measurement on the PMA sample. (c) AHE loops measured in the samples with different Hall bar width. (d) VCMA measurement with applying a bias voltage of 1.2 V.

The PMA in bottom electrode is characterized by examining the magnetic exchange coupling between Pd(0.7)[Co(0.4)/Pd(1.2)]$_3$ and CoFeB layers. There is a thin Ta layer between them as buffer layer to promote PMA in CoFeB layer, but this Ta layer cannot be too thick to kill the exchange coupling between [Co/Pd] and CoFeB layers. In our device, the Ta thickness is 0.4 nm. To prove the validity of this thickness, we prepare three samples on Si wafer: 1) Pd(0.7)[Co(0.4)/Pd(1.2)]$_3$, 2) Ta/CoFeB(0.9)/MgO(2) and 3) Pd(0.7)[Co(0.4)/Pd(1.2)]$_3$/Ta(0.4)/CoFeB(0.9)/MgO(2). Their AHE results have been shown in Figure 5.9 from (a) to (c). It is found that the coercivity H_c is 100 Oe in [CoPd] sample and 2.5 Oe in Ta/CoFeB/MgO sample. We also compare the AHE of the combined sample with and without 0.4 nm Ta layer(data is not shown here). It turns out that sharp switch disappears in the sample without 0.4 nm Ta layer, which suggests this thin Ta is necessary to promote the PMA in upper CoFeB layer. The coercivity of combined sample is 20 Oe that is smaller than that of 100 Oe in Co/Pd multilayer and larger than that of 2.5 Oe in CoFeB layer, which indicates the exchange coupling between the two PMA layers has been established through the thin Ta layer. In Figure 5.9 (d), we show the VSM result of an MTJ grown on Si wafer with structure CoFeB(0.9)/MgO(2) CoFeB(1.5). Two switch points are observed and have been marked in the loop, in which the first and second switch points correspond to the flip of the magnetization in bottom CoFeB (free layer) and top (fixed layer) layers, respectively. It is noted that the sharpness of the jumps in the hysteresis loop can be enhanced by optimizing the annealing process to our MTJ sample.

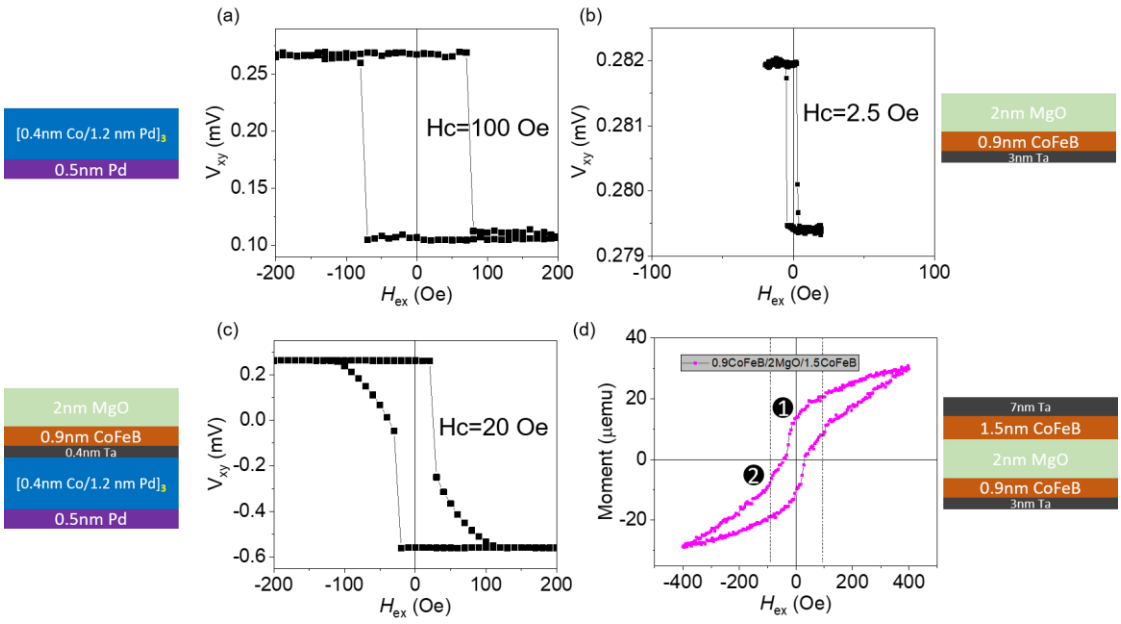

Figure 5.9 (a) AHE measurement of [Co/Pd] multilayer grown on Si wafer. (b) AHE of the sample Ta(3)/CoFeB(0.9)/MgO(2) grown on Si. (c) AHE of sample $[Co/Pd]_3$Ta(0.4)/CoFeB(0.9)/MgO(2). (d) VSM measured magnetic hysteresis loop of the sample CoFeB(0.9)/MgO(2) CoFeB(1.5) grown on Si wafer. An out-of-plane magnetic field is applied for all hysteresis loop measurements.

5.4.2 Integration of ME Device

The integration of the ME device is complicated and challenging due to its nanometer scale and multiple steps in fabrication. We have to assure the good quality of the MTJ in sub-micro size and its interaction to Cr_2O_3 film. The lithography of small features such as the cross-opening needs high writing resolution and precise alignment between layers. In brief, we first use lift-off technique to fabricate the big contact pads which consists of AlO_x(2)/Ru(2). The second step is to transfer small Hall bar pattern onto PRs to lift-off the whole MTJ structure. In the third step, we create the cross-opening and deposit SiO_2 layer using lift-off. The last step is to grow the contact pads for both top and bottom electrodes.

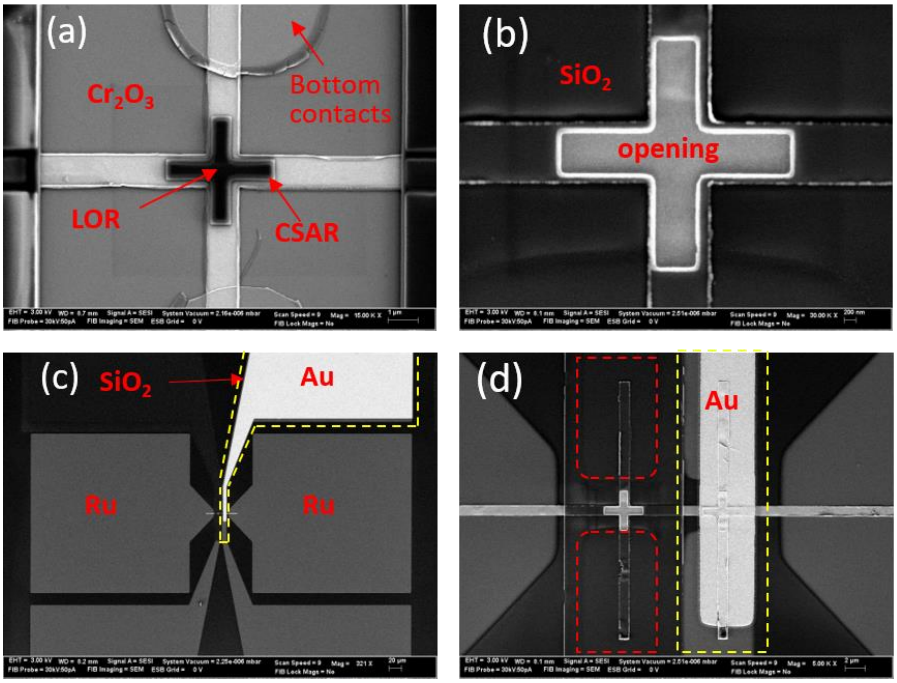

Figure 5.10 (a) The SEM image of the device after the two-step developing process. (b) The SEM image of the SiO_2 layer with opening in the center position. (c) Top view of the device. The yellow dash line draws the outline of the SiO_2 layer underneath the Au electrode. (d) Enlarged view of the Hall cross area. The red dash lines draw the outline of the bottom electrode.

In Figure 5.10 (a), we show the SEM image of the patterned PRs for SiO_2 layer deposition. The black cross is the patterned bilayer LOR/CSAR photoresists which is on top the Hall bar cross and will be removed after SiO_2 deposition in order to access the top electrode of the MTJ. The edges of the PRs cross show light color, which is the signature of the undercut profile formed in this PRs cross. After the deposition of SiO_2 layer and remove the PR cross, it is observed that the PRs cross has been completely removed and the crossing opening window is formed in SiO_2 layer as shown in Figure 5.10 (b). It is also shown that all boundaries of the opening have been well confined inside the boundary of the Hall bar strip, which indicates the upper Ti/Au layers can

be safely deposited subsequently. We use yellow dash lines to depict the outline of the SiO_2 layer underneath the Ti/Au contacts in Figure 5.10 (c). As seen in Figure 5.10 (d), the area of the top contact pad is smaller than that of the patterned SiO_2 layer, which helps to isolate the top electrode from Cr_2O_3 layer.

5.4.3 Issues in Device Fabrication and The Solutions

So far, we have completely fabricated the device with full stacks as shown in Figure 5.10 . However, we failed to acquire the electrical signal from the TMR measurement on our devices. It turns out that the top and bottom electrodes of the MTJ have been shorted. We attribute this problem to the unexpected connection between two CoFeB layers in the MTJ junction. This possibly happens when one applies lift-off technique for film deposition in a sputtering system. Typically, the sputtered films on a flat substrate form an arc-shaped stacks when deposition is confined in a narrow slot (The Hall bar width is 0.8 μm in our device) formed by photoresist as shown in Figure 5.11 (a). The edge part of the film is thinner than the center part. In our junction, the MgO layer is so thin (2 nm, middle area) that it might not well insulate between two CoFeB layers in edge area along the width direction of the Hall bar. It is highly possible that MgO is discontinuous around edge region, which as a result, induces the short-circuit between two electrodes.

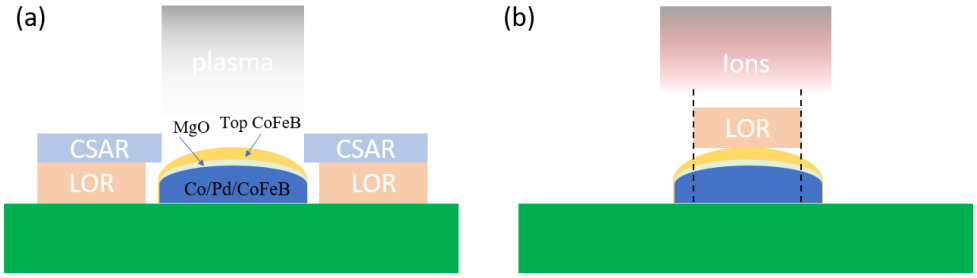

Figure 5.11 (a) Growing shaped MTJ multilayers using lift-off technique in a sputtering system. (b) Dash lines represents the boundary of cutting off the edge of MTJ using the ion mill etching. The area covered by LOR resist survives from this physical etching.

To circumvent this, we have optimized our fabrication by introducing the ion etching process (use ion mill facility) to cut off the shorted edge part of the Hall bar structure. At first, we deposit the whole stacks including Co/Pd multilayer and MTJ as usual but extend the Hall bar width to 5 μm. Then the Hall bar is covered by a Hall bar shaped PR mask written by EBL with width of 0.8 μm as sketched in Figure 5.11 (b). Then the sample is transferred into an ion mill chamber where we can use Ar+ ions to remove the unprotected part until the discontinuous MgO has been completely removed. The covered part of the MTJ survives from the ion etching process. It should be noted that the ion etching on the multilayers must stop at somewhere within Co/Pd multilayer to preserve the connection of bottom electrode to the contact pad outside the stacks. Specifically, that means the etching must be stopped somewhere beyond the Ru layer, otherwise the connection to contact pad will be cut off. From Figure 5.2 (b), we know that the etching tolerance we have is the thickness of metallic multilayers (about 7 nm) between MgO and Ru layers. Thus, it is quite challenging to estimate the etching depth in a thin multilayer structure since the etching rates vary with the materials. In this regard, we have also fabricated a control sample with the

whole MTJ stacks on a transparent glass substrate. The control sample and ME device are etched simultaneously in ion mill chamber. By observing the transparency and measuring the film resistance of the control sample, we can carefully estimate the etching depth in our ME device.

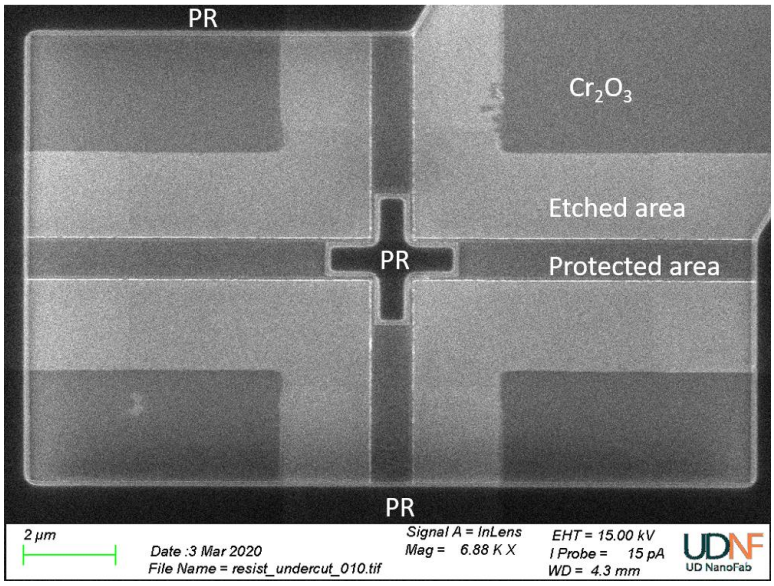

Figure 5.12 SEM images of Hall bar etched by ion mill tool. Dark areas are the PRs.

Figure 5.12 shows the SEM image of the Hall cross area where we label the area of Cr_2O_3, MTJ (under the thin cross protected area) and etched MTJ (bright area, broad cross), and the bilayer PRs cross (the darkest area in the middle). A clear contrast between Cr_2O_3, etched area, and protected area suggests we have safely etched down to [CoPd] multilayer. In Figure 5.13 (a), we can clearly see the boundary of the small cross shows light color, which is the feature of undercut formed by PRs as mentioned above. The inner dark cross is bottom photoresist LOR3A while the outer edge is the extension of the top photoresist CSAR. The outreach of CSAR is measured around 90 nm. In addition, we did not find any part of this small cross extends outside

the region of the thin Hall bar, which means a good alignment was applied between PRs cross and Hall bar strip. The SEM image in Figure 5.13 (b) is the best view of undercut feature we can capture from a tilted angle. We use a red dash line to draw the outline of bottom LOR photoresist for a better view. It is also observed that the surface of thin Hall bar has a larger roughness than the etched area. This is because the thin Hall bar area is the films as grown while the etched area is the polished [CoPd] multilayer by Ar+ ions. Nevertheless, this rough surface still can hold the upper PRs very well since we did not find any PRs fall off after the development process. In addition, one might also observe that there are bright particles intermittently distributed around the outline of the Hall bar. Those are the residuals of the PR after etching process and it is hard to be removed by the regular NMP remover. However, those residuals do not affect the function of our ME memory device because they are not conductive and do not induce any unexpected isolation in our device.

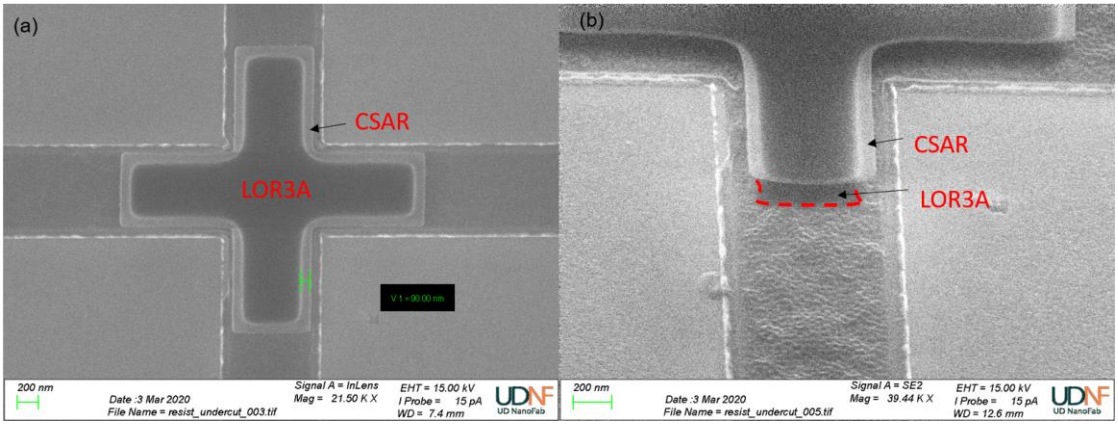

Figure 5.13 SEM pictures of (a) the enlarged view of the cross center. (b) the view of the undercut profile at a tilted angle.

Compared with previous one step lift-off method of patterning Hall bar shaped MTJ, the method of lift-off plus etching down might be a little bit tricky since we must carefully control the etch down depth in MTJ structure. However, the process ensures the quality of MTJ, which, all by itself, is already difficult to fabricate because of the ultrathin MgO barrier layer of only about 1-2 nm. One might concern about the Hall bar fabricated by the second method that the increased contact area with Cr_2O_3 film might increase the chance of current leakage. It is true we have enlarged the width of Hall bar to 5 μm for the first lift-off growth of MTJ. But this width scale is still in the safe range as mentioned in previously that a square contact sizes of 50 μm is still small enough to prevent the current leakage to Cr_2O_3 film.

5.5 Summary

In this chapter, we introduced a novel nano-scaled ME device based on an antiferromagnet Cr_2O_3 which owns significant VCMA property. Its perpendicular surface magnetic moment can be promoted and switched by dc voltage bias. The switching of this surface moment has been employed to switch a perpendicular MTJ (hall bar shaped) in our ME device via the exchange coupling. Avoiding current leakage through Cr_2O_3 is the most crucial thing in fabricating this ME device. For the integrant bottom contact pads in our device, we grew a thin 2nm AlO_x layer underneath to isolate the contact pads from Cr_2O_3 layer. In addition, we also demonstrated the connection between the top electrode of the MTJ to the contact pad can be built through an artificial opening in SiO_2 insulator layer.

REFERENCES

[1] P. Curie,"*First consideration of an intrinsic correlation of magnetic and electric properties in a solid*", J. de Physique (3rd series) **3**, 393 (1894).

[2] P. Debye,"*Bemerkung zu einigen neuen Versuchen über einen magneto-elektrischen Richteffekt*", Zeitschrift für Physik **36**, 300 (1926).

[3] M. Fiebig,"*Revival of the magnetoelectric effect*", Journal of physics D: applied physics **38**, R123 (2005).

[4] E. M. Lifshi͡ts, *Electrodynamics of continuous media* (Pergamon press, 1960), Vol. 8.

[5] T. H. O'Dell, *The electrodynamics of magneto-electric media* (North-Holland Publishing Company, 1970), Vol. 11.

[6] I. E. Dzyaloshinskii,"*On the magneto-electrical effects in antiferromagnets*", Soviet Physics JETP **10**, 628 (1960).

[7] D. Astrov,"*Magnetoelectric effect in chromium oxide*", Sov. Phys. JETP **13**, 729 (1961).

[8] X. He, Y. Wang, N. Wu, A. N. Caruso, E. Vescovo, K. D. Belashchenko, P. A. Dowben, and C. J. N. m. Binek,"*Robust isothermal electric control of exchange bias at room temperature*", **9**, 579 (2010).

[9] C. Binek and B. Doudin,"*Magnetoelectronics with magnetoelectrics*", Journal of Physics: Condensed Matter **17**, L39 (2004).

[10] J.-P. Rivera,"*On definitions, units, measurements, tensor forms of the linear magnetoelectric effect and on a new dynamic method applied to Cr-Cl boracite*", Ferroelectrics **161**, 165 (1994).

[11] P. Borisov, A. Hochstrat, X. Chen, W. Kleemann, and C. Binek,"*Magnetoelectric switching of exchange bias*", Physical review letters **94**, 117203 (2005).

[12] T. Wächtler, *Thin films of copper oxide and copper grown by atomic layer deposition for applications in metallization systems of microelectronic devices* (Thomas Waechtler, 2010).

Chapter 6

SUMMARY AND FUTURE WORK

6.1 Summary of Research and Future Work

This thesis focuses on the study of the magnetization dynamics in spintronic devices. In the first project (Chapter 3), we explored the method of enhancing the resonant frequency. We asked the questions whether the exchange coupling in ferromagnetic materials can be utilized to enhance the resonance frequency since the exchange coupling is much stronger compared with other effective fields induced by strain or anisotropy. While the exchange coupling inside a ferromagnet is difficult to change, it is relatively easy to control the exchange coupling at the interface between two ferromagnetic layers (FM). The optical mode in which the magnetization in two FM layers are precessing out-of-phase is sensitively depending on the exchange coupling and can occur at much high frequencies. We demonstrated this effect using trilayers $Co_{90}Fe_{10}(10)/Ta(t)/ Ni_{80}Fe_{20}(10)$. We also developed a model that explains the experimental results very well. The magnitude of OM is always smaller than that of acoustic mode (AM) because of the out-of-phase precessing. We further ask the question whether we can increase the magnitude of OM which would be a very useful feature if we want to develop a microwave absorber. Through the modeling, we found that the magnitude of the OM can be significantly enhanced by the saturation magnetization contrast between two FM layers. We developed NiFeCu alloys which does not show significant different in magnetic damping but the saturation magnetization dramatically decreases with increasing Cu content. We have successful

demonstrate the magnitude of OM can be significantly enhanced by substituting NiFe with NiFeCu alloy [1]. The future work on this project could focus on how to electrically tune the interlayer coupling via voltage-controlled anisotropy. Another potential direction is to investigate the interlayer coupling in 2D magnetic materials.

In the second project, we investigated the magnetization dynamics under spin orbit torques (SOTs) (Chapter 4). We set to answer three questions: (1) what is rule of the field-like torque and damping-like torque in determining the magnetization dynamics, (2) can we extract the field-like and damping-like toques from dynamic measurements, and (3) are SOTs torques different in dynamic and dc measurements. We used TR-MOKE to measure the magnetization dynamics in 3Py/3Pt and 3Ta/3CoFeB heterostructures. We have shown the field-like torque determines initial oscillation magnitude and the damping-like torque determines the final steady position. We have also demonstrated that the SOT effective fields h_{DL} can be extracted from the plateau value (P) and h_{FL} can be extracted from fitting the TR-MOKE spectrum by varying h_{FL} to match the O/P ratio. The results are in good agreement with DC-MOKE measurements results, indicating that the effective fields do not change at high frequency [2]. The future work can focus on the switching characteristics due to SOTs, including the critical value of SOT for switching, switching process (domain nucleation and motion), switching speed, and zero-bias field switching.

In the third project (Chapter 5), we explored whether the magnetization can be switched by a voltage so that one can significantly reduce the energy consumption. By taking advantage of the VCMA property in antiferromagnet Cr_2O_3, we engineered a nano-scaled ME device where the free layer of the MTJ is coupled to the promoted

surface magnetic moment of the Cr_2O_3. Thus, the switching of Cr_2O_3 would also assist the switching of free layer in MTJ due to the exchange coupling. There are series of challenges in fabricating a functional device, we summarize the challenges and demonstrated solutions.

1. Couple the surface magnetization of Cr_2O_3 to a ferromagnetic layer/heterostructure with perpendicular magnetization (PMA): we have successfully demonstrated that the surface magnetization of Cr_2O_3 can be coupled to [Co/Pt] multilayer.
2. Couple the [Co/Pt] multiplayer to CoFeB with PMA: we have demonstrated that an ultrathin Ta (0.4 nm) can promote PMA in CoFeB with destroying the coupling between [Co/Pd] and CoFeB.
3. Eliminate the leakage problems in Cr_2O_3: the leakage problem is solved by reducing the device size and inserting a thin insulating layer of AlO_x under the contact pads.
4. Make a contact to the middle layer of [Co/Pd]/Ta/CoFeB which is less than 5 nm thick: we demonstrate using Ru thin layer as a connection between layer and contact can make effective contact to middle thin layer.
5. Avoid shorting between two electrodes over MgO barrier which is less than 2 nm thick and open a top widow to access the top contact: we have demonstrated multi-step lithography to achieve this goal.

Due to time and funding restriction, we were not able to demonstrate a functional device in time. However, as illustrated above, most challenges have been resolved.

The research on the field of spintronics has shifted to replace ferromagnetic materials with antiferromagnetic materials (AFM). While this thesis has already

investigated ME devices based on AFM Cr_2O_3, it is author's interest to study the magnetization dynamics in AFM in the future. In the following I briefly summarize the subject and some preliminary results.

6.2 Novel Antiferromagnetic Spintronics

Recently antiferromagnetic (AF) materials have attracted much attention and have been considered as the promising candidate for future spintronic applications owing to the numerous interesting features they combine [3,4]. The simplest antiferromagnets (AFs) are collinear, consisting of anti-aligned magnetic moments $\mathbf{M_1}$ and $\mathbf{M_2}$ belonging to two magnetic sublattices where $M_1=M_2$ results in zero net magnetization. This also means there is no stray fields thus AF materials are insensitive to the external electromagnetic interference. In addition, they display intrinsic high frequency dynamics due to the very large internal exchange coupling. In the past, the value of AF materials is only realized in applying exchange bias in hard disk recording head [5,6], which happens to be the first commercial applications of AF materials.

6.2.1 Antiferromagnetic Dynamics

It is known that the antiferromagnetic resonance (AFMR) can be as large as a few THz, which attributes to the exchange interaction in AFs. The antiferromagnetic dynamics can be descripted by equations of motion of the magnetic sublattice moments similar to those used for FMs but coupled via an inter-sublattice exchange field H_{ex}. The involvement of H_{ex} in FMs requires finite momentum magnon excitations that demagnetize the system. However, in AFs, the inter-sublattice

exchange allows for optical mode zero-momentum excitations that involve H_{ex}. This exchange field is so large that it brings AFMR to THz [7].

In a FM, one can use a uniform static magnetic field, the spin current induced STT or SOTs to compensate the internal damping and induce switching. In an AFM, a uniform static field generates two torques that have opposite signs on the two opposite sublattices as shown in Figure 6.1(a). Those two torques almost compensate each other thus are relatively inefficient at switching AFM or inducing the magnetization dynamics. However, the STT or SOTs can generate an oscillation of the staggered magnetization (or called Néel vector) defined as $\mathbf{L}=\mathbf{M}_1-\mathbf{M}_2$. For example, in the configuration of Figure 6.1(b), the magnetization of the two sublattices interact with a coming spin current polarized in a direction perpendicular to **L**. From the cross relations in Eq (1.41), one can find FL torques on the opposite magnetic sublattices are compensated while the DL torques are parallel. Above a threshold the total torque can induce a stable precession of **L** within the plane perpendicular to the spin-current polarization $\boldsymbol{\sigma}$ [8].

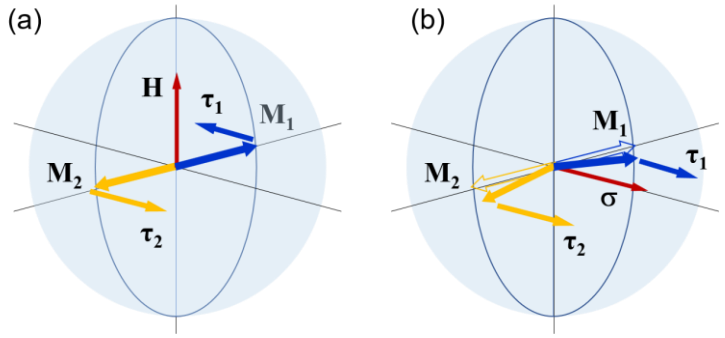

Figure 6.1 Sublattice magnetizations $\mathbf{M}_1$ and $\mathbf{M}_2$ are antiparallel in equilibrium. (a) external magnetic field applied on the AFs generates two opposite torques τ_1 and τ_2. (b) spin with polarization $\boldsymbol{\sigma}$ introduces two parallel torques τ_1 and τ_2.

Furthermore, those spin torques also lead to a small tilt of $\mathbf{M_1}$ and $\mathbf{M_2}$ along the spin polarization direction, which triggers oppositely directed large exchange torques due to the large H_{ex}, then induce fast rotation of the magnetic moments. On the other hand, due to the tilting, i.e., non-zero component of **L** in $\boldsymbol{\sigma}$ direction, the rotation of $\mathbf{M_1}$ and $\mathbf{M_2}$ is associated with appearance of non-zero dynamic magnetization, which allows AFM layer pumps spin current into the neighboring non-magnetic layer similar to a FM. Thus, the FM driven by a magnetic field or a spin polarized current tends to switch between different static states while an AF can works a spin-torque oscillator [9].

6.2.2 Synthetic Antiferromagnetic Materials

One of the challenges to studying AFM dynamics is the lack of characterization tools at THz [10]. The manmade antiparallelly magnetized multilayer, i.e., so-called synthetic antiferromagnets (SyAFs), do not suffer from this drawback because of their weak interlayer exchange. The GHz resonance of SyAFs can also be easily tuned as we demonstrated in Chapter 3. In this regard, the SyAF has become a fruitful model system to simulate AFM.

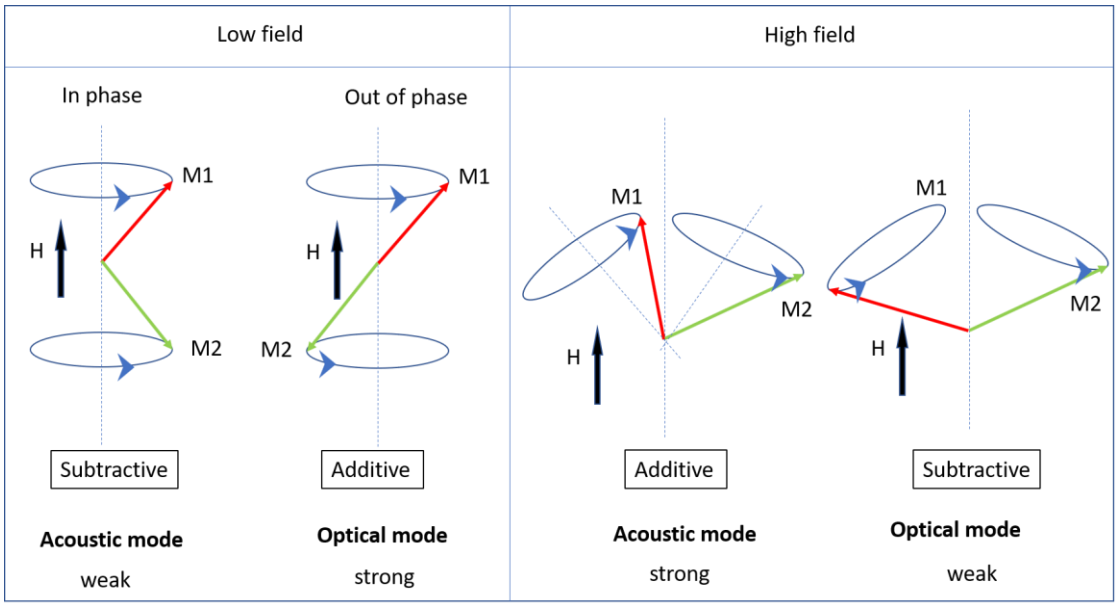

Figure 6.2 Precession diagram of FMR in AFM system at low field (a) and high field (b).

Similar to the synthetic ferromagnets (SyFs) systems presented in Chapter 3, SyAFs also have OM and AM due to the exchange coupling between two magnetic layers. The schematics of two precession magnetization under two modes in a SyAF are shown in Figure 6.2. When the external magnetic field is small, two magnetizations are antiparallelly precessing, which results in a stronger OM in magnitude than that of AM. This is because out-of-phase precession of two opposite magnetizations leads to additive relation of the energy absorption in two magnetic layers. Conversely, in-phase precession in AM has a weak FMR magnitude. However, with increasing the field passing through a critical point (called switching field, H_{sw}), $\mathbf{M_2}$ turns to be switched to the direction of $\mathbf{M_1}$, then the system becomes a FM coupled configuration. As a result, the magnitude comparison between two FMR modes get reversed. In addition, because the total magnetization in OM/AM is

decreasing/increasing with increasing the magnetic field, the frequencies of OM/AM is decreasing/increasing with the field.

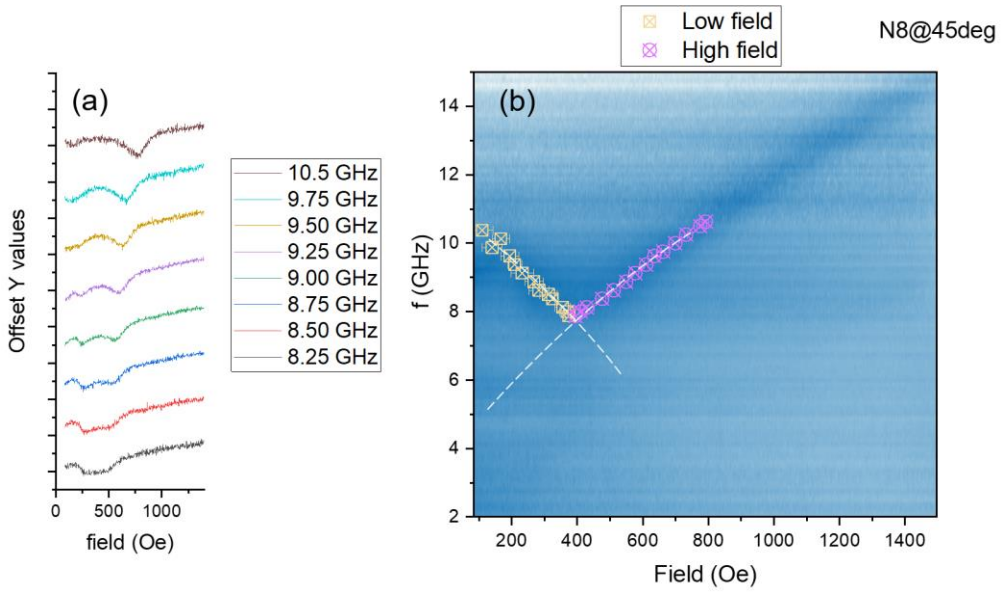

Figure 6.3 (a) FMR spectrums with field scan at different microwave frequencies. (b) color mapping of FMR results where the dark areas sketch the contours of two branches corresponding to OM and AM. The yellow squares and purple circles indicate the position of fitted resonant peaks of OM and AM, respectively.

In Figure 6.3, we show the in-plane FMR measurement data of a SyAF sample 2Ti/10CoFe/0.8Ru/10NiFe/2Ti in which the thin Ru layer induces the AFM coupling between CoFe and NiFe layers. The magnetization in CoFe and NiFe layers are different, thus strictly speaking this is a synthetic ferrimagnet. However, the mentioned above FMR mechanism in SyAF is completely applicable to this synthetic ferrimagnet. It is found in Figure 6.3 (b) the OM (left-short) branch and AM (right-long) branch cross at H= 405 Oe which agrees with the switching field H_{sw} found from

its VSM result (does not show here). We also draw the extension of the two branches after passing through the crossing point. This crossing feature is supposed to be observed in the mapping plot, but the signal is too weak to be displayed in our measured data. To further enhance the signal to noise rate in our measurement, we next plan to integrate our film sample with a coplanar wave (CPW) guide [11] using lithography technique. The design of the patterning is shown in Appendix F.

One of interesting aspect of the SyAF is the hybridization of OM and AM. It is known that the magnon-photon coupling enables the exchange of energy and information between two different systems due to the physical nature of their hybridizing mechanisms, which can be used to develop quantum transducers and long-lifetime multimode quantum memories [12]. In addition, another emerging direction in coherent magnonics study is the magnon-magnon coupling of uniform spin wave modes in SyAF which intrinsically possess two magnon modes, i.e., the exchange interaction between OM and AM in a SyAF. To hybridize OM and AM, the twofold rotational symmetry of the two magnetization vectors about the dc magnetic field needs to be broken [13]. To this end, one can break this symmetry by applying an out of plane external field. It is noted that here the out-of-plane field H is at an angle θ with respect to the normal direction. Due to the demagnetizing field H_d, the magnetizations of the two sublattices are not fully aligned by the field but tilted out of plane along two asymmetric directions, and thus the rotational symmetry is broken.

When the SyAF is under in-plane condition, the system is at ground state and OM and AM cannot interact strongly at the crossing point to degenerate an energy. Applying a large field at a small angle θ can lift this degeneracy where an avoided crossing starts to emerge as a signature of modes hybridization. At this moment,

within the SyAF magnon system the energy transfer between the two modes takes place at a rate of $g/2\pi$ which is proportional to the gap of the anti-crossing. The parameter g is also characterized as the exchange coupling strength of the two modes.

Apart from applying an out of plane field, the coupling strength can also be tuned by changing the wavenumber. For example, in Yoichi's work [14] they found that the magnitude of the anti-crossing gap can be enhanced by increasing the wave number of excited spin waves. We refer to this method in the device design of our SyAF sample CoFe/Ru/NiFe by changing the signal line width and gap width of the CPW.

Above we briefly summarize our preliminary results on SyAF and future direction for AFM research. The author would like to continuously pursue these research topics and encourage graduate students to work in this area.

REFERENCES

[1] H. Chen, Y. Chen, T. Wang, Y. Xie, A. F. Franco, and J. Q. Xiao,"*Tuning Optical Mode of Ferromagnetic Resonance in Exchange-Coupled CoFe/Ta/(NiFe) 1–x Cu_x Trilayers*", IEEE Transactions on Magnetics **56**, 1 (2020).

[2] X. Zhou, H. Chen, Y.-S. Ou, T. Wang, R. Barri, H. Kannan, J. Q. Xiao, and M. F. Doty,"*Investigation of spin orbit torque driven dynamics in ferromagnetic heterostructures*", Journal of Magnetism and Magnetic Materials **503**, 166211 (2020).

[3] M. B. Jungfleisch, W. Zhang, and A. Hoffmann,"*Perspectives of antiferromagnetic spintronics*", Physics Letters A **382**, 865 (2018).

[4] V. Baltz, A. Manchon, M. Tsoi, T. Moriyama, T. Ono, and Y. Tserkovnyak,"*Antiferromagnetic spintronics*", Reviews of Modern Physics **90**, 015005 (2018).

[5] W. Zhang and K. M. Krishnan,"*Epitaxial exchange-bias systems: From fundamentals to future spin-orbitronics*", Materials Science and Engineering: R: Reports **105**, 1 (2016).

[6] J. Nogués and I. K. Schuller,"*Exchange bias*", Journal of Magnetism and Magnetic Materials **192**, 203 (1999).

[7] P. Ross, M. Schreier, J. Lotze, H. Huebl, R. Gross, and S. T. Goennenwein,"*Antiferromagentic resonance detected by direct current voltages in MnF2/Pt bilayers*", Journal of Applied Physics **118**, 233907 (2015).

[8] R. Cheng, M. W. Daniels, J.-G. Zhu, and D. Xiao,"*Ultrafast switching of antiferromagnets via spin-transfer torque*", Physical Review B **91**, 064423 (2015).

[9] R. Cheng, J. Xiao, Q. Niu, and A. Brataas,"*Spin pumping and spin-transfer torques in antiferromagnets*", Physical review letters **113**, 057601 (2014).

[10] T. Chiba, G. E. Bauer, and S. Takahashi,"*Magnetization damping in noncollinear spin valves with antiferromagnetic interlayer couplings*", Physical Review B **92**, 054407 (2015).

[11] R. Simons and R. N. Simons, *Coplanar waveguide circuits, components, and systems* (Wiley Online Library, 2001), Vol. 15.

[12] B. Bhoi and S.-K. Kim,"*Photon-magnon coupling: historical perspective, status, and future directions*", Solid State Physics **70**, 1 (2019).

[13] D. MacNeill, J. T. Hou, D. R. Klein, P. Zhang, P. Jarillo-Herrero, and L. Liu,"*Gigahertz Frequency Antiferromagnetic Resonance and Strong Magnon-Magnon Coupling in the Layered Crystal CrCl 3*", Physical review letters **123**, 047204 (2019).

[14] Y. Shiota, T. Taniguchi, M. Ishibashi, T. Moriyama, and T. Ono,"*Tunable Magnon-Magnon Coupling Mediated by Dynamic Dipolar Interaction in Synthetic Antiferromagnets*", Physical Review Letters **125**, 017203 (2020).

Appendix A

DERIVATION OF SUSCEPTIBILITY TENSOR χ

In a bilayer system the LLG equation for the magnetization in each layer is given

$$\frac{d\mathbf{M}_1}{dt} = -\gamma\left(\mathbf{M}_1 \times \mathbf{H}_{eff\,1}\right) + \frac{\alpha_1}{M_{s1}}\mathbf{M}_1 \times \frac{d\mathbf{M}_1}{dt}, \tag{A1}$$

$$\frac{d\mathbf{M}_2}{dt} = -\gamma\left(\mathbf{M}_2 \times \mathbf{H}_{eff\,2}\right) + \frac{\alpha_2}{M_{s2}}\mathbf{M}_2 \times \frac{d\mathbf{M}_2}{dt}, \tag{A2}$$

By substituting the time dependent M_s and the total effective fields H_{eff} discussed in main text into Eq. (A1), (A2), one obtains

$$D * \begin{bmatrix} m_{1x} \\ m_{1y} \\ m_{2x} \\ m_{2y} \end{bmatrix} = \begin{bmatrix} 0 & M_{1s} & 0 & 0 \\ -M_{1s} & 0 & 0 & 0 \\ 0 & 0 & 0 & M_{2s} \\ 0 & 0 & -M_{2s} & 0 \end{bmatrix} * \begin{bmatrix} h \\ 0 \\ h \\ 0 \end{bmatrix}, \tag{A3}$$

where the matrix for *rf* field is given according to the direction of the microwave induced magnetic field which is along *x* direction in our experiment. The matrix *D* on left hand side of Eq. (A3) is written as

$$D = \begin{bmatrix} \frac{i\omega}{\gamma} & H + M_{1s} + \frac{i\alpha_1\omega}{\gamma} + A_{12}M_{2s} & 0 & -A_{21}M_{1s} \\ -H - \frac{i\alpha_1\omega}{\gamma} - A_{12}M_{2s} & \frac{i\omega}{\gamma} & A_{21}M_{1s} & 0 \\ 0 & -A_{12}M_{2s} & \frac{i\omega}{\gamma} & H + M_{2s} + \frac{i\alpha_2\omega}{\gamma} + A_{21}M_{1s} \\ A_{12}M_{2s} & 0 & -H - \frac{i\alpha_2\omega}{\gamma} - A_{21}M_{1s} & \frac{i\omega}{\gamma} \end{bmatrix}, \tag{A4}$$

The two dispersive relation corresponding to the two FMR modes can be obtained by eigenvalues of D via the solution of $det\ |D|=0$. Given $m_{ij} = \overleftrightarrow{\chi} * h$, from Eq. (A3) we can write the susceptibility tensor in a coupled bilayer as

$$\chi = D^{-1} * \begin{bmatrix} 0 & M_{1s} & 0 & 0 \\ -M_{1s} & 0 & 0 & 0 \\ 0 & 0 & 0 & M_{2s} \\ 0 & 0 & -M_{2s} & 0 \end{bmatrix} = \begin{bmatrix} \chi_{1x,1x} & 0 & \chi_{1x,2x} & 0 \\ \chi_{1y,1x} & 0 & \chi_{1y,2x} & 0 \\ \chi_{2x,1x} & 0 & \chi_{2x,2x} & 0 \\ \chi_{2y,1x} & 0 & \chi_{2y,2x} & 0 \end{bmatrix}, \qquad \text{(A5)}$$

where D^{-1} is the inverse of matrix D, i=1, 2 is the index of while j= x, y represents the direction.

Appendix B

NUMERICAL SIMULATION CODE FOR FMR IN FERROMAGNETIC COUPLED BILAYER

```
clear
syms w hext a A12 A21
gama=28;
m1s=1.9;
m2s=0.4;
a1=0.005;
a2=0.008;
hext=0.03;

A=eye(4)./gama*i*w;   %frequency matrix
M1=[0,hext+m1s;-hext,0];
M2=[0,hext+m2s;-hext,0];
g1=[0,i*a1*w/gama;-i*a1*w/gama,0];
g2=[0,i*a2*w/gama;-i*a2*w/gama,0];
M=blkdiag(M1,M2);
G=blkdiag(g1,g2);

J11=[0,A12*m2s;-A12*m2s,0];
J12=[0,-A12*m1s;A12*m1s,0];
J21=[0,-A21*m2s;A21*m2s,0];
J22=[0,A21*m1s;-A21*m1s,0];

J=[J11,J12;J21,J22];
b1=[0;-m1s;0;0];
b2=[0;0;0;-m2s];
Dm=M+A+J;
D=Dm+G;
s=inv(D)*(b1);% s is kafa volumn matrix induced by rf field b1
ss=inv(D)*(b2);% ss is kafa volumn matrix induced by rf field b2
n=100;
k=1:1:n
s1=1:1:n;
s2=1:1:n;
r11=zeros(n);
r12=zeros(n);
r13=zeros(n);
r14=zeros(n);
r21=zeros(n);
r22=zeros(n);
r23=zeros(n);
```

```
r24=zeros(n);
for m=1:1:4     % vary exchange strength
    A12=(m-1)*0.0001;  % A12 is positive for AF, negative for AFM
    A21=A12;
for j=1:1:n
    w=j*0.2;    % vary frequency
    s11(j)=eval(s(1));        %read for loop, know s11()
    s12(j)=eval(s(2));
    s13(j)=eval(s(3));
    s14(j)=eval(s(4));
    s21(j)=eval(ss(1));
    s22(j)=eval(ss(2));
    s23(j)=eval(ss(3));
    s24(j)=eval(ss(4));
end
r11(:,m)=imag(-s11);        %take nagative value and find imag part
r12(:,m)=imag(-s12);
r13(:,m)=imag(-s13);
r14(:,m)=imag(-s14);
r21(:,m)=imag(-s21);
r22(:,m)=imag(-s22);
r23(:,m)=imag(-s23);
r24(:,m)=imag(-s24);
end
plot(k,r11(:,2))
```

Appendix C

DEVICE DESIGNS FOR DC-MOKE MEASUREMENT

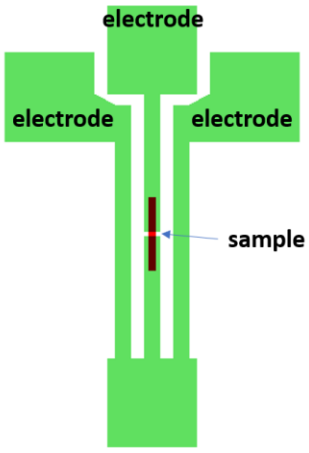

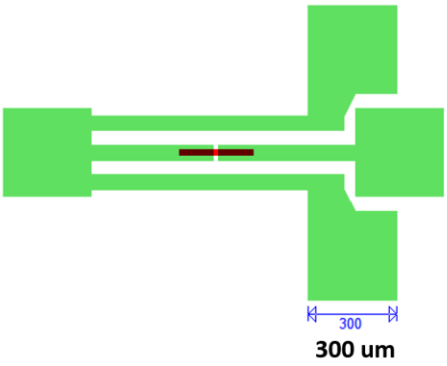

.

Appendix D

OOMMF SIMULATION CODE FOR SOTS INDUCED DYNAMICS

```
# MIF 2.1
set pi [expr 4*atan(1.0)]
set mu0 [expr 4*$pi*1e-7]
RandomSeed 1
Parameter cellsize 100e-9
set x_length 20e-7
set y_width 250e-7
set z_thick 3e-9

# t0 is start time, t1 is width of pulse
Parameter t0 1.1e-9
Parameter t1 6.6e-9
Parameter h  0
# h in unit of mT

# Current density in unit A/m2
Parameter current_density 2.39e10
Parameter Polarization 0.077
# Polarization is exactly the spin Hall angle
Parameter Primee 0.01
Parameter Lambda 1.0
Parameter phi 270
Parameter beta 0

set phi_inp   [expr {$phi*$pi/180.}]
set beta_inp   [expr {$beta*$pi/180.}]

Specify Oxs_BoxAtlas:atlas [subst {
  xrange {0 $x_length}
  yrange {0 $y_width}
  zrange {0 $z_thick}
}]

Specify Oxs_RectangularMesh:mesh [subst {
  cellsize {$cellsize $cellsize 1e-9}
```

```
  atlas :atlas
}]

Specify Oxs_UniaxialAnisotropy {
  K1  1750
  axis {0 1 0}
}

Specify Oxs_UniformExchange {
  A  13e-12
}

# Temporal signature of applied field
proc Fprofile { total_time } {
    global t0 t1 h
    set Hy 0.0;
          set dHy 0.0;

    set tt [expr {$total_time-$t0}]
    if {$tt<0} {
              set Hy 0.0
                    set dHy 0.0
          } elseif {$tt<0.05e-9} {
        set Hy [expr {$h*$tt/0.05e-9}]
                    set dHy $h
    } elseif {$tt<0.05e-9+$t1} {
        set Hy $h
                    set dHy 0.0
    } elseif {$tt<0.1e-9+$t1} {
        set Hy [expr {$h*(0.1e-9+$t1-$tt)/0.05e-9}]
                    set dHy -$h
    }
    return [ list 0 $Hy 0 0 $dHy 0 ]
}

Specify Oxs_ScriptUZeeman {
   script_args total_time
   script Fprofile
   multiplier 795.77
}

# Add external field, 10 mT
Specify Oxs_FixedZeeman [subst {
```

```
  field {[expr {cos($beta_inp)}] [expr {sin($beta_inp)}] 0}
  multiplier [expr {15*0.001/$mu0}]
}]

Specify Oxs_Demag {}

# Evolver
Specify Oxs_SpinXferEvolve:evolve [subst {
   alpha 0.038
   start_dm 0.04
   mp {[expr {cos($phi_inp)}] [expr {sin($phi_inp)}] 0}
   J $current_density
   J_profile Jprofile
   J_profile_args total_time
   P $Polarization
   Lambda $Lambda
         eps_prime $Primee
}]

Specify Oxs_TimeDriver [subst {
 evolver :evolve
 stopping_time 14e-9
 mesh :mesh
 Ms 760e3
 m0 {1 0 0}
}]

proc Jprofile { total_time } {
   global t0 t1
   set scale 0.0;
   set tt [expr {$total_time-$t0}]
   if {$tt<0} {
            set scale 0.0
         } elseif {$tt<0.05e-9} {
      set scale [expr {$tt/0.05e-9}]
   } elseif {$tt<0.05e-9+$t1} {
      set scale 1.0
   } elseif {$tt<0.1e-9+$t1} {
      set scale [expr {(0.1e-9+$t1-$tt)/0.05e-9}]
   }
   return $scale
}.
```

Appendix E

PATTERN DESIGN OF ME-MTJ DEVICE

(A)

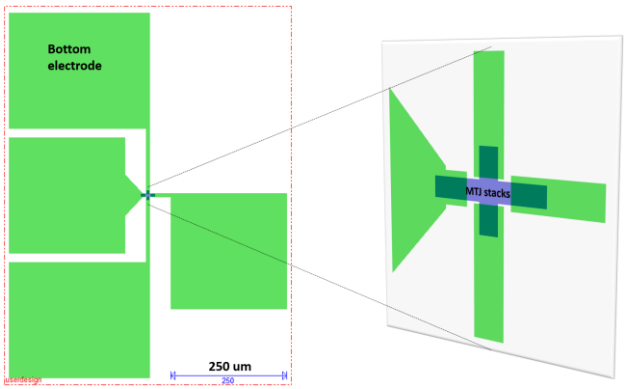

(b)

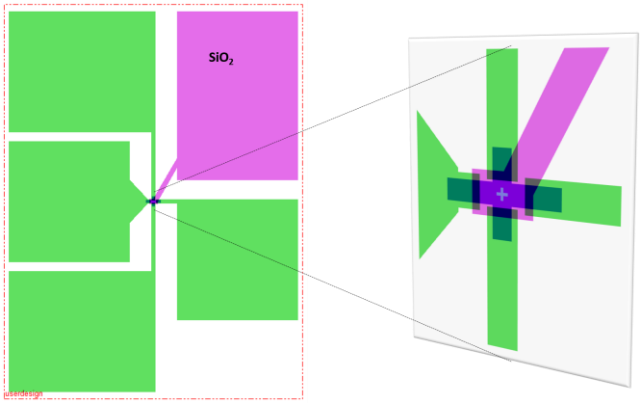

(c)

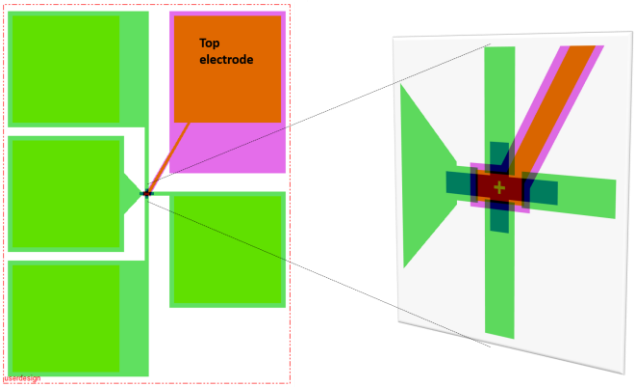

Appendix F

PATTERN DESIGN OF SYNTHETIC ANTIFERROMAGNETIC DEVICE

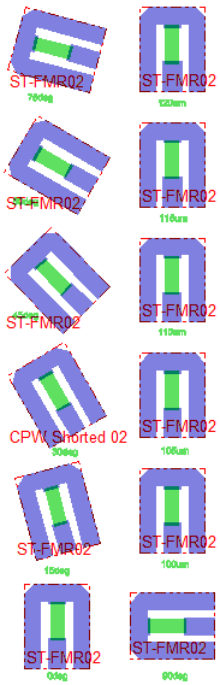

Note: the layout of the upper pattern design was provided by Dr. Benjamin Jungfleisch group in University of Delaware.

Appendix G

REPRINT PERMISSIONS

Reprint Permissions for Figures in Chapter 3 and 4.

Copyright Clearance Center RightsLink®

Home | Help | Live Chat | Sign in | Create Account

IEEE Requesting permission to reuse content from an IEEE publication

Tuning Optical Mode of Ferromagnetic Resonance in Exchange-Coupled CoFe/Ta/(NiFe)1−xCux Trilayers

Author: Hang Chen
Publication: IEEE Transactions on Magnetics
Publisher: IEEE
Date: Aug. 2020

Copyright © 2020, IEEE

Thesis / Dissertation Reuse

The IEEE does not require individuals working on a thesis to obtain a formal reuse license, however, you may print out this statement to be used as a permission grant:

Requirements to be followed when using any portion (e.g., figure, graph, table, or textual material) of an IEEE copyrighted paper in a thesis:

1) In the case of textual material (e.g., using short quotes or referring to the work within these papers) users must give full credit to the original source (author, paper, publication) followed by the IEEE copyright line © 2011 IEEE.
2) In the case of illustrations or tabular material, we require that the copyright line © [Year of original publication] IEEE appear prominently with each reprinted figure and/or table.
3) If a substantial portion of the original paper is to be used, and if you are not the senior author, also obtain the senior author's approval.

Requirements to be followed when using an entire IEEE copyrighted paper in a thesis:

1) The following IEEE copyright/ credit notice should be placed prominently in the references: © [year of original publication] IEEE. Reprinted, with permission, from [author names, paper title, IEEE publication title, and month/year of publication]
2) Only the accepted version of an IEEE copyrighted paper can be used when posting the paper or your thesis on-line.
3) In placing the thesis on the author's university website, please display the following message in a prominent place on the website: In reference to IEEE copyrighted material which is used with permission in this thesis, the IEEE does not endorse any of [university/educational entity's name goes here]'s products or services. Internal or personal use of this material is permitted. If interested in reprinting/republishing IEEE copyrighted material for advertising or promotional purposes or for creating new collective works for resale or redistribution, please go to http://www.ieee.org/publications_standards/publications/rights/rights_link.html to learn how to obtain a License from RightsLink.

If applicable, University Microfilms and/or ProQuest Library, or the Archives of Canada may supply single copies of the dissertation.

BACK CLOSE WINDOW

© 2021 Copyright - All Rights Reserved | Copyright Clearance Center, Inc. | Privacy statement | Terms and Conditions
Comments? We would like to hear from you. E-mail us at customercare@copyright.com

Copyright Clearance Center RightsLink®

Home | Help | Live Chat | Sign in | Create Account

Investigation of spin orbit torque driven dynamics in ferromagnetic heterostructures

Author:
Xinran Zhou,Hang Chen,Yu-Sheng Ou,Tao Wang,Rasoul Barri,Harsha Kannan,John Q. Xiao,Matthew F. Doty

Publication: Journal of Magnetism and Magnetic Materials

Publisher: Elsevier

Date: 1 June 2020

© 2019 Published by Elsevier B.V.

Journal Author Rights

Please note that, as the author of this Elsevier article, you retain the right to include it in a thesis or dissertation, provided it is not published commercially. Permission is not required, but please ensure that you reference the journal as the original source. For more information on this and on your other retained rights, please visit: https://www.elsevier.com/about/our-business/policies/copyright#Author-rights

BACK CLOSE WINDOW

© 2021 Copyright - All Rights Reserved | Copyright Clearance Center, Inc. | Privacy statement | Terms and Conditions
Comments? We would like to hear from you. E-mail us at customercare@copyright.com